UNIVERSITY OF CALIFORNIA
RIVERSIDE

Dynamics of eIF4F Mediated Messenger RNA Cap Recognition in Early Translation Initiation

A Dissertation submitted in partial satisfaction
of the requirements for the degree of

Doctor of Philosophy

in

Cell, Molecular, and Developmental Biology

by

Burak Cetin

June 2022

Dissertation Committee:

Dr. Seán O'Leary, Chairperson
Dr. Jernej Murn
Dr. Sika Zheng

The Dissertation of Burak Cetin is approved:

Committee Chairperson

University of California, Riverside

ACKNOWLEDGEMENTS

The text of this dissertation in part is a reprint of the material as it appears in Çetin B, Song GJ, O'Leary SE. Heterogeneous Dynamics of Protein-RNA Interactions across Transcriptome-Derived Messenger RNA Populations. J Am Chem Soc. 2020 Dec 23;142(51):21249-21253.

Çetin B, O'Leary SE. mRNA- and factor-driven dynamic variability controls eIF4F-cap recognition for translation initiation. Nucleic Acids Res. In press. 2022

The co-author, Seán O'Leary listed in the publications above, directed and supervised the research.

ABSTRACT OF THE DISSERTATION

Dynamics of eIF4F Mediated Messenger RNA Cap Recognition in Early Translation Initiation

by

Burak Cetin

Doctor of Philosophy, Graduate Program in Cell, Molecular, and Developmental Biology
University of California, Riverside, June 2022
Dr. Seán O'Leary, Chairperson

Translation initiation is a critical step of protein synthesis across all domains of life. In eukaryotes, the first step of this process is formation of a messenger ribonucleoprotein particle between the messenger RNA and the initiation factor complex named eIF4F. This process is required for canonical translation initiation in eukaryotes and is followed by recruitment of the ribosome and downstream initiation processes to form an elongation-competent ribosome. Here, I extensively characterized the formation of the eIF4F complex on yeast mRNAs, using a combination of in vitro reconstitution of this complex and single molecule techniques. A single-molecule FRET-based assay utilizing fluorescently labeled eIF4E and mRNA was used to measure the basal rates of formation and dissociation of the complex between the cap binding subunit eIF4E and using model mRNAs transcribed in vitro, in addition to pools of mRNAs extracted from cells. The eIF4E-mRNA interaction is highly dynamic and dependent on mRNA features, with the rate of binding causing variability between mRNAs. Characterizing the eIF4E binding of different mRNAs revealed that the binding is controlled by mRNA cap-

proximal structure and length. The contributions of other eIF4F subunits to cap binding by eIF4F (eIF4A and eIF4G) were elucidated on different mRNAs. eIF4A and eIF4G can both enhance the formation of this complex by accelerating the rate of formation, whereas eIF4G also stabilizes the complex, increasing the bound lifetime of eIF4E to the mRNA cap. Further studies truncating the eIF4G peptide demonstrated that the multiple RNA-binding domains are required to increasing the bound lifetime, whereas the first domain is sufficient to accelerate the rate of formation of the eIF4E-mRNA complex. ATP further increases the rate of formation and lifetime of the complex. Lastly, three and four-color single molecule fluorescence assays were developed, fluorescently labeling eIF4A, and eIF4G. Utilizing these, we revealed the order of disassembly of these factors on mRNA. eIF4E (together with eIF4G) is likely to be ejected from the mRNA cap after formation of the eIF4F complex, which appears to be similar between mRNAs. An approach for automating data analysis on our custom single molecule imaging platform is also discussed. Ultimately, the study elucidated the eIF4E cap binding dynamics on model mRNAs and populations, and elucidated the contribution of other eIF4F subunits, as well as the mechanism of eIF4F assembly and the ATP dependence.

TABLE OF CONTENTS

List of Figures

Chapter 1. Dynamics of eIF4E binding to mRNAs

Introduction

Protein synthesis is a crucial stage of gene expression and is tightly regulated to ensure the right types of proteins are translated in the right dosage required by the cell. In eukaryotes, translational control is exerted particularly at the initiation step Sonenberg and Hinnebusch., 2009), and this regulation is crucial for cell growth, differentiation, and development. Translational control therefore determines the expression rate of many genes throughout the transcriptome (Gebauer and Hentze 2004). Translational control also allows cells to respond to stimuli faster than transcriptional control and is less wasteful in terms of energy required to synthesize new transcripts (Hershey et al., 2014). In addition, translational control is needed because there is a significant energy expenditure during translation from each round of elongation requiring nucleotide hydrolysis. The mechanism of canonical translation initiation involves the 5′ 7-methylguanosine cap structure added to mRNA (Shatkin 1976, Sonenberg and Hinnebusch, 2009). The cap structure, which is co-transcriptionally added to mRNAs, plays an important role in determining translational efficiency and stability of transcripts, where the translation of many transcripts is strongly dependent on the presence of this structure, along with the poly(A) tail (Kozak 1999, Ramanathan et al. 2016). This structure is bound and recognized by a core set of initiation factors before protein synthesis can take place. mRNA translation

efficiencies vary between transcripts, and initiation is tightly controlled based on mRNA features and sequence (Jackson et al. 2010). The rate of initiation is thus an important parameter for determining translational output (Sharma et al. 2019; Szavits-Nossan and Ciandrini 2020).

Binding of eIF4F to mRNAs is thought to “prime” or activate them for protein synthesis. Formation of a complex between the mRNA 5′ cap and the heterotrimeric eIF4F complex is followed by recruitment of the small ribosomal subunit, as a 43S pre-initiation complex (PIC) with additional factors (Hinnebusch and Lorsch, 2012). The 43S PIC binds to the mRNA near the 5′ end, which is facilitated by eIF4F, eIF3, the poly(A) binding protein (which binds the eIF4F subunit eIF4G and the mRNA poly(A) tail) (Tarun and Sachs 1995, Tarun et al. 1997, Kahvejian et al. 2005), resulting in the formation of a “closed-loop” particle through the interaction of the poly(A) binding protein with eIF4G. The resulting protein bridge from eIF4F factors and poly(A) binding protein facilitates the loading of the 43S PIC to the mRNA 5′ end. PABP binds the poly(A) tail present on mRNAs and activates translation in a dose-dependent manner (Machida et al. 2018). Once loaded onto the mRNA, the PIC is thought to move through the mRNA 5′ leader toward the start codon, in a process known as scanning (Hinnebusch and Lorsch, 2012). This is followed by compositional (such as dissociation of eIF1, 1A) as well as conformational changes culminating in the joining of the large ribosomal subunit to produce an elongation-competent 80S particle (Nanda et al. 2013, Hinnebusch 2014; Pelletier and Sonenberg 2019,

Hussain et al. 2014). The ribosome can then proceed with elongation to synthesize the multitude of proteins required by the cell (Kozak 1999, Hershey et al. 2012). Since initiation of translation is thought to be the rate-limiting step (Shah et al. 2013), it is important to understand its molecular mechanisms and how they differ between mRNAs.

eIF4F is composed of three subunits. The eIF4E subunit binds the mRNA cap specifically recognizing the 7-methylguanosine structure. This binding is a critical first step for loading of the ribosome to the 5′ end, with eIF4E directing other factors to the 5′ end. This factor was first isolated based on cross-linking to the mRNA cap structure (Sonenberg et al. 1978). Further studies using affinity purification identified other eIF4F factors that co-purify with eIF4E in a complex (Etchison and Milburn 1987; Grifo et al. 1983), which were later named eIF4G and eIF4A. eIF4G acts as a “scaffold” protein to assemble the complex and mediate interactions between eIF4F and the ribosome (Aitken and Lorsch 2012), and eIF4A is an ATP-dependent RNA helicase thought to resolve RNA structures that occur near the mRNA 5′ end (Lu et al. 2014, Gingras et al. 1999). eIF4A is a weak helicase on its own, but its processivity is enhanced by eIF4F and other factors such as eIF4B and eIF4H, shown in previous biophysical and biochemical experiments (Özeş et al. 2011, García-García et al. 2015) Binding of eIF4G and other factors to eIF4A favors a more active, “closed” conformation of the helicase, stimulating RNA unwinding through local strand separation as well as the rate of ATP hydrolysis (Schütz et al. 2008, Harms et al. 2014; Andreou and

Klostermeier 2014; Andreou and Klostermeier 2013, Nielsen et al. 2011) In addition, the unwinding is biased towards duplexes with 5′ overhangs in yeast (Rajagopal et al. 2012). In addition, recent studies suggest eIF4A enhances the recruitment small ribosomal subunit to different mRNAs, regardless of structural complexity (Yourik et al. 2017). Furthermore, the protein is present in excess of the other eIF4F components (Duncan and Hershey 1983, von der Haar and McCarthy 2002), and the activity of the free fraction appears to regulate translation (Firczuk et al. 2013). Additional interactions between eIF4G and 43S PIC components result in PIC recruitment to the mRNA, directed to the 5′ end through the interaction between eIF4E and the mRNA cap structure (Merrick, 2015). In mammals, eIF4G directly interacts with eIF3 subunits to promote ribosome recruitment to the mRNA (Villa et al. 2013).

At the cellular level, the availability of eIF4E for incorporation into eIF4F is extensively regulated through interaction with 4E-binding proteins (4EBPs), which bind and sequester it away from eIF4G to globally inhibit translation (von der Haar et al., 2004). The large-scale, transcriptome-wide changes to translational output induced by 4EBP activity have been a key line of evidence highlighting the importance of eIF4F in controlling gene expression. 4EBP's ability to interact with eIF4E is controlled through phosphorylation through several cellular pathways (Karaki et al. 2015). These pathways ultimately change the "active" eIF4E amount in the cell through 4E-binding proteins. Yeast has

additional 4E-binding proteins that differ from their mammalian counterparts in terms of their 4E-binding mode (Grüner et al. 2018).

Several steps of translation initiation were characterized using yeast as a model system, such as scanning and the factors involved in start codon selection (Altmann and Linder 2010).. Because the translation process is conserved from yeast to human (and yeast eIF4E functions highly like other metazoan and mammalian counterparts, given that eIF4E knockouts in yeast can be restored with murine and *D. melanogaster* eIF4E). Yeast remains an attractive model organism for characterizing translation, given its relative simplicity in genetics before moving on to the mammalian system (Altmann and Linder 2010).

The advent of ribosome profiling has allowed determination of translational efficiency of mRNAs transcriptome-wide *in vivo* (Ingolia et al., 2012). Furthermore, ribosome profiling has been applied to investigate how mRNAs depend on individual translation initiation factors such as eIF4B for their efficient translation genome-wide (Sen et al., 2016). Such studies have also shown that eIF4A dependence in mammals is correlated with the 5′ UTR secondary structure and G-quadruplex structures (Wolfe et al., 2014, Rubio et al., 2014). Moreover, these translatome profiling studies demonstrate vast heterogeneity in translational efficiencies across the transcriptome, which support a model of mRNA selection during translation. While it is well-established that mRNA features contribute to translation initiation (Hinnebusch et al. 2016; Leppek et al.

2018), the mechanistic basis of this differential dependence of mRNA translational efficiency on a particular initiation factor is unknown.

Translation initiation is a multi-step process that is inherently complex, involving more than a dozen initiation factors and various transient intermediates. Molecular dynamics and conformational changes that take place in the order of seconds play a huge role in the fidelity of translation (Prabhakar et al. 2017). Because initiation involves numerous transient intermediates involving more than a dozen factors, it is difficult to characterize the kinetics. Furthermore, detailed characterization of the earliest step (eIF4E-cap binding) and the role of the m^7G cap and poly(A) tail in stimulating eIF4F-mediated cap recognition is limited, even though this interaction is part of a rate-limiting step (Shah et al. 2013). Elucidating the distinct contributions of individual factors to cap binding remains a key challenge to understanding how mRNAs are selected for translation. In addition, the eIF4F-mRNA complex formation is too dynamic to be effectively characterized by conventional biochemical techniques. Previous rapid-reaction data has indicated rapid cycling between the cap-bound and unbound forms of eIF4E (Slepenkov et al. 2008*,* von der Haar and McCarthy 2002), which is ideally characterized by single-molecule approaches which can detect the formation of a highly dynamic complex in real time, while observing different populations in the same experiment.

eIF4F is implicated in viral infection, and its activity is dysregulated in several diseases and select forms of cancer. The cap-binding subunit eIF4E plays an

important role in controlling cell growth (Sonenberg and Gingras 1998). The complex members show aberrant activity in specific types of cancer, making them attractive targets for suppression of cancer cells' growth. Thus, the components of this complex are extensively being targeted for cancer therapy (Pelletier et al. 2015, Graff et al. 2008). eIF4E and eIF4A remain attractive targets, due to the observation that they appear to be overproduced/overactive in malignancy (Graff and Zimmer 2003). eIF4E is required for the translation of several oncogenic mRNAs, which require higher eIF4E/eIF4F activity more than other mRNAs, depending more on eIF4F for their translation (Silvera et al. 2010). Overexpression of eIF4E has been demonstrated to drive malignant transformation of cells and is associated with poor prognosis (Mamane et al. 2004). Although eIF4E is a global regulator of translation, it can selectively increase translation of a specific set of transcripts (Fischer 2009, Graff and Zimmer, 2003).

In vivo experiments utilizing snapshots of this interaction have suggested that eIF4F interacts differently with different mRNAs, ultimately affecting their translation efficiency (Costello et al. 2015). Other approaches that utilize eIF4E cross-linking to the cap structure have also been developed, certain motifs have been demonstrated to increase eIF4E interaction when present near the cap structure (Jensen et al. 2021). eIF4E also promotes functional folding of eIF4G (Hershey et al. 1999). However, little is known about the dynamics of this interaction of eIF4E with full-length mRNAs, and how of this variability is an

inherent property of eIF4F and its factors. Although the eIF4F-mRNA complex formation is critical for translation initiation, little is known about the rate of formation, or the lifetime of this complex, and whether it can vary between mRNAs (Sokabe and Fraser 2019). The rate of formation of this complex would kinetically control the downstream steps on initiation, and the lifetime of this complex would determine how long the mRNA is activated for ribosome recruitment. Past studies included kinetics and thermodynamic analysis using cap analogs (lacking an mRNA body) or fragments of other eIF4F subunits (Niedzwiecka et al. 2004 , Niedzwiecka et al. 2002, von der Haar et al. 2000, Slepenkov et al., 2008, Slepenkov et al. 2006). Thus, no information is available on the dynamics of this interaction on full-length mRNAs and thus how mRNA-to-mRNA variability in those dynamics impacts translation and its regulation.

In this study, we extensively characterized the eIF4F-mRNA interaction using biophysical methods. Using yeast as a model system, we designed an experimental approach to report real-time interactions between eIF4F subunit eIF4E and the mRNA cap structure in vitro using recombinant eIF4E and purified mRNAs at the single-molecule level. We first used this approach to examine the interaction of eIF4E with selected yeast mRNAs. The system uses single-molecule FRET (smFRET) between mRNA labeled with a donor fluorophore and the eIF4E protein labeled with an acceptor fluorophore, using the classic Cy3-Cy5 FRET pair which can be used to study the binding of one biomolecule to

another (Hwang et al. 2009). We combined this with zero-mode waveguide technology to allow for a higher concentration of fluorescent proteins and higher throughput (Chen et al. 2014), which we used to measure the interaction on populations. This ZMW-based approach has been used for sequencing of DNA, studying translation from bacterial ribosomes, studying telomeric DNA synthesis by the telomerase reverse transcriptase, and steps of IRES-mediated and canonical eukaryotic translation initiation (Wang et al. 2019; Choi et al. 2016; Duss et al. 2018, Petrov et al. 2016, Hentschel et al. 2021). Binding of eIF4E to mRNAs is readily detected through bursts of FRET between the mRNA and the protein, and the experimental approach allows for addition of different initiation factors to probe how they affect the dynamics of eIF4E-mRNA interaction.

The approach described above results in a molecular movie of this complex forming and dissociating in real time, at the single molecule level. Such use of single molecule methods makes it possible to discern differences in subpopulations of biological molecules (e.g., a transient vs. stable complex, or differential factor composition within the system under study), unavailable when conducting bulk experiments, where only the average of the population would be observed (Tinoco and Gonzalez 2011). We first describe this approach for only eIF4E, then extend to other eIF4F subunits with smFRET and other multicolor assays which probe eIF4E binding to mRNAs together with eIF4A. The multicolor

assays probe formation of the eIF4F complex and the order of dissociation of the eIF4E and eIF4A factors from the mRNA and each other.

Results

Development of a smFRET-based assay platform to study interactions between eIF4E and full-length mRNAs

We first picked different model mRNAs to study for eIF4E-mRNA interaction, based on their past behavior in in vivo studies (*NCE102, JJJ1 , HSP30, HXT2*). We aimed to compare eIF4F-mRNA dynamics on mRNAs with variable *in vivo* eIF4E binding. This necessitated selecting a representative set of mRNA candidates from the ~6.600 genes in the *S. cerevisiae* genome (Hirschman et al., 2006).

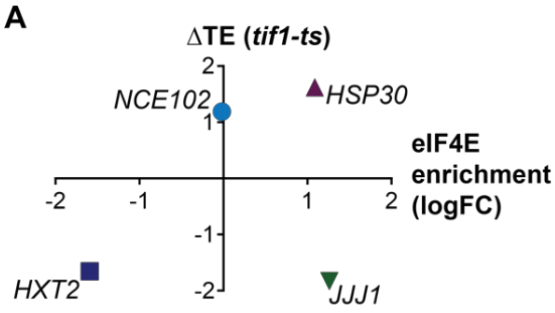

Figure 1.1. Candidate mRNAs used for the study. Selection of mRNAs with varying *in-vivo* enrichment in eIF4E•eIF4G and translation dependence on eIF4A, as measured by Costello *et al.* (2015), and Sen *et al.* (2015).

To look at specific eIF4F-mRNA binding, we examined a previously published RIP-seq dataset that quantifies eIF4E-mRNA interaction transcriptome-wide, and allows for comparing and contrasting between eIF4E-enriched (*JJJ1*, *HSP30*) and eIF4E-depleted (*NCE102*, *HXT2*) mRNAs that also have varying affinity for other initiation factors such as the poly(A) binding protein (Costello *et al.*, 2015, Figure 1.1.). Because we also aimed to define effects of eIF4A, from potential model mRNAs selected according to the RIP-seq data, we only looked at mRNAs with translation efficiencies that depended exclusively on eIF4A (*HXT2*, *JJJ1*). Later, additional mRNAs were added to obtain a larger sample size and variable length when contrasting between how mRNAs of different properties interact with eIF4E (*MIM1, SSA1, GIC1*). We then PCR-amplified the DNA corresponding to this transcript from yeast genomic DNA and transcribed the selected genes into mRNA using T7 RNA polymerase. The isolated mRNAs were then treated with a recombinant capping enzyme to add a 5′ cap structure, and poly(A) polymerase, to add a poly(A) tail and yield a mature mRNA. The added poly(A) tail appears to be around ~100 nt, based on gel electrophoresis (Figure 1.2C). For a sample of the mRNAs, we also measured the in vitro capping efficiency via nuclease treatment which selectively degrades uncapped RNA (Figure 1.2B). The enzymes for this processing are commercially available, although we usually purify the T7 polymerase in our laboratory.

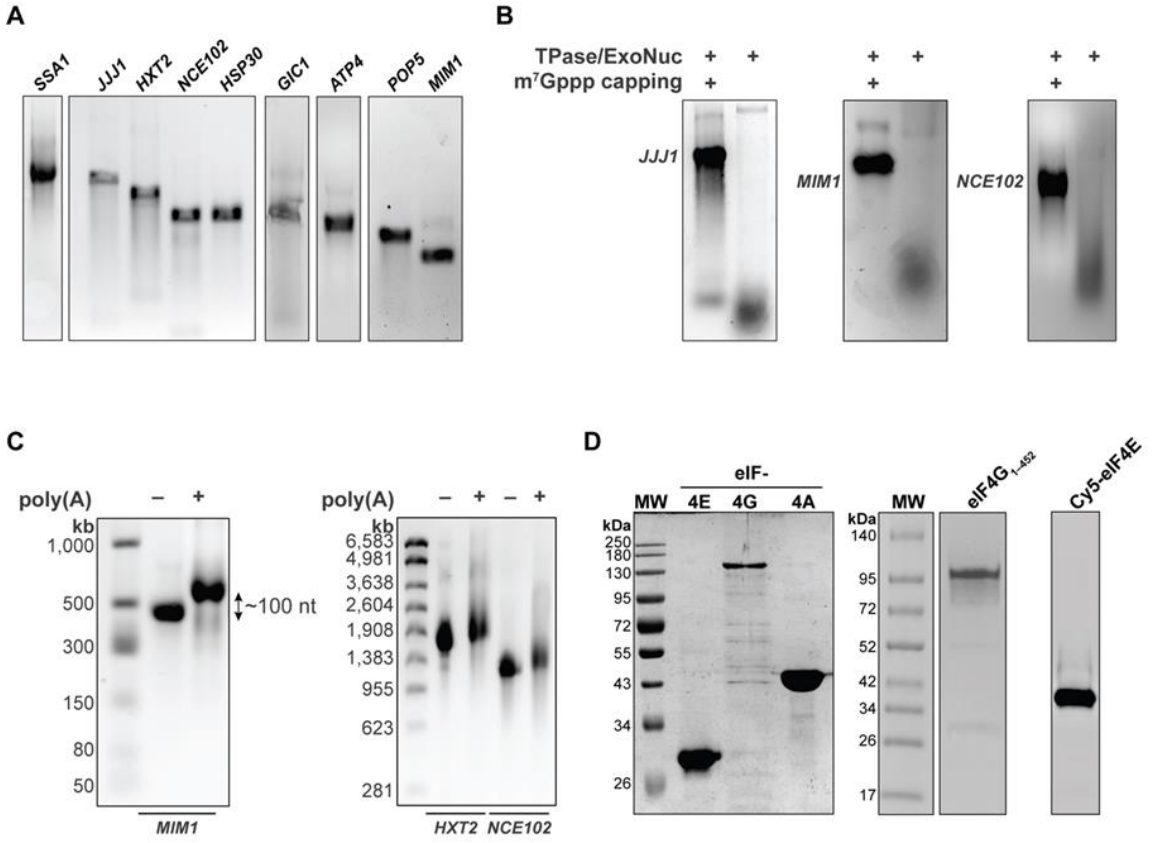

Figure 1.2. Preparation of mRNAs and recombinant proteins. A**.** Representative agarose gel electrophoresis of mRNA transcripts after capping and polyadenylation. B. Analysis of mRNA capping stoichiometry by dual enzymatic treatment with RNA 5' polyphosphatase and RNA 5′ terminator dependent exonuclease. Uncapped mRNAs are selectively degraded upon this treatment. C. Analysis of mRNA poly(A) tail length. D. SDS-PAGE analysis of purified recombinant eIF4F factors.

The isolated mRNAs were subjected to an annealing reaction with a fluorescent oligonucleotide, biotin-5′-$(dT)_{45}$-3′-Cy3 oligonucleotide. A biotinylated d(T) oligonucleotide (45 nucleotides) was ordered with a 3' amine, which reacts readily with the NHS-ester derivative of common organic dyes that can act as part of FRET pairs. The single-molecule imaging approach requires the RNA of interest be tethered on a glass surface to be able to track binding of a protein. The biotinylated oligonucleotide targets the mRNA poly(A) tail and therefore can be used for many different mRNAs. After conducting an annealing reaction, the mRNA of interest can then be immobilized onto the surface of zero-mode waveguides and will be labeled with a FRET donor at the 3' end. We then prepared fluorescently labeled eIF4E to act as a FRET acceptor for monitoring the interaction (Figure 1.1.). The A124C mutant of wild-type yeast eIF4E is inserted into a pET28-based expression vector, also adding a polyhistidine tag at the N-terminus. The single cysteine mutation allows for site-specific labeling of the eIF4E protein. The mutant eIF4E protein can be expressed and purified using *E. coli*, and fluorescently labeled using Cy5-maleimide, which was described previously (O'Leary et al., 2013). Upon preparation of fluorescently labeled mRNA and eIF4E, the binding can then be monitored using single-molecule FRET between fluorescent mRNA and eIF4E (Figure 1.2.A,B). The binding is detected through cycles of FRET between the RNA and protein (e.g, appearance and disappearance of FRET). FRET can also be used to detect conformational changes and measure distances within a biomolecule via monitoring the

efficiency, however this system only probes for total appearance and disappearance of FRET. This allows individual binding and dissociation events to be observed and fitting the dwell times of many binding and dissociation events allows us to obtain the rate constant for eIF4E-mRNA cap binding and dissociation. While the tag is at the opposite end of the mRNA, we have been able to monitor the interaction as the 5′ and 3’ ends of purified mRNAs appear to be close when they are refolded in solution. This signal was previously this signal for oligoribonucleotides where the FRET donor was ~40 nt from the cap (O’Leary *et al.*, 2013). Here, we instead used the same signal eIF4E-cap binding for full-length mRNAs (~0.4 – 2 kb).

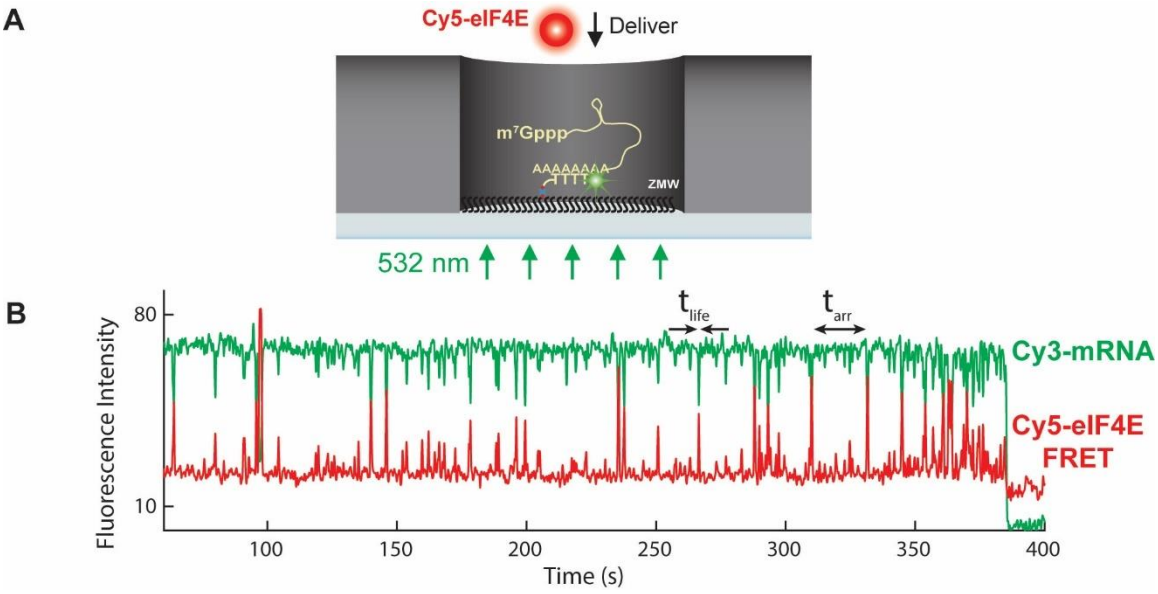

Figure 1.2. Real-time monitoring of eIF4E-mRNA interaction on full-length yeast mRNAs. A. Selection of mRNAs with varying *in-vivo* enrichment in eIF4E•eIF4G and translation dependence on eIF4A, as measured by Costello *et al.* (2015), and Sen *et al.* (2015). B. Schematic of single-molecule FRET experiment to detect binding of fluorescently-labeled eIF4E to surface-immobilized, fluorescently-labeled mRNA. C. Sample smFRET trajectory showing eIF4E–mRNA interaction in the absence of other eIF4F components. Purified recombinant eIF4E (labeled with a FRET acceptor) is delivered to single mRNAs (labeled with a FRET donor) immobilized at the bottom of zero-mode waveguides to detect real-time binding. Binding of eIF4E to the mRNA leads to an appearance of FRET, and this is apparent in the fluorescence time trajectories leading to a decrease in donor fluorescence intensity with an increase in acceptor fluorescence intensity at the same time. The transient bursts of FRET indicate cycles of binding and dissociation for the eIF4E-mRNA interaction. Data from many binding events can be fit to an exponential model, and fitting data from many binding events allows for calculation of the macroscopic rate constants for the eIF4E-mRNA interaction. Different mRNAs with variable behavior in vivo can be tested in the experiments to generate the kinetics and compared in terms of their eIF4E interaction profiles (their eIF4E association as well dissociation rates, corresponding to how well eIF4E binds the particular mRNA).

The imaging approach uses zero-mode waveguides and a commercially available Pacific Biosciences RS II DNA sequencer (Chen et al. 2014). While originally built for DNA sequencing, the instrument is inherently a microscope that conducts single-molecule imaging and can be customized for single-molecule experiments of different types, involving immobilization of a biotinylated molecule at the bottom of the zero-mode waveguides. The previous approach used TIRF microscopy (O'Leary *et al.*, 2013), which allowed observation of the eIF4E-mRNA interaction on oligonucleotides. However, the imaging platform based on the Pacific Biosciences DNA sequencer has several advantages: one is the high concentration of fluorescent ligand the user can add into the system (due to the use of zero-mode waveguides that restrict the illumination volume even further than TIRF microscopy), allowing observation of more binding events and generating more data. This is particularly important for molecules that interact slowly, since less binding would be observed at lower concentrations, rendering it difficult to conduct the experiment and observe sufficient binding for data analysis. Furthermore, the instrument is high throughput, imaging ~150.000 single molecule reactions in parallel in ~20 minutes (for a typical 10-minute movie, preparing the chip and data acquisition). This allows for generation of large amounts of single molecule data/time trajectories in a short amount of time, ideal for studying protein-RNA interactions due to the ability to make many measurements in parallel.

Dynamics of eIF4E interaction vary between messenger RNAs

We wanted to determine how much eIF4E interaction varies between mRNAs. The pulses of FRET that occur upon delivery allow for calculation of the rate of formation and the lifetime of the eIF4E-mRNA complex. Because each FRET event is a cycle of binding and release, fitting many binding events to a model (exponential fitting) allows one to obtain the macroscopic rate constants for the interaction and the equilibrium dissociation constant (Figure 1.3). The eIF4E-mRNA interaction typically exhibits rapidly reversible binding and dissociation on all mRNAs tested, lasting around ~1-2 s. The binding rate of eIF4E can be compared between mRNAs using this approach, determining whether the binding and dissociation rates vary significantly.

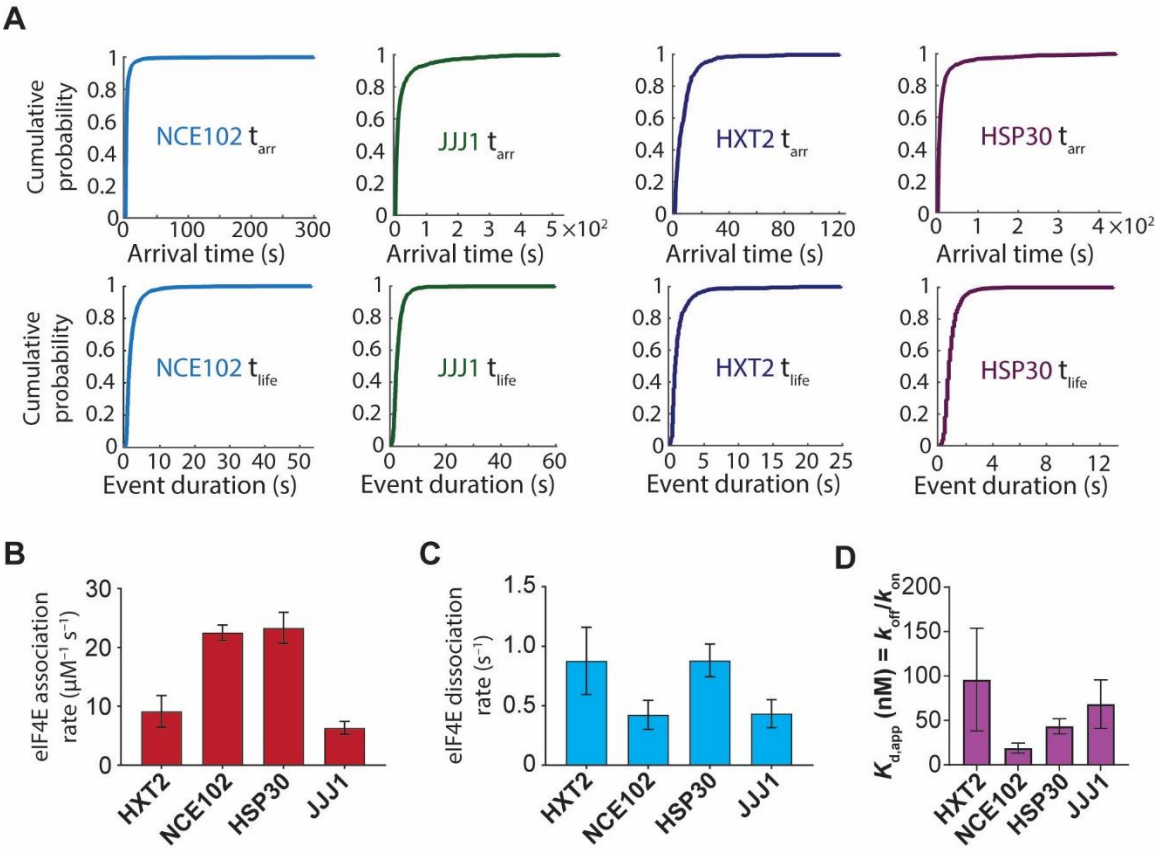
A
Cumulative probability
NCE102 t_arr
JJJ1 t_arr
HXT2 t_arr
HSP30 t_arr
Arrival time (s)
NCE102 t_life
JJJ1 t_life
HXT2 t_life
HSP30 t_life
Event duration (s)
B
eIF4E association rate (μM⁻¹ s⁻¹)
C
eIF4E dissociation rate (s⁻¹)
D
K_d,app (nM) = k_off/k_on
HXT2
NCE102
HSP30
JJJ1

Figure 1.3. Kinetics of eIF4E-mRNA interaction on full-length yeast mRNAs. A. eIF4E–mRNA association rates quantified from exponential fitting of arrival-time and lifetime cumulative distribution functions. Error bars reflect the standard errors of the mean for three replicates of an experiment where the eIF4E–mRNA binding rate is measured across at least 100 mRNA molecules. B. eIF4E–mRNA association rates from the experiments C. eIF4E–mRNA dissociation rates from the experiments. D. eIF4E–mRNA equilibrium dissociation constants computed from the rates. Purified recombinant eIF4E (labeled with a FRET acceptor) is delivered to single mRNAs (labeled with a FRET donor) immobilized at the bottom of zero-mode waveguides to detect real-time binding. Binding of eIF4E to the mRNA leads to an appearance of FRET, which is apparent in the fluorescence time trajectories leading to a decrease in donor fluorescence intensity with an increase in acceptor fluorescence intensity at the same time. The transient bursts of FRET indicate cycles of binding and dissociation for the eIF4E-mRNA interaction. Data from many binding events can be fit to an exponential model, and fitting data from many binding events allows for calculation of the macroscopic rate constants for the eIF4E-mRNA interaction, as well as the equilibrium dissociation constant. The equilibrium dissociation constant for the eIF4E-mRNA interaction (obtained through dividing the dissociation rate of eIF4E by the association rate) varies between ~20 and ~120 nM on the mRNAs we tested, which is consistent with previous measurements made on shorter oligonucleotides (Figure 1.3D). Different mRNAs with variable behavior in vivo can be tested in the experiments to generate the kinetics and compared in terms of their eIF4E interaction profiles (their eIF4E association as well dissociation rates, corresponding to how well eIF4E binds the particular mRNA). These rates are then correlated to mRNA features such as length, and in vivo data (Figure 1.4, Figure 1.5.).

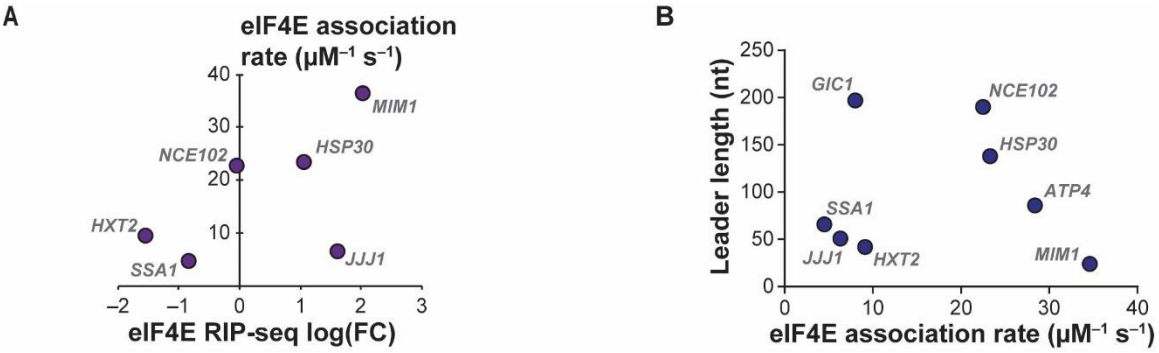

Figure 1.4. Correlation between eIF4E binding rates and in vivo affinity. E. A weak correlation between eIF4E-mRNA association rates were observed across the sample. F. No correlation was observed between 5′ UTR length and eIF4E association rate.

The kinetics of formation of the eIF4E-mRNA complex varied between four mRNAs (Figure 1.2), ranging from ~6 to ~23 μM^{-1} s^{-1} (highest for *HSP30*, *NCE102* and lowest for *JJJ1*). The dissociation rate was less variable, ranging from ~0.4 to ~0.9 s^{-1}. While we initially had four model mRNAs for study, we later added different mRNAs of different sizes and structural propensity near the 5′ end (0.4-2.1 kb). The range of association rates then increased, ranging from ~4 to ~34 μM^{-1} s^{-1}. We observed that eIF4E-mRNA association rates were correlated with ORF length and total length, where shorter mRNAs bind eIF4E faster (Figure 1.4.). These results suggested that the rate of formation of the eIF4F complex, but not the lifetime, control variable eIF4E-mRNA interaction. Thus, the eIF4E-mRNA interaction is high-affinity, although it dissociates rapidly when formed.

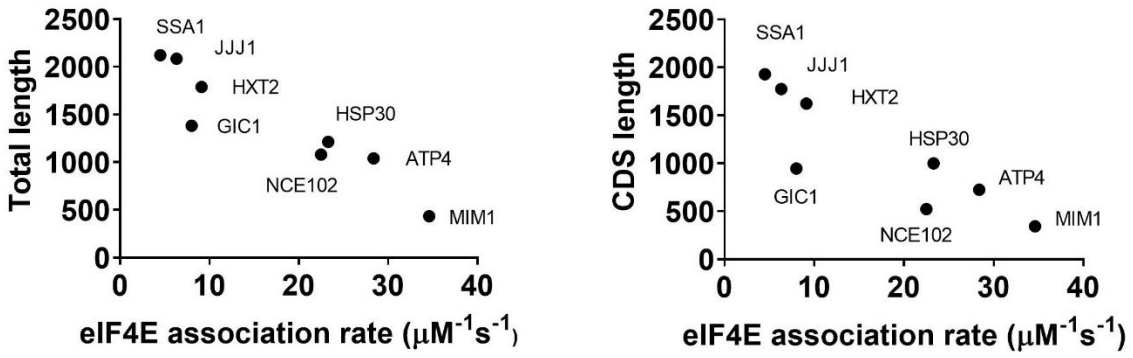

Figure 1.5. mRNA ORF length/total length reduces the eIF4E-mRNA association rate. Left: mRNAs with shorter ORFs bind eIF4E faster, clearly observed when the mean association rate for each mRNA is plotted alongside the ORF length. **Right:** Since most of the mRNA length consists of the open reading frames for this set of mRNAs (*NCE102* mRNA being the only exception), a similar correlation holds for the mRNA length. Both correlations are statistically significant, where the total mRNA length correlates better to the eIF4E association rate. Data includes eight mRNAs (*JJJ1, NCE102, HXT2, MIM1, SSA1, GIC1, HSP30, ATP4*).

Determining the kinetics eIF4E-mRNA interaction at the transcriptome level

The experiments outlined above involve in vitro transcription of a specific mRNA, and monitoring the eIF4E-mRNA interaction (e.g., monitoring the interaction on many copies of the same RNA, Figure 1.6.). We have also been interested in whether the eIF4E-mRNA interaction can be monitored at the global scale within the same experiment. Instead of T7 RNA polymerase-based in vitro transcription of an mRNA template, we isolated native mRNA from wild-type yeast culture using acid phenol-chloroform extraction and hybridized it to the same fluorescent, biotinylated oligonucleotide and captured total mRNA on the surface of ZMWs (Figure 1.6., 1.7.). This allowed us to distinguish between kinetics at the global

level vs. on many copies of the same transcript. This experiment acts as a global RNA-binding assay that computes the variability of eIF4E-mRNA interactions at the population-wide level. This can then be contrasted with the variability observed when eIF4E is binding to many copies of the same transcript.

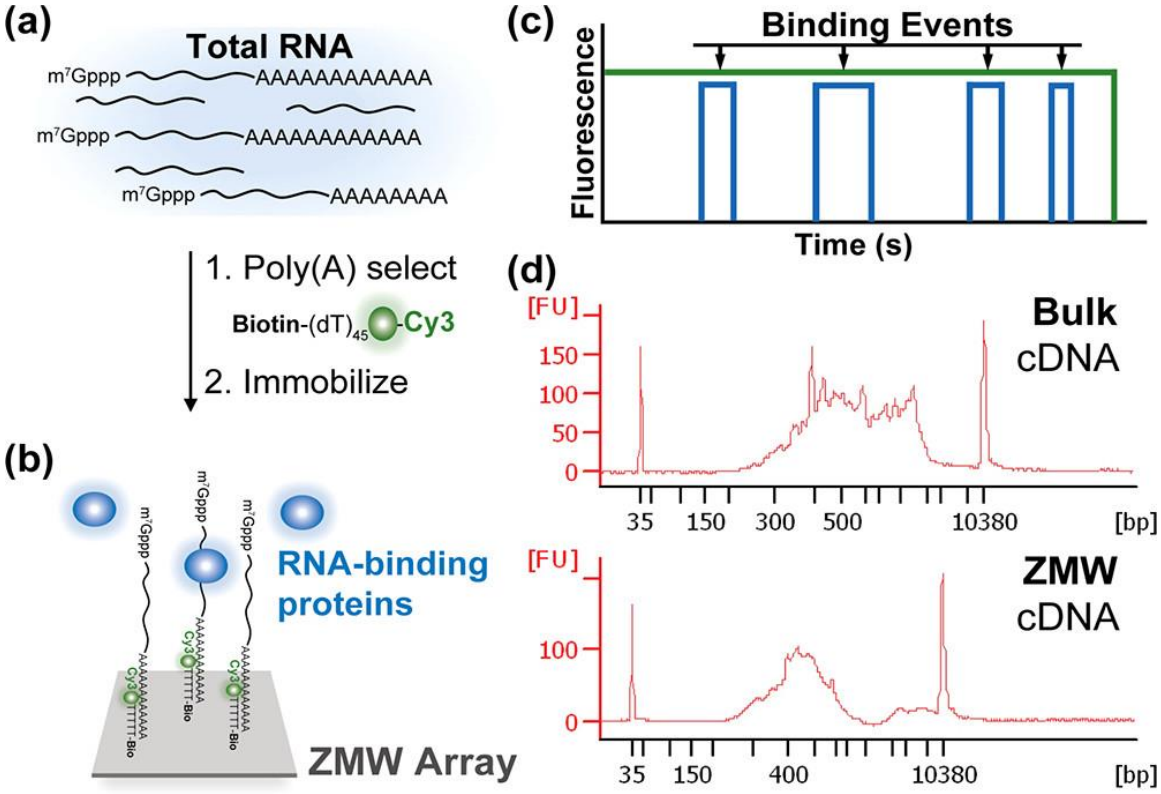

Figure 1.6. Experimental approach to analyze single-molecule eIF4E-mRNA interaction dynamics on transcriptome-derived mRNA populations. Total RNA is isolated from yeast, then subjected to a hybridization reaction using a biotinylated, fluorescently labeled d(T) oligonucleotide, which binds to the poly(A) tail present of messenger RNAs. The resulting mRNA pool is captured on the surface of a zero-mode waveguide using a biotin-NeutrAvidin-biotin interaction. Binding of fluorescently labeled RNA binding proteins can be detected through pulses in the fluorescent signal (either co-localization of RNA and protein fluorescence, or a FRET signal). The size distribution of mRNAs immobilized on the zero-mode waveguide can be visualized through reverse transcription and cDNA library generation, and electrophoresis of the resulting library.

We assessed the size of mRNAs that immobilize in the zero-mode waveguides through RT-PCR and assessed the size distribution resulting cDNA library compared to mRNA that was not immobilized, finding that it has a bias for shorter mRNAs, which could be due to diffusion-related effects in ZMW loading (Figure 1.5). We also subjected this cDNA library to RNA sequencing using an Illumina-based sequencing approach and found that about ~50% of the transcriptome can be detected on the waveguide. We also detected individual genes with variable expression through RT-PCR, confirming the presence of different transcripts of varying abundance in cells (Figure 1.7.). The observed immobilization bias could likely be mitigated by fractionating the mRNAs based on size, and then repeating the experiments, where the immobilization bias based on size would be reduced, or not using a diffusion-based loading method. We repeated the same experiments using eIF4E and eIF4E together with eIF4A in the presence of ATP as a proof of principle, determining the kinetics of eIF4E-mRNA interaction, computing an average and the range of the dynamics when eIF4E is binding to a pool of mRNAs with and without eIF4A. The effect of adding another protein could also be monitored, where adding eIF4A+ATP produced a detectable change in the kinetics of eIF4E-mRNA interaction in replicate experiments on the same batch of RNA.

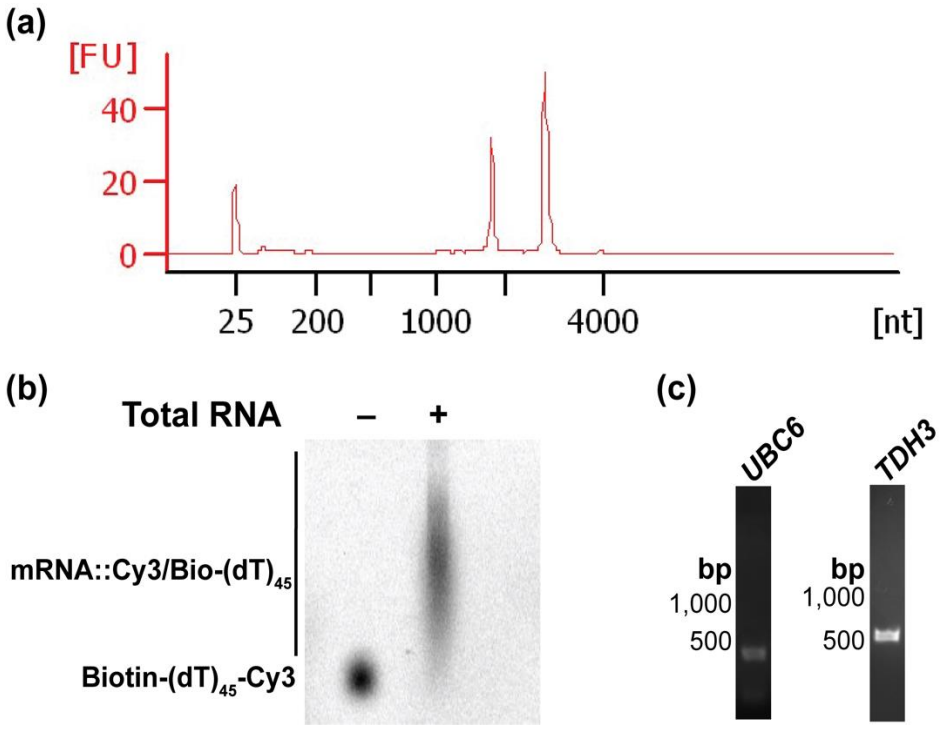

Figure 1.7. Preparation of Saccharomyces cerevisiae total RNA. (a) BioAnalyzer analysis of total RNA preparation. The dominant peaks confirm the presence of intact ribosomal RNA. (b) Hybridization of immobilization/fluorescent labeling oligo (biotin-5'-$(dT)_{45}$-3'-Cy3) to total mRNA, assayed by TBE-agarose electrophoresis with imaging for Cy3 oligo fluorescence. (c) Single-gene PCR analyses of ZMW-derived cDNA library, confirming the presence of mRNA for highly expressed TDH3 (GAPDH) and UBC6 (~0.13-fold expression relative to GAPDH in publicly available RNA-seq data.

eIF4E–mRNA interaction throughout a population of immobilized mRNAs was characterized by rapidly reversible binding and dissociation of the protein, monitored through the same smFRET signal (Figure 1.7, 1.8.). Single-molecule fluorescence trajectories for each mRNA can therefore be used to determine the arrival times between FRET events, and their durations. The arrival times can then be subjected to exponential fitting to extract the rates of eIF4E binding and dissociation across the population, calculating different parameters. Arrival times typically showed a double-exponential distribution, with a fast arrival rate contributing >80% of the total amplitude in the cumulative distribution function. This is consistent with a stochastic, Poisson-type sampling process for eIF4E–mRNA binding. Event-duration distributions were more complex but were typically dominated by an exponential distribution. These results support a two-state equilibrium-binding model for yeast and human eIF4E.

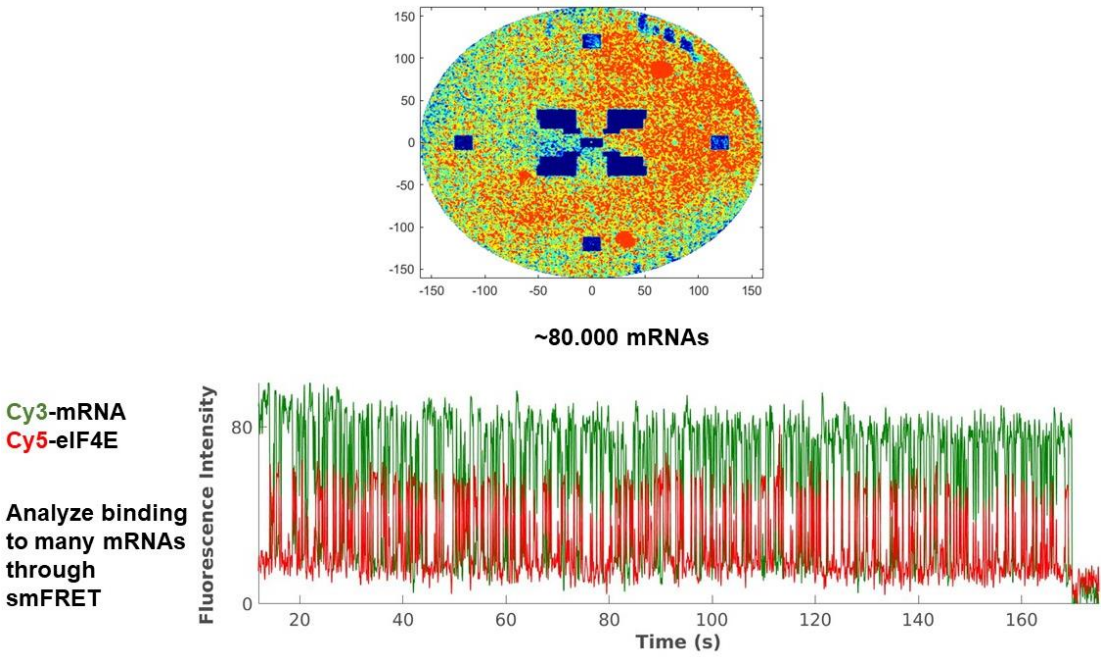

Figure 1.8. Example results from mRNA hybridization and capture on the zero-mode waveguides. Top: A fluorescent intensity heatmap of mRNAs immobilized onto the zero-mode waveguide and an example smFRET trace for the interaction is also presented, where eIF4E rapidly binds to and dissociates from the mRNA.

We analyzed eIF4E interaction with 438 mRNAs chosen arbitrarily from the population (Figure 1.9a,b). We constructed a distribution of the number of times each mRNA bound to eIF4E during a 10-minute observation, as censored by FRET-donor photobleaching. The 5th and 95th percentiles of this distribution lay at 1 and 104 events, respectively, representing a ~100-fold variability in eIF4E binding (Figure 1.9e). The median mRNA bound to eIF4E 23 times, which scaled with eIF4E concentration. In contrast, distributions generated for similar populations of the JJJ1 and NCE102 transcripts showed variabilities of only ~26-

and ~18-fold. Thus, we propose that the ~100-fold variability reflects authentic kinetic diversity driven by mRNA identity. We extracted mean eIF4E–mRNA binding rates for each mRNA in the population, by fitting the arrival-time distributions for each mRNA to an exponential model (Figure 1.9). We excluded molecules with fewer than 10 observed binding events to ensure robust fitting.

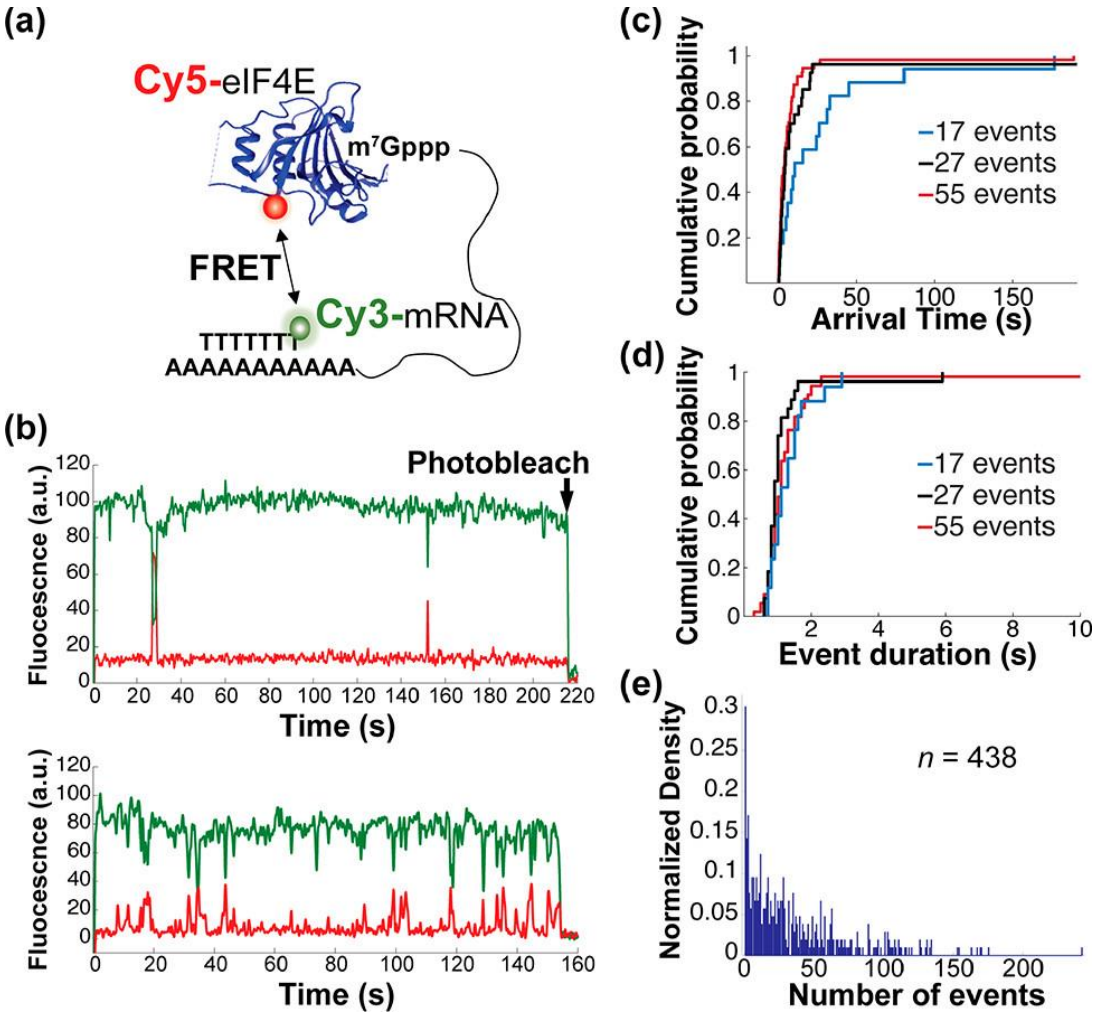

Figure 1.9. Real-time monitoring of eIF4E-mRNA interactions in mRNA populations. (a) Schematic of experimental approach showing smFRET signal between immobilized, Cy3-labeled mRNA and Cy5-labeled eIF4E cap-binding protein. (b) Representative single-molecule fluorescence trajectories for eIF4E-mRNA binding, contrasting mRNAs with few (top) and many (bottom) eIF4E-binding events. (c) Empirical cumulative probability distribution of eIF4E-mRNA arrival times from molecules showing 17, 27, and 55 events. (d) Empirical cumulative probability distribution of eIF4E-mRNA event durations on the same mRNAs as in panel (d). (e) Distribution of numbers of eIF4E–mRNA binding events observed across 438 mRNA molecules over a 10-minute observation. eIF4E binding to different transcripts throughout the transcriptome can be monitored through cycles of FRET. The molecules show vast heterogeneity, with some molecules binding eIF4E a small number of times, versus others that bind it many more times on a sample of several hundred mRNAs, which can be determined from smFRET traces. The rates for binding and dissociation can be obtained by fitting the dwell times to an exponential model.

eIF4E–mRNA association rate constants were distributed between 0.32 and 119 $\mu M^{-1}\ s^{-1}$, with a median of 5.0 $\mu M^{-1}\ s^{-1}$. The 5th and 95th percentiles of the distribution lay at 1.04 and 20.8 $\mu M^{-1}\ s^{-1}$, a ~20-fold variability. The fastest rate constants approached those for eIF4E binding to an unstructured, capped RNA oligonucleotide (O'Leary et al., 2013). Similar values were obtained in analyses that excluded trajectories with increasing goodness-of-fit stringency (Figure 10 A,B.). The 20-fold association-rate range thus likely sets a lower limit on the true transcriptome-wide diversity.

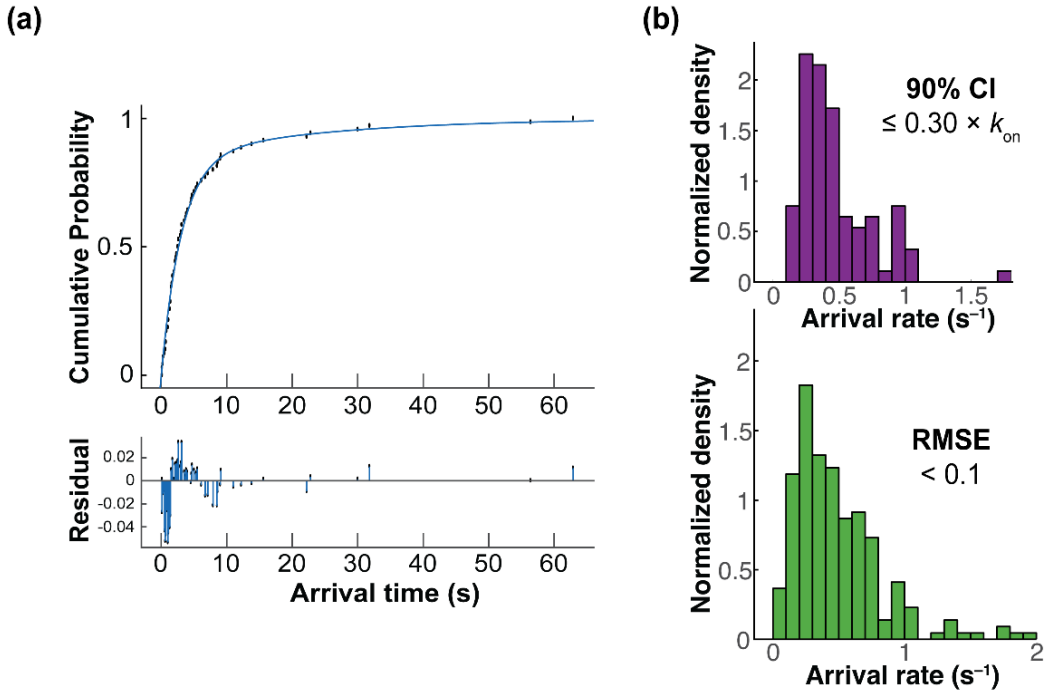

Figure 1.10. Goodness-of-fit analysis for on-rate parameters. (a) Top – representative exponential fit for eIF4E binding rate on an arbitrarily chosen mRNA with 70 binding events. Bottom – residual plot for the same fit. (b) Effects of increasing stringency of fitting on distributions of fitted arrival rates for 70 nM eIF4E binding to the transcriptome-derived mRNA population, as refined by (top) the 95% confidence intervals of the fitted rate parameter being separated by < 30% of the fitted rate, and (bottom) the root-mean-square error of the fit being <0.1.

Arrival times fitting to a >70% fast phase observed slow association rate across all experiments involving eIF4E may be partially caused by measuring the binding rate in zero mode waveguides (Duss et al. 2018). Steric hindrance of the eIF4E-cap interaction could occur from ZMW walls. However, this phenomenon has also been observed in previous SPR-based studies with short oligonucleotides (von der Haar et al., 2000), suggesting it may be partially due to aggregation of eIF4E. We seem to obtain a similar (possibly the same) slow

binding phase which does not respond to the eIF4E concentration. The slow arrival rate seems to be between 0.04-0.06 s^{-1} regardless of which transcript (or even across a pool of native transcripts) is used. Another possible reason is an RNA conformation that is less likely to bind eIF4E (e.g., misfolded or aggregated).

The approach described above computed a global range of association and dissociation (as a global RNA binding assay), however it is difficult to know exactly which RNA feature is causing this variability in cap binding. We therefore looked at the 5′ cap proximal structure, which was previously shown to impact eIF4E binding. For our analysis on how structural propensity near the 5′ mRNA cap may modulate eIF4E affinity, we examined a published dataset with in vitro measurements of mRNA secondary structure (PARS-seq) (Kertesz et al. 2010). Such measurements have used enzymatic treatment of isolated yeast RNA to determine the extent of secondary structure at various positions, giving an estimate for the likelihood for a specific region of the mRNA to be structured or unstructured. An unstructured region is expected to lead to higher accessibility and less of a steric block to the eIF4E-mRNA cap interaction (Cawley and Warwicker 2012), hence a higher eIF4E binding rate. We in-vitro transcribed four yeast mRNAs that have a different extent of structure near the mRNA cap (*SSA1*, *NCE102*, *GIC1*, *ATP4*): these have PARS scores for the first thirty nucleotides of 45.7 and -54.13, where a higher score indicates higher extent of structure. We found that the eIF4E association rates for these mRNAs to be ~4

μM^{-1} s^{-1} and ~28 μM^{-1} s^{-1}, respectively, i.e. more structure resulted in a slower binding rate (Figure 1.11a., Figure 1.12e). This correlation held for the 5'-proximal 20, 30, and 40 nucleotides (Figure 1.11a).

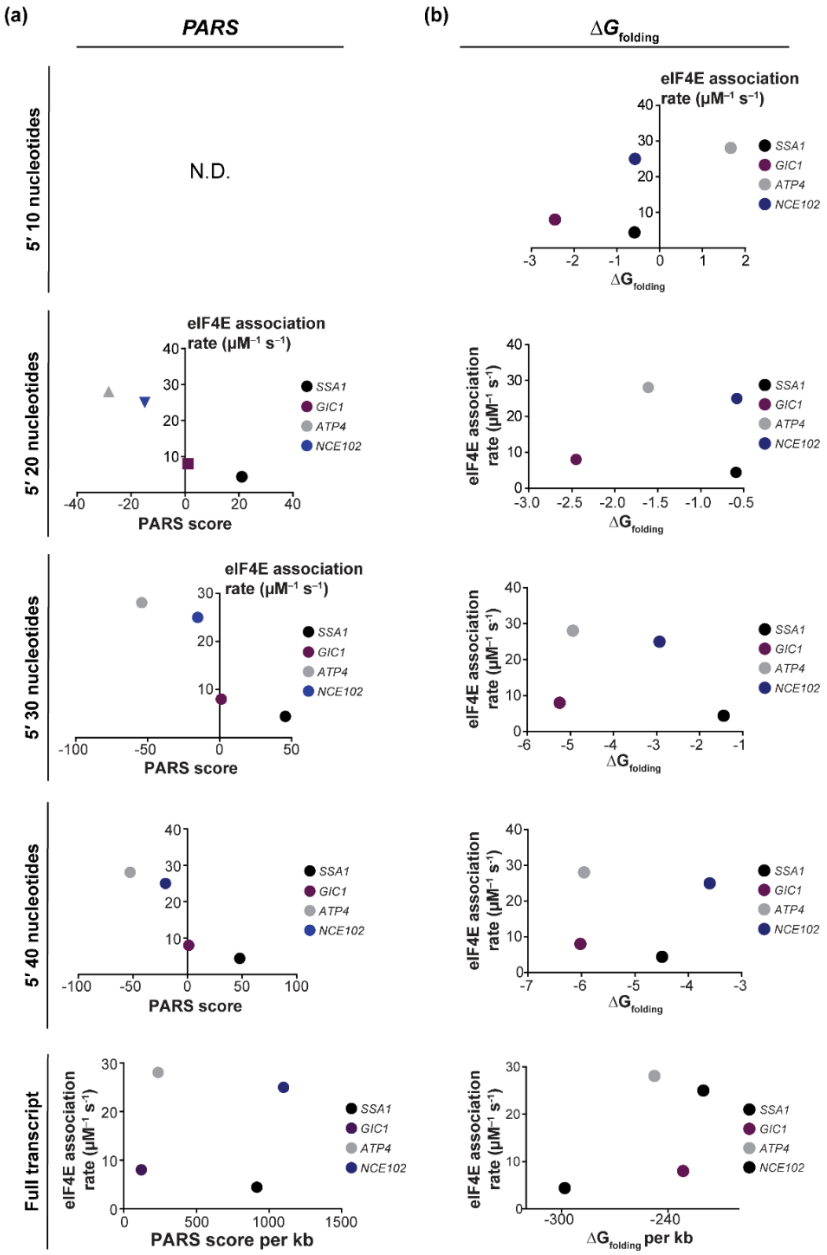

Figure 1.11. Correlation between mRNA structural properties and eIF4E-mRNA association rate. (a) Correlation plots for eIF4E-mRNA association rate and PARS score for the first 20–40 nucleotides and the entire transcript. Insufficient data were available to calculate the PARS score for the first 10 nucleotides. The *SSA1* and *ATP4* mRNAs bracket the range of available PARS scores transcriptome-wide. **(b)** Correlation plots for eIF4E-mRNA association rate and computed folding free energy change at 30˚C for the first 10–40 nucleotides and the entire transcript.

We also prepared and analyzed two mRNAs (*GIC1* and *NCE102*) previously shown to contain internal ribosome entry site (IRES) elements in the literature (Gilbert et al. 2007) and found the eIF4E association rates to be ~8 μM^{-1} s^{-1} for GIC1 and ~25 μM^{-1} s^{-1} for NCE102, which respectively lie above and substantially above the population median. We did not observe a correlation between the computed folding energy of the cap-proximal nucleotides and the binding rate of eIF4E (Figure 1.11b). Interestingly, the two IRES-containing mRNAs still sustain eIF4E binding at a high rate, even though they do not require cap binding for their translation. Since these IRES elements are activated at certain conditions (such as starvation, Gilbert et al. 2007), this may be a mechanism to ensure they get translated when canonical eIF4E/cap dependent translation is the dominant pathway. These results support a model where extent of mRNA structure kinetically controls eIF4E association rate. Steric blocking of the eIF4E–cap interaction by the mRNA body is expected to vary between mRNAs. Barriers to dissociation are expected to be less variable, reflecting similar structural environments for mRNA 5′ ends in the eIF4E·mRNA complex. Since the free energy change for eIF4E binding to cap structure analogs lacking an RNA body is dominated by interactions with the methylated guanine base and

the triphosphate bridge, differences in affinity imply barrier-height variation between distinct mRNA–protein encounters marked by early transition states.

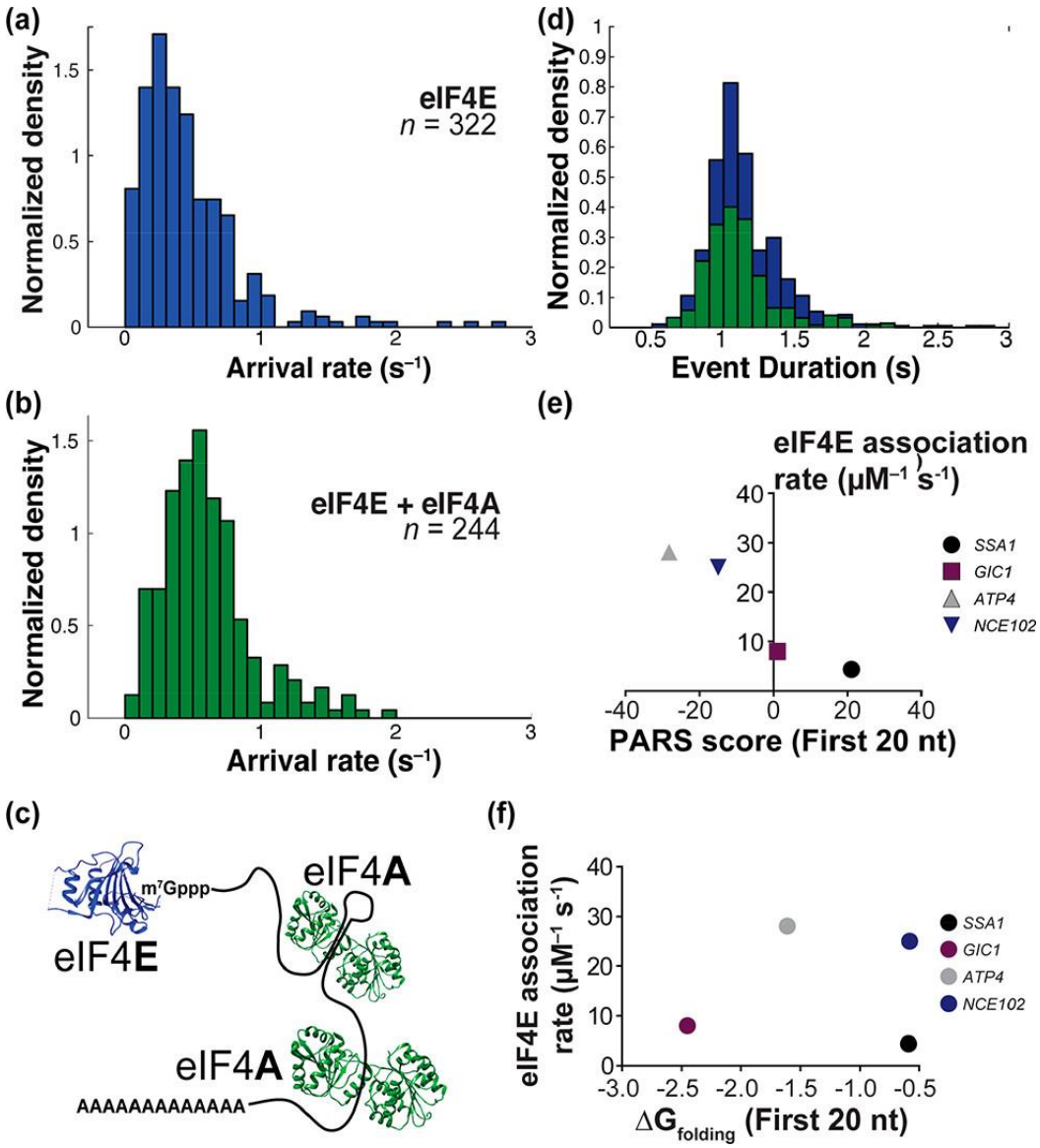

Figure 1.12. eIF4A affects the eIF4E binding rate transcriptome-wide. Distributions of protein-RNA binding kinetics. (a) On-rate distribution for eIF4E binding to 322 arbitrarily chosen mRNAs from the surface-immobilized population. (b) eIF4E-mRNA on-rate distribution in the presence of eIF4A. (c) Schematic with relative mRNA-binding sites of eIF4E and eIF4A. (d) Distribution of eIF4E-mRNA event durations in the absence (blue) and presence (green) of eIF4A. (e) Correlation of eIF4E-mRNA association rate with the extent of cap-proximal 20 nucleotides, as measured by PARS score. (f) Correlation of eIF4E-mRNA association rate with computed folding free energy change at 30˚C for the cap-proximal 20 nucleotides. Examples of the per-mRNA arrival rate distributions are contrast experiments where eIF4E alone was added, compared to eIF4E with eIF4A (and ATP). eIF4A can bind throughout the mRNA, presumably changing the structural landscape in an mRNA population. Addition of eIF4A, together with ATP, affects the arrival rate distribution, increasing eIF4E binding overall. Correlations of mRNA features to eIF4E binding rate on known specific transcripts are also provided. The extent of secondary structure near the mRNA 5′ end is negatively correlated with eIF4E-binding rate. The folding energy of nucleotides near the cap does not seem to correlate significantly with eIF4E-mRNA association rates on these set of mRNAs.

The ends of mRNAs are close in solution

We have also conducted some intramolecular FRET as a control to validate this signal (e.g., FRET between ends of RNAs in the absence of any protein). This is because the cap-binding protein can bind the mRNA without FRET between the fluorophores. Recent results suggest that mRNA folding brings the 5′ and 3’ ends within FRET distance in solution (2 – 8 nm for Cy3/Cy5) (Lai et al., 2018, Vicens et al., 2018). Hence, this also replicated results obtained previously in the literature, using mRNA sequences derived from yeast instead of mammals and viruses. To validate the smFRET signal described above, we conducted intramolecular FRET experiments (Figure 1.13.) that detect FRET between 5′ -3’ ends of mRNAs. In this case, mRNAs are labeled at the 5′ triphosphate moiety

according to a published method (Lai et al., 2018) instead of enzymatic capping with a capping enzyme. The mRNA is then poly(A) tailed as described in the Materials and Methods section. Instead of detecting binding of a protein to RNA via FRET (a FRET signal between protein and RNA), we measured the end-to-end distance of selected model mRNAs using intramolecular FRET (FRET between fluorescent dyes attached at either end). To this end, we used a derivative of an experiment described in the literature (Lai et al. 2018), using the same 5′ end labeling approach, but changing the 3' end labeling to hybridization at the poly(A) tail for consistency with previous eIF4E binding experiments. The mRNAs are labeled with a Cy3 (FRET donor) at the 5′ triphosphate, whereas a similar biotin-5′-(dT) $_{45}$-3′-Cy5 (using Cy5 fluorophore instead of Cy3) oligonucleotide is annealed to the 3' end and imaged in a smFRET experiment (Figure 1.12.). The results obtained in this experiment demonstrate that the mRNAs studied here fold into structures bringing the ends within FRET distance (8 nm). This was also demonstrated with viral RNAs that are a large (>1 kb) size using single molecule confocal microscopy (Leija-Martínez et al. 2014).

We tested four of the mRNAs used for our measurements (*JJJ1, NCE102, MIM1, HXT2*), which vary in length between ~0.4 to ~2.1 kb. We found that all of these mRNAs are likely to fold into structures that bring the mRNA ends within FRET distance, as computationally predicted and experimentally demonstrated for other mRNAs (Lai et al. 2018, Yoffe et al. 2011, Leija-Martínez et al. 2014). This

may be a global feature of mRNA sized RNAs, as argued in previous literature (Yoffe et al. 2011, Vicens et al., 2018). We found that the four mRNAs tested spend greater than two thirds of their lifetime (~67 to ~83%) in a FRET state (Figure 1.13). This contrasts with the mammalian mRNAs, which were found to be in a FRET state during the entire experimental period (Lai et al. 2018). The observed differences could be due to the base composition of yeast vs. mammalian RNA. A similar compaction was demonstrated in cells when translation was arrested through chemical inhibitors (Khong and Parker 2018).

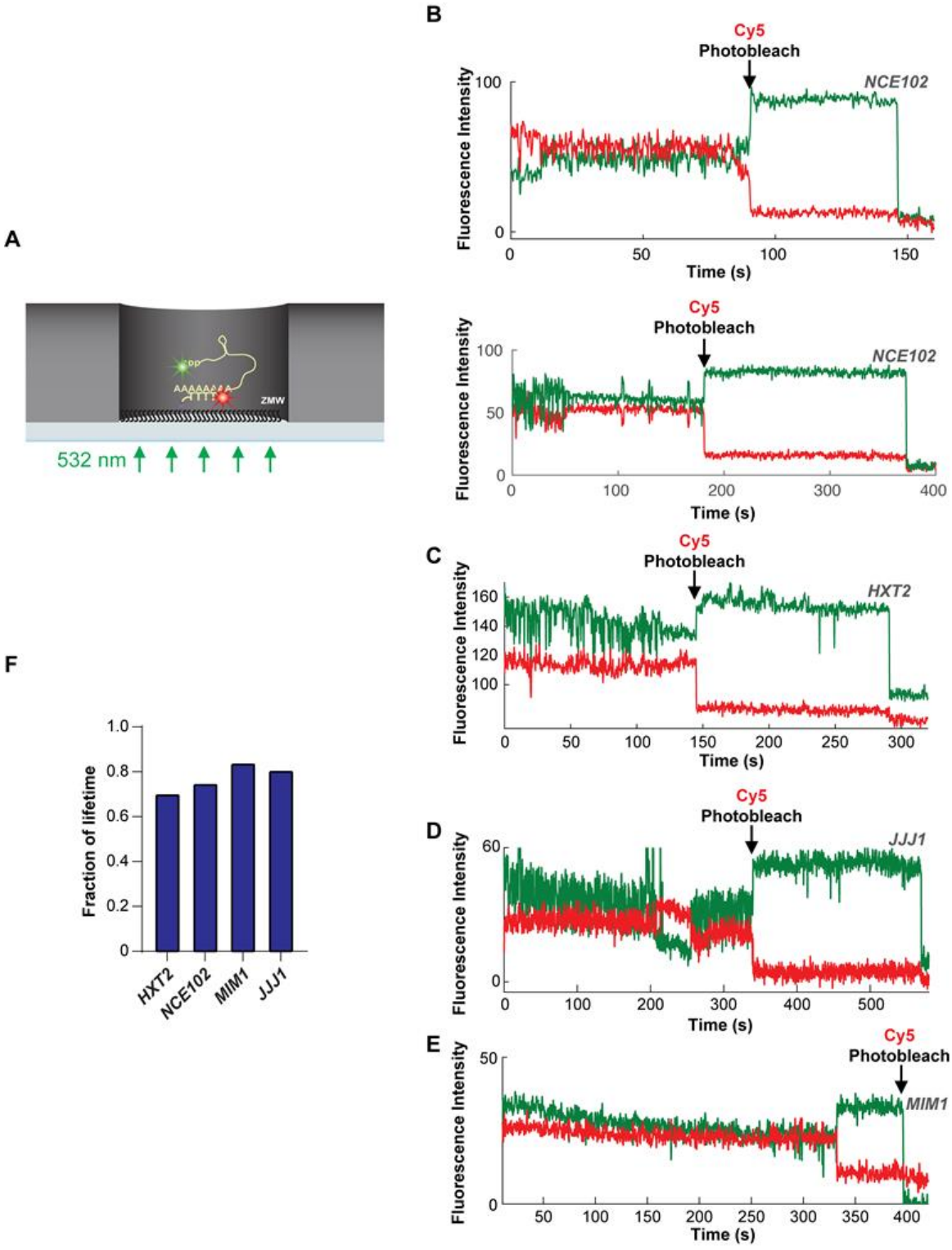
A
ZMW
532 nm
B
Cy5
Photobleach
NCE102
Fluorescence Intensity
Time (s)
C
HXT2
D
JJJ1
E
MIM1
F
Fraction of lifetime
HXT2
NCE102
MIM1
JJJ1

Figure 1.13. Intrinsic proximity of mRNA ends allows accurate determination of eIF4E–mRNA arrival rates. A. Schematic of intramolecular smFRET experiment to assess intrinsic mRNA end-to-end proximity. Uncapped mRNA is labeled through its 5' triphosphate group with a FRET donor (Cy3), and on its poly(A) tail with a FRET acceptor (Cy5), then surface-immobilized through poly(A) capture. **B–E.** Representative smFRET traces showing 5′ - to 3'-end FRET for yeast mRNAs: *NCE102*, panel B; *HXT2, C*; *JJJ1,* D; *MIM1*, E. Efficient smFRET is terminated by apparent acceptor photobleaching. **F.** Plot showing the fraction of Cy5 lifetime spent in a detectable FRET state for all four mRNAs.In vitro transcribed yeast mRNAs (containing a 5′ triphosphate) are labeled with a FRET donor at the 5′ end (Cy3) and an oligonucleotide containing a FRET acceptor is hybridized to the poly(A) tail near the 3' end. The labeling scheme results in a mRNA tagged with fluorophores on both end that serve as a FRET pair, and FRET between the two fluorophores can be detected, as well as conformational cycling between different FRET states.

Discussion

Variable recognition of the mRNA cap structure by eIF4E demonstrated on model mRNAs

The basal eIF4E-mRNA interaction is highly dynamic and varies between mRNAs. We have been able to measure differences between mRNAs using a smFRET-based assay. Our assay allows for comparing and contrasting between how different mRNAs interact with eIF4E in terms of rate. We found that eIF4E by itself binds mRNAs with variable affinities, consistent with past results and proposals in the literature (Sonenberg and Hinnebusch 2009, Costello et al., 2015, Truitt et al. 2015). Moreover, we found that the variation is largely due to differences in the rate at which eIF4E associates with the cap (the dissociation rate varies less). This basal eIF4E-cap association rate ranged over ~8-fold, from

~34 μM^{-1} s^{-1} to ~4.5 μM^{-1} s^{-1}; the upper values are reminiscent of eIF4E association with an unstructured, capped oligonucleotide (O'Leary *et al.*, 2013). mRNA length also appears to be the main determining factor that causes variable eIF4E binding along with secondary structure near the cap, at least when eIF4E alone is present in the experiment without additional eIF4F complex subunits.

It has long been known from earlier studies that mRNA structure can hinder eIF4E-cap binding through steric effects. However, past work has ascribed the block to the effects of cap-local structure (Pelletier and Sonenberg 1985). Similarly, we propose that global mRNA tertiary structure can also pose a steric block that defines an mRNA-specific rate of eIF4E association, along with mRNA 5′ cap-proximal structure. This may explain the anticorrelation between mRNA length and eIF4E binding rate. This suggests that longer mRNAs need to be chaperoned by other RNA-binding proteins to bind eIF4E faster. In either case, eIF4E alone can kinetically discriminate between mRNAs (or mRNA identity defines the binding). This fundamental property of the cap-binding protein likely allows cells to differentially regulate translation of mRNAs. In addition, eIF4E binding may help stabilize mRNAs by protecting them from degradation. This was not assessed in the current research but may be a potential mechanism for determining mRNA stability, e.g, mRNAs that bind eIF4E/eIF4F better would be more stable overall, preventing decapping by enzymes such as Dcp2 by

occupying the cap structure and preventing them from accessing the cap structure.

The eIF4E-mRNA interaction at the global scale

Modulation of cellular active eIF4E concentration is a major control mechanism for protein synthesis (von der Haar et al. 2004). However, not all mRNAs are equally sensitive to changing eIF4E levels; mRNAs with structured 5′ ends are particularly sensitive (Bhat et al. 2015). The heterogeneity observed here in eIF4E–cap association rates suggest a kinetic mechanism for this differential sensitivity: mRNAs with intrinsically fast association are likely to sustain eIF4E–cap binding sufficient to allow continued translation initiation even when the available concentration of eIF4E is reduced. Furthermore, recent work has implicated free eIF4A activity throughout the length of the mRNA as accelerating ribosome–mRNA recruitment (Yourik et al., 2017)

Our results suggest that this effect may be exerted even at the very initial steps of mRNA selection for translation, by enhancing binding of eIF4E to the mRNA cap structure. Our results further demonstrate that RNA-binding proteins, even when binding at remote sites, can modulate the eIF4E binding rate to the cap, presumably by inducing 3D conformational rearrangements. Although not a direct goal of our experiment, we found that mRNAs are likely to fold into compact structures even when RNA-binding proteins are present, replicating results

already present in the literature. This brings the ends close together (within FRET range, which would be <8 nm), possibly separated when initiation progresses, and many ribosomes are loaded on the mRNA. This may have implications for the re-initiation of a mRNA, by ensuring that the mRNA is in a “closed loop” by default and that the ribosomal particle remains proximal to the 5′ end at the end of elongation. This end-to-end communication is a feature of many different types of RNA across all domains of life (including viral RNAs), likely to facilitate different processes such as RNA processing, assembly of protein complexes and RNA decay (Vicens et al., 2018, Ermolenko and Mathews 2021). The approach presented here is performed on yeast RNA, however, the experiment also works on total RNA extracted from 293T cells in the same manner.

Overall, our results highlight how kinetic heterogeneity, determined by the sequence and structural information encoded throughout RNA transcripts, may contribute significantly to dynamic control of gene expression. In addition, a phenomenon that was observed both in many copies of the same mRNA and throughout pools of native mRNA, was that the eIF4E-mRNA interaction is highly transient (lasting around ~1-2 s). Translation initiation is thought to take longer, closer to tens of seconds (Ciandrini et al. 2013, Acker et al. 2009). Because translation initiation takes place at a longer timescale (around tens of seconds, although it can vary considerably between mRNAs), the eIF4E-mRNA dissociation rate consistently being over ~0.5 s suggested that additional factors

may be required to stabilize the interaction. eIF4E alone would not stay bound long enough to sustain translation initiation.

Chapter 2.

Contributions of eIF4G and eIF4A to eIF4E–mRNA interaction dynamics.

Introduction

The eIF4F complex that mediates translation initiation has two subunits in addition to eIF4E. eIF4G is a second subunit, which has direct interactions with eIF4E and eIF4A (Hinnebusch and Lorsch, 2012, Merrick 2015). Binding of eIF4E to eIF4G induces a conformational change thought to stabilize the interaction between eIF4E and the mRNA cap structure, which was shown previously via structural studies of apo-eIF4E as well as eIF4E in complex with the eIF4E-binding domain of eIF4G (Gross et al. 2003). This would facilitate the loading of the ribosome at the 5′ end. eIF4A, an ATP-dependent RNA helicase, is also a component of the eIF4F complex. Biochemical, genetic, and structural studies have also established that dynamic inter-subunit coordination is an important property of eIF4F function (Oberer et al. 2005, Feoktistova et al. 2013). However, a detailed kinetic framework for the molecular mechanisms of this coordination has not yet been established. Past studies of eIF4F–RNA interaction have utilized the intact heterotrimeric eIF4F complex purified from cell lysates (Kaye et al. 2009), precluding isolation of the effects of individual subunits.

Where complexes have been reconstituted from purified subunits, to isolate effects of individual subunits, kinetics were measured with capped oligonucleotides, or only partial eIF4G sequences were used that lack RNA-binding activity (Slepenkov et al. 2008, von der Haar and McCarthy 2002). How kinetics underpin the coordinated biochemical functions of the eIF4F subunits thus remains poorly understood. For example, while eIF4G was shown to greatly enhance eIF4E–cap affinity using crosslinking and pulldown assays and RNA-binding activity (Haghighat and Sonenberg, 1997, Yanagiya et al. 2009), it is not known whether this is due to acceleration of initial eIF4E–mRNA binding, to stabilization of the eIF4E•eIF4G•mRNA complex after initial binding, or a combination of both. A single-molecule platform is ideal for characterizing this interaction because it detects eIF4E-G-mRNA complex formation in real time elucidating the precise mechanism by which eIF4G may exert such an effect. Likewise, while eIF4G–eIF4A interaction stimulates the eIF4A ATPase and helicase activities by modulating eIF4A conformational cycling (Andreou and Klostermeier 2014; Harms et al. 2014), and eIF4A globally promotes cap recognition (Sen et al. 2015), the extent to which eIF4A activity contributes to cap binding rates on different mRNAs is unknown.

Another outstanding question is the division of labor between eIF4F-bound eIF4A and the order-of-magnitude cellular excess of free eIF4A (Duncan and Hershey 1983, von der Haar and McCarthy 2002) over the eIF4F-bound factors, is also not yet well understood, though the free eIF4A fraction is increasingly implicated as contributing to initiation in experiments looking at ribosome recruitment (Yourik et al., 2017, Chu et al. 2020). Indeed, although the function of eIF4A as an ATP-dependent RNA helicase is well established, the precise contributions of eIF4A ATP binding and hydrolysis to the dynamics of eIF4F-mRNA complex formation are not yet understood, along with their relative importance for eIF4F recognition of different mRNAs. More broadly beyond these examples for individual eIF4F subunits, the precise sequence of molecular events occurring in the eIF4F•mRNA complex prior to PIC recruitment is not fully known. To address this, we included other eIF4F factors in our assay, starting with eIF4G.

Results

eIF4G accelerates the binding rate of eIF4E to mRNAs

We first isolated recombinant eIF4G using an established procedure (Liu et al. 2019). Once included in our smFRET assay together with eIF4E, eIF4G accelerated eIF4E-mRNA association for all mRNAs tested (*NCE102*, *JJJ1*, *HXT2*, *HSP30*, *MIM1*, *SSA1*). However, the extent of acceleration differed by

mRNA, from ~7-fold for JJJ1 to ~2.3-fold for MIM1 resulting in rates from ~41 ± 7 μM^{-1} s^{-1} to ~88 ± 14 μM^{-1} s^{-1}. eIF4E binding remained faster for shorter mRNAs, though the range of rates was narrower than for eIF4E alone (Figure 2.1 A).

Figure 2.1. eIF4G1 accelerates eIF4E–mRNA binding in an mRNA-dependent manner. A. eIF4E-mRNA association rates in the absence (grey) and presence (red) of full-length yeast eIF4G1. B. eIF4E-mRNA association rates in the absence (grey) and presence (red) of eIF4G (1–452).

We also isolated an eIF4G1 fragment (eIF4G 1–452) containing the N-terminal RNA-binding domain but truncated immediately N-terminal to the eIF4E-binding domain (Figure 2.2). This fragment retains one of the RNA-binding domains, and hence some RNA-binding activity (Figure 2.2.).

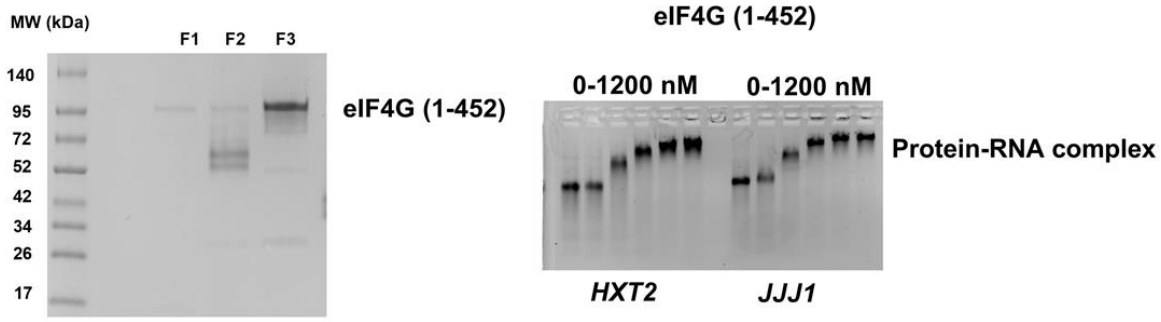

Figure 2.2. Preparation and activity of the eIF4G truncation. Left: Gel filtration separates the eIF4G fragment from contaminants. Right: The isolated eIF4G fragment binds the mRNAs used in our studies, which can be monitored via agarose EMSA, where the RNA binding causes a gradual mobility shift.

This fragment showed comparably accelerated eIF4E association, except for the HSP30 mRNA (Figure 2.1B). Experiments with uncapped (5'-triphosphate), polyadenylated NCE102 mRNA did result in eIF4E–mRNA FRET events (mean duration ~1 ± 0.31 s), but at only ~2% of the association rate relative to the capped mRNA (Figure 2.3A, B). When the N-terminal RNA-binding domain was removed further from this truncation (83-452), which abolishes its RNA-binding activity, no stimulation of eIF4E–mRNA binding was observed (Figure 2.3 C-E).

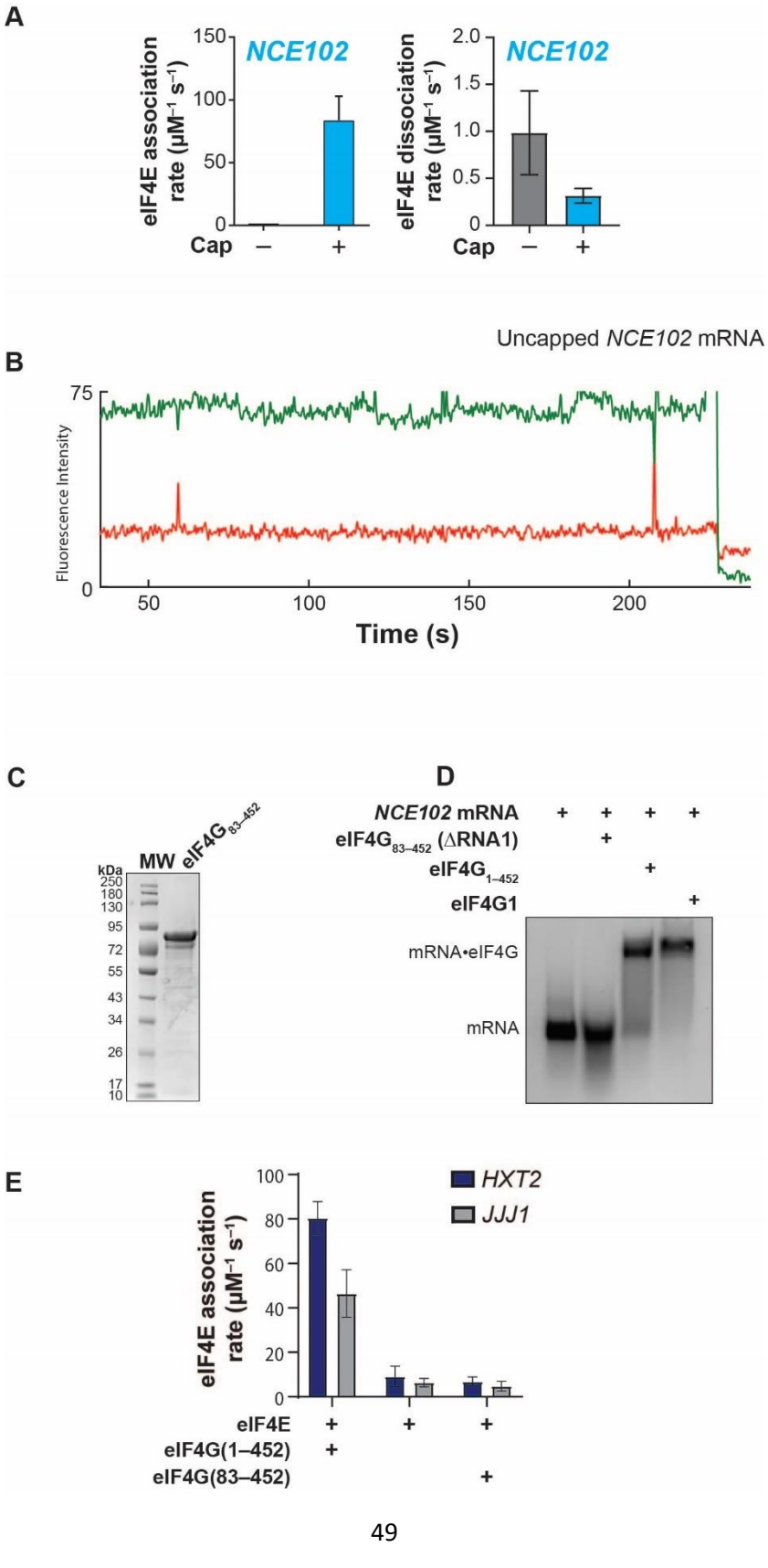
A
NCE102
eIF4E association rate (μM⁻¹ s⁻¹)
150
100
50
0
Cap – +
NCE102
eIF4E dissociation rate (μM⁻¹ s⁻¹)
2.0
1.5
1.0
0.5
0
Cap – +
B
Uncapped NCE102 mRNA
Fluorescence Intensity
75
0
50
100
150
200
Time (s)
C
MW
eIF4G83–452
kDa
250
180
130
95
72
55
43
34
26
17
10
D
NCE102 mRNA + + + +
eIF4G83–452 (ΔRNA1) +
eIF4G1–452 +
eIF4G1 +
mRNA•eIF4G
mRNA
E
HXT2
JJJ1
eIF4E association rate (μM⁻¹ s⁻¹)
100
80
60
40
20
0
eIF4E + + +
eIF4G(1–452) +
eIF4G(83–452) +

Figure 2.3. Analysis of eIF4E-G binding to uncapped RNA, and eIF4G (83-452). A. eIF4E-mRNA association rate on uncapped *vs.* capped *NCE102*, and eIF4E-mRNA dissociation rate on uncapped *vs.* capped *NCE102*. **B.** Representative smFRET trace from an experiment with uncapped *NCE102* and eIF4E•eIF4G1. **C.** SDS-PAGE analysis of purified $eIF4G_{83–452}$, which lacks the N-terminal RNA-binding domain. **D.** Analysis of RNA binding by full-length eIF4G and truncations, indicating reduction in RNA binding between full-length eIF4G and $eIF4G_{1–452}$, and loss of binding on further removal of the RNA-binding domain in $eIF4G_{83–452}$ relative to $eIF4G_{1–452}$. **E.** Comparison of eIF4E–mRNA association rates between $eIF4G_{1–452}$ and $eIF4G_{83–452}$, indicating that removal of the N-terminal RNA-binding domain abrogates acceleration of eIF4E–mRNA association.

Thus, direct eIF4G–mRNA interactions play a deterministic role in accelerating eIF4E–cap binding. The results are also consistent with previous results for mammalian eIF4F binding to RNAs, in that the affinity of eIF4F for RNA is driven dominantly by eIF4G (Kaye et al., 2009). The degree of acceleration also correlated significantly with CDS and total mRNA lengths (Figure 2.4A,B.) Shorter mRNAs showed less acceleration, even when including two additional mRNAs (*MIM1* and *SSA1*) to see if the correlation persists in a larger sample size and length differences.

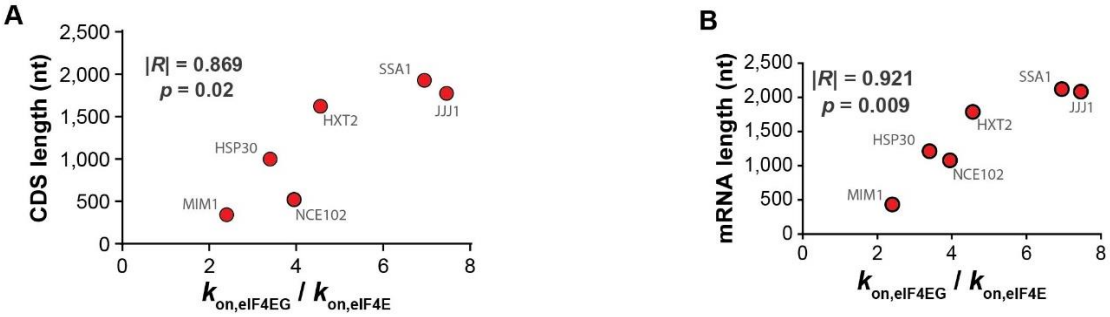

Figure 2.4. eIF4G stimulation of eIF4E binding depends on mRNA length. A. Fold-stimulation of eIF4E–mRNA association rate by eIF4G1, as a function of CDS length. B. Fold-stimulation of eIF4E–mRNA association rate by eIF4G1, as a function of mRNA length. Both correlations are statistically significant.

We previously showed that the extent of cap-proximal secondary structure impedes eIF4E–mRNA association in the absence of eIF4G, in an approximately linear anti-correlation over a wide range of secondary-structural propensities (Çetin et al., 2020). To investigate whether similar effects operate for eIF4E•eIF4G, we compared the eIF4E•eIF4G–mRNA association rates for mRNAs in our dataset that have well-defined PARS structural data (Kertesz et al. 2010), spanning the range of structuredness in their cap-proximal 30 nucleotides. *NCE102*, the mRNA with the least structured 5′ end (PARS score: –15.18), bound eIF4E•eIF4G with the highest rate: 89 ± 18 μM^{-1} s^{-1}. *SSA1*, which has a highly structured 5′ end (PARS score of 45.7), bound eIF4E•eIF4G the slowest, at 32 ± 4 μM^{-1} s^{-1}. An mRNA with intermediate cap-proximal secondary structure, *HXT2* (PARS score –6.38), also showed an intermediate eIF4E•eIF4G–mRNA association rate of 41 ± 7 μM^{-1} s^{-1}. Thus, cap-proximal structure that impedes eIF4E–mRNA association also impedes eIF4E•eIF4G–mRNA association.

eIF4G stabilizes the eIF4E-cap interaction on individual mRNAs

Our data were surprising in that, for eIF4E alone, cap-binding events were short relative to the initiation timescale (Acker et al. 2009, Palmiter 1975), contrasting with eIF4E remaining associated with the 48S ribosomal pre-initiation complex throughout scanning. Fast eIF4E dissociation would limit how long an intact eIF4F•mRNA complex is available for PIC recruitment. On the other hand,

different models have been proposed (Archer et al. 2016, Bohlen et al. 2020) in relation to whether eIF4E remains cap-bound as the mRNA 5' end enters the PIC mRNA channel. eIF4E remaining cap-bound, or dissociating and rapidly rebinding, would favor maintaining eIF4G bound to the mRNA 5′ end, and thus looping of the leader as it moves through the PIC in search of the start site. We therefore assessed how eIF4G impacted the eIF4E–cap binding duration.

eIF4G slightly or moderately lengthened transient eIF4E–mRNA binding events for most mRNAs (k_{off} = 0.35 ± 0.01 s^{-1} to 0.93 ± 0.25 s^{-1}, Figure 2.6A), resembling its effect on eIF4E binding to capped oligonucleotides. The effect varied between mRNAs, yielding a slightly narrower range of dissociation rates. However, the interactions remained transient on the initiation timescale.

Strikingly, though, a proportion of eIF4E-mRNA binding events lengthened by an order of magnitude in the presence of eIF4G (~10% – 34%, depending on mRNA). The effect was observed as double-exponential behavior (Figure 2.5 A-B) in the event-duration distribution.

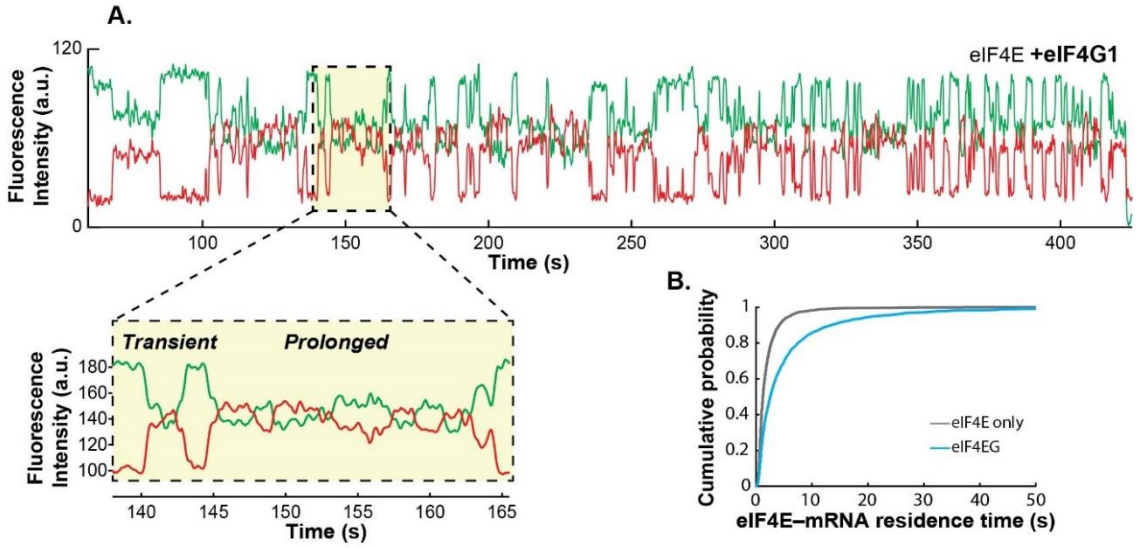

Figure 2.5. eIF4G1 allows the eIF4E-mRNA interaction to persist on the translation initiation timescale. A. Representative single-molecule fluorescence trace for eIF4E–mRNA binding in the presence of eIF4G1. The inset shows representative transient and prolonged events on an expanded time axis. B. Cumulative probability distributions of eIF4E–NCE102 mRNA event durations in the absence (grey) and presence (blue) of eIF4G1, showing appearance of slowly-dissociating events when eIF4G1 is present.

These long events were not observed with the eIF4G$_{1–452}$ fragment (Figure 2.6B), implying they result from direct eIF4E–eIF4G interaction. Increasing the eIF4G concentration to 1 μM did not increase the relative proportion of the longer events (Figure 2.6D.), arguing that the remaining transient events are not due to eIF4E–mRNA binding without eIF4G. Similarly, titrating the eIF4G concentration from 75 nM to 250 nM did not significantly alter the eIF4E–mRNA association rate, consistent with saturation of eIF4E in the eIF4E•eIF4G complex under our experimental conditions (Figure 2.5D.). As the Cy5 lifetime is greater than two minutes in our illumination conditions (observed in separate experiments labeling RNA), disappearance of FRET is unlikely to be due to Cy5 photobleaching.

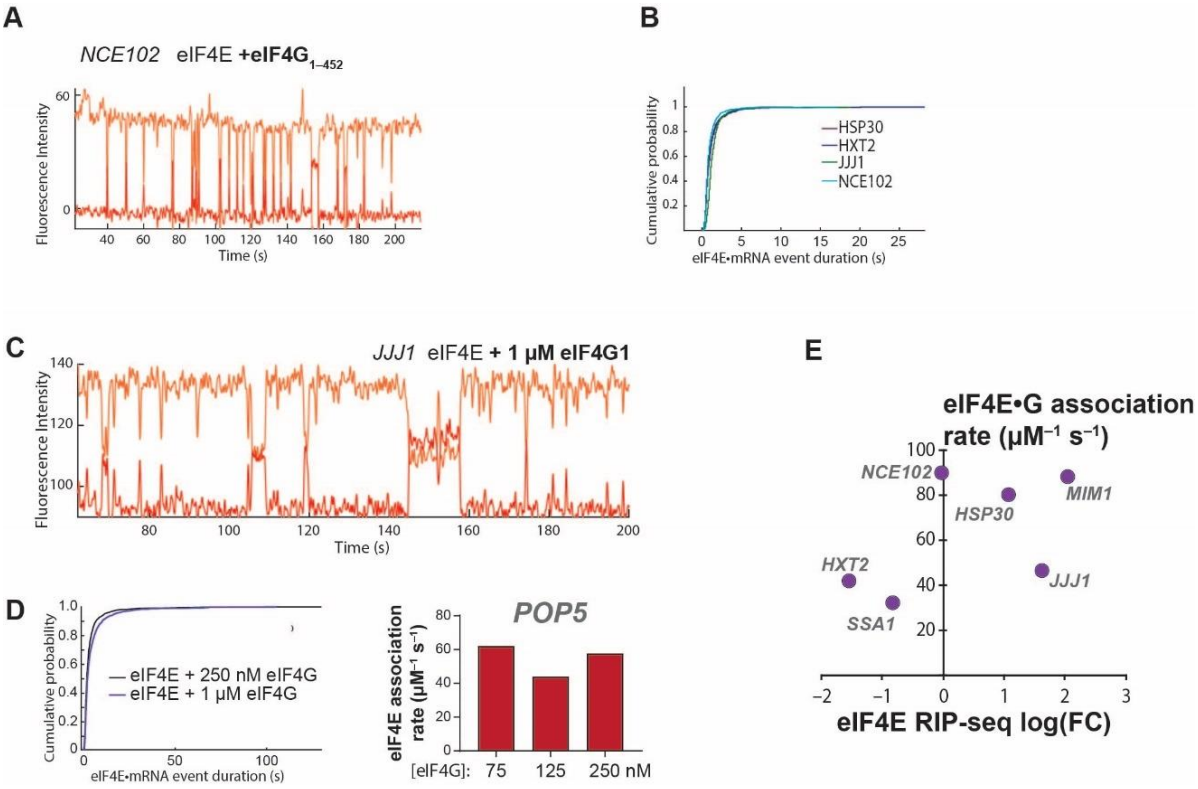

Figure 2.6. eIF4E–mRNA kinetics with varying concentrations of full-length eIF4G1, and eIF4G1 (1–452). A. Sample smFRET trajectory for eIF4E–mRNA binding in the presence of eIF4G1 (1–452). B. Cumulative distribution function of the eIF4E-mRNA interaction lifetimes in the presence of eIF4G1 (1–452). C. Sample smFRET trajectory for eIF4E–mRNA binding in the presence of 1 μM eIF4G1. D. Cumulative distribution function of the eIF4E-mRNA interaction lifetimes in the presence of 1 μM eIF4G1 for the *JJJ1* mRNA, and eIF4E–mRNA association rates on the *POP5* mRNA at varying concentrations of full-length eIF4G. E. Correlation of eIF4E–mRNA association rates in the presence of eIF4G with in-vivo eIF4E RIP-seq enrichment from Costello et al. (2015).

The dissociation rate for longer events varied between mRNAs (k_{off} = 0.03 ± 0.01 s^{-1} to 0.15 ± 0.01 s^{-1}, Figure 2.7B). Taken together, these results imply that the two dissociation events occur from two different states of the eIF4E•eIF4G•mRNA complex. The simplest possible interpretation for the identity of the second state is an alternative conformation in which one or more of the eIF4G RNA-binding domains have engaged the mRNA, leading to a higher energetic barrier for detachment of eIF4E from the eIF4E•eIF4G•mRNA complex, and thus the slower dissociation rate. Put otherwise, the data as a whole point to an accommodation mechanism where initial encounter of eIF4E•eIF4G with the mRNA through the cap structure precedes formation of more stable eIF4G–mRNA contacts.

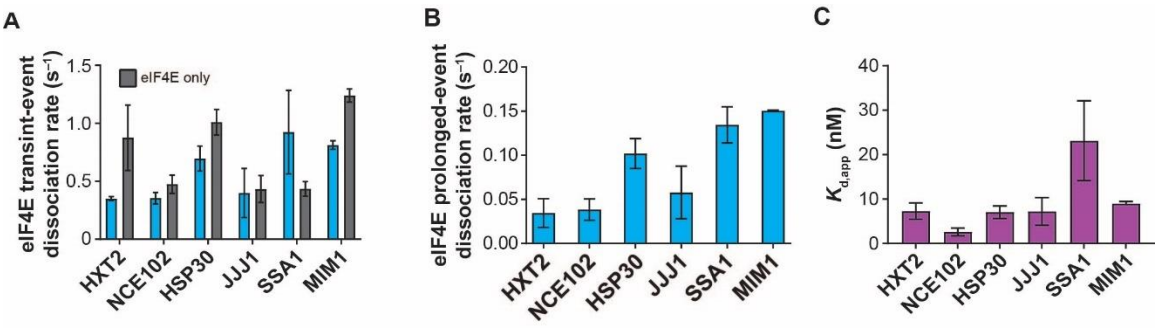

Figure 2.7. Dissociation kinetics and equilibrium dissociation constants for the eIF4E-mRNA interaction in the presence of eIF4G. A. Kinetics of eIF4E–mRNA dissociation for transient binding events in the presence (blue) and absence (grey) of eIF4G1. B. eIF4E–mRNA dissociation rates for long-lived binding events in the presence of eIF4G1. C. Apparent equilibrium dissociation constants for the eIF4E–mRNA interaction in the presence of eIF4G1.

These combined effects of eIF4G on eIF4E association and dissociation drastically enhanced the apparent eIF4E–cap affinity: $K_{d,app}$ values for the interaction were reduced ~4.8 – 15.8-fold (K_d range: 2.8 ± 0.9 nM to 23 ± 9 nM, calculated based on a weighted average of the two dissociation rate constants, Figure 2.7C.). As in the case of eIF4E alone, these equilibrium dissociation constants did not trend with the *in-vivo* RIP-seq eIF4E enrichments of the mRNAs, but, on the whole, the mRNAs enriched in eIF4E again showed faster association rates (Figure 2.6E.). This would also be consistent with eIF4E•eIF4G–mRNA association being kinetically, rather than thermodynamically controlled *in vivo*.

Taken together, our data show that the eIF4G RNA-binding activity is central to both accelerating cap recognition and allowing it to persist on the initiation timescale. While the accelerative effect is more pronounced on longer mRNAs, shorter mRNAs still bind eIF4E•eIF4G faster, at rates inversely dependent on cap-proximal secondary structure. Also, while eIF4G induces long eIF4E–mRNA binding events, the association rates still confer greater variability in eIF4E–mRNA interaction dynamics between mRNAs.

eIF4A alone can stimulate eIF4E-mRNA binding

We recently reported that free yeast eIF4A (without being bound to an eIF4F complex) increased eIF4E association rates across mRNA populations (Çetin et al., 2020). However, it remained unclear whether this effect operates to the same extent for all mRNAs, or whether they are affected differently. Moreover, the relationship of this phenomenon to translation dependence on eIF4A was unclear.

We added eIF4E to the immobilized mRNAs together with eIF4A (2 μM) in the presence of 2.5 mM ATP. eIF4A and ATP addition indeed accelerated eIF4E-cap association for each mRNA (Figure 2.8A.). However, the fold-acceleration ranged from ~1.2 (very little stimulation) to ~4.2 -fold, yielding rates from ~25 μM^{-1} s^{-1} to ~53 μM^{-1} s^{-1}. As observed for eIF4G, the fold-acceleration of eIF4E–mRNA binding induced by eIF4A again was greater for longer *vs.* shorter mRNAs. No significant acceleration was observed when ATP was removed from the experiment (Figure 2.9.). Acceleration was the same when ATP was substituted by the slowly-hydrolyzable ATP analog ATP-*y*-S (Figure 2.8C).

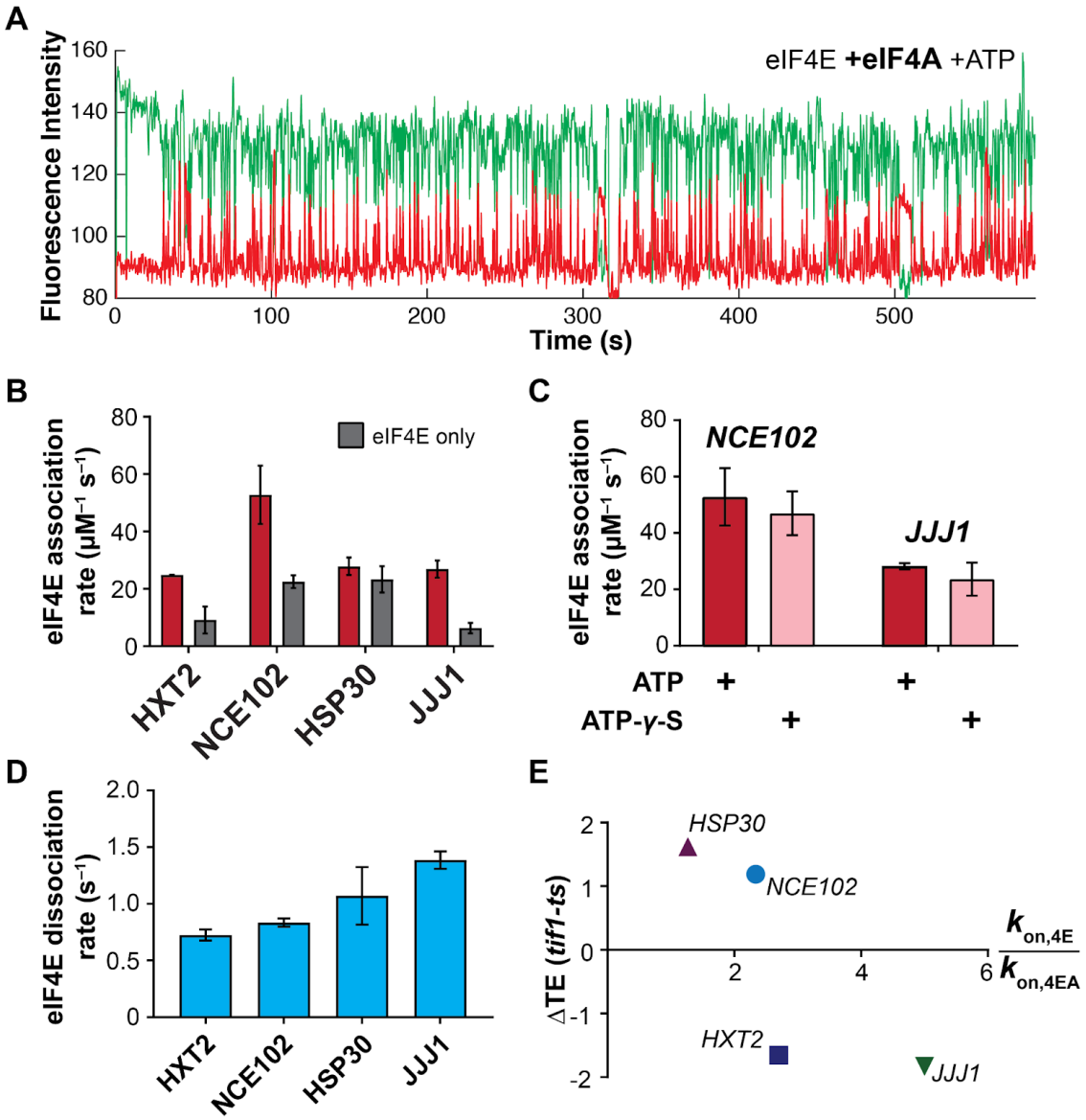
A
eIF4E +eIF4A +ATP
Fluorescence Intensity
160
140
120
100
80
0
100
200
300
400
500
Time (s)
B
eIF4E only
eIF4E association rate (μM⁻¹ s⁻¹)
80
60
40
20
0
HXT2
NCE102
HSP30
JJJ1
C
NCE102
JJJ1
eIF4E association rate (μM⁻¹ s⁻¹)
ATP
ATP-γ-S
D
eIF4E dissociation rate (s⁻¹)
2.0
1.5
1.0
0.5
0
HXT2
NCE102
HSP30
JJJ1
E
HSP30
NCE102
HXT2
JJJ1
ΔTE (tif1-ts)
k on,4E / k on,4EA

Figure 2.8. Free eIF4A with bound ATP stimulates eIF4E–mRNA association independently of eIF4G. A. Representative single-molecule trace showing eIF4E–mRNA interaction in the presence of 2 μM eIF4A and 2.5 mM ATP. B. eIF4E-mRNA association rates in the presence (red) and absence (grey) of eIF4A and ATP, compared with eIF4E-only rates. C. eIF4E–mRNA association rates in the presence of eIF4A and ATP or ATP-γ-S, for the *NCE102* and *JJJ1* mRNAs. D. eIF4E–mRNA dissociation rates in the presence of free eIF4A and ATP. E. Relationship between translation-efficiency dependence on eIF4A and the fold-increase in eIF4E–mRNA association rate induced by free eIF4A and ATP. eIF4A accelerates the rate of eIF4E-mRNA binding when ATP is present in the experiment. The dissociation rates increase slightly. ATP-γ-S is able to accelerate the eIF4E-mRNA binding rate almost as much as ATP, suggesting ATP binding by eIF4A is sufficient to observe the acceleration effect. Finally, the fold-stimulation of eIF4E-mRNA association rates by eIF4A correlates with the dependence of these mRNAs on eIF4A for their translation.

We performed the ATP-*γ*-S experiments on two of the mRNAs (NCE102 and JJJ1, which show the greatest stimulation of eIF4E binding by eIF4A) and obtained the same results (Figure 2.8C.). Nucleotide binding to eIF4A is thus sufficient to induce the acceleration observed. Meanwhile, the lifetime of eIF4E–mRNA binding events with free eIF4A and ATP remained a similar length relative to the eIF4E-only condition (Figure 2.8D), which we had also observed previously across mRNA populations.

Additionally, we correlated the eIF4E–mRNA association rates for each mRNA with ribosome-profiling data (Sen et al. 2015) for the mRNAs' eIF4A–translation efficiency dependence. eIF4A indeed accelerates eIF4E binding to a greater degree for mRNAs that are hyperdependent (HXT2, JJJ1) on eIF4A compared to hypodependent mRNAs (HSP30, *NCE102*) (~1.8 vs. 3.6-fold, Figure 2.8E). This strongly suggests that an eIF4G-independent role of eIF4A in promoting cap

binding contributes significantly to translation efficiency right from the outset of initiation.

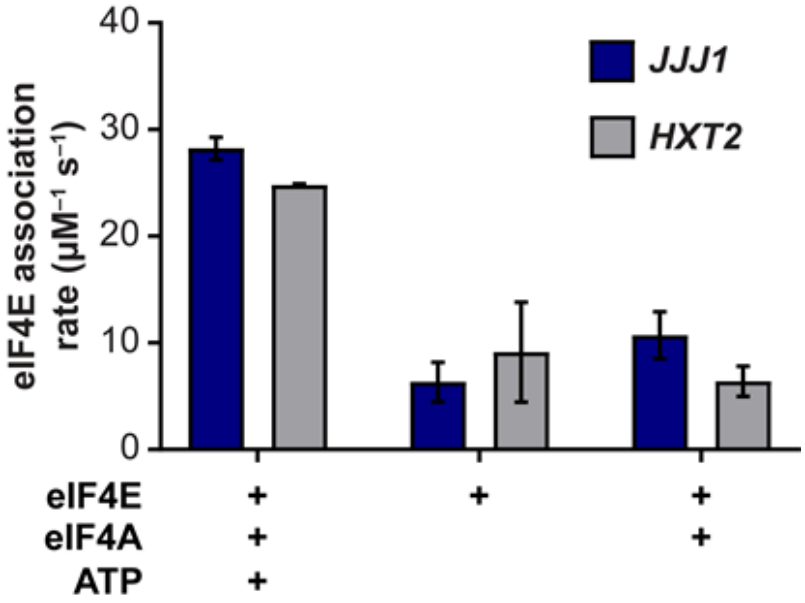

Figure 2.9. ATP is required for stimulation of eIF4E–mRNA association by free eIF4A. eIF4E–mRNA association rates in the absence of eIF4A, and with eIF4A in the absence and presence of ATP. The *JJJ1* and *HXT2* mRNAs were chosen for this experiment as they show the greatest fold-acceleration of eIF4E–mRNA association by eIF4A (ATP).

eIF4G stabilizes the eIF4E-mRNA interaction at the global scale

Our previous studies showed order-of magnitude variability in eIF4E affinity throughout the transcriptome driven mostly by the association rate. We next sought to address the role of other eIF4F complex members and initiation factors in defining cap recognition dynamics between transcripts. Due to the small sample size of mRNAs tested in our initial experiments (~0.1% of yeast mRNAs),

it was not possible to distinguish whether the observed effect of eIF4G on cap binding is specific to that set of mRNA, or if it takes place at the global level. Our assay is well suited for proposed models for eIF4F-based cap recognition and inferring rates of subsequent events and contributions of individual initiation factors, and their net effect across the transcriptome.

To determine if eIF4G can exert the same effect at the global level, we also repeated our transcriptome-wide experiment looking at eIF4E-mRNA dynamics, but this time including eIF4G together with eIF4E. In this case, the same batch of total mRNA was used, allowing for easy measurement of eIF4G-induced effects in a population-wide experiment and comparison with previous experiments using eIF4E alone (Figure 2.6.). We included eIF4G (250 nM) together with Cy5-labeled eIF4E (50 nM). Delivery of eIF4E to an mRNA population led to transient cycles of FRET, which is the same behavior observed with eIF4E alone. Due to the high affinity of eIF4G for eIF4E (K_d= 15 nM, Mitchell et al. 2010), under these conditions all the eIF4E protein is expected to be bound to eIF4G. Inclusion of full-length yeast eIF4G1 in the smFRET assay led to a reproducible acceleration of the median arrival rate across the mRNA population relative to the eIF4E-only condition previously reported (Figure 2.10B.).

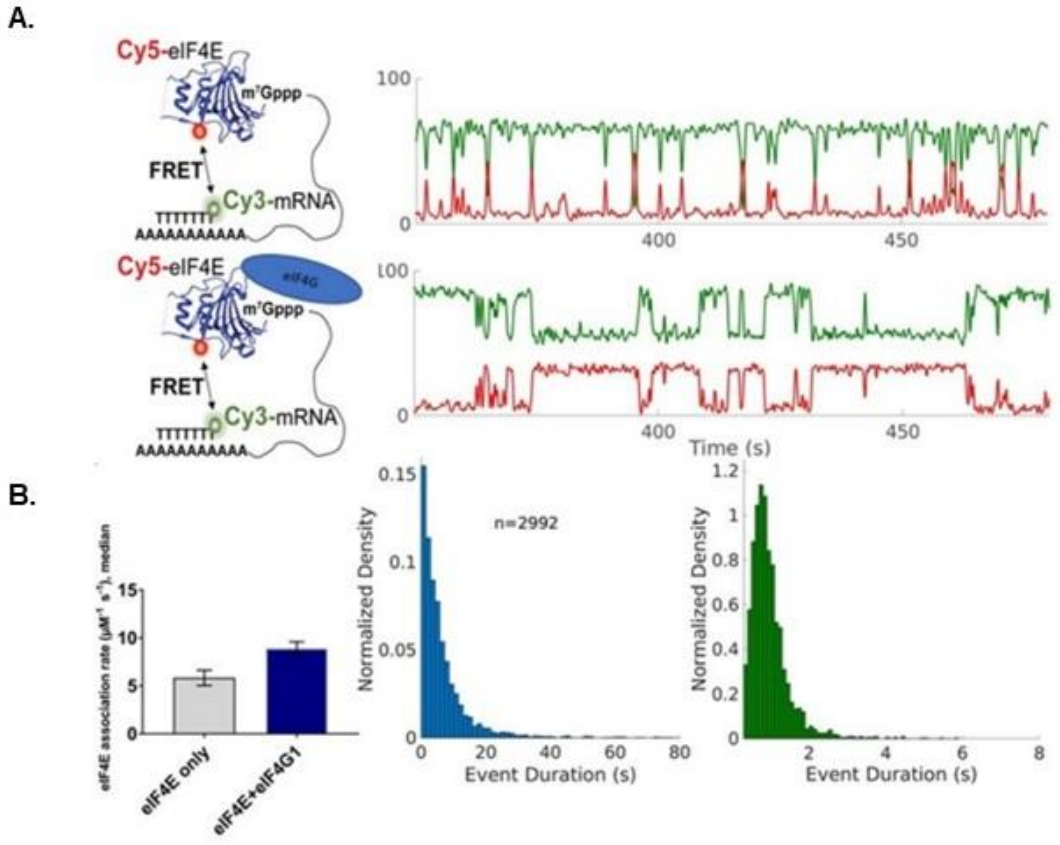

Figure 2.10. Dynamics of the eIF4E-eIF4G interaction transcriptome-wide. A. eIF4G is added into the transcriptome-wide experiment along with eIF4G. eIF4G accelerates the eIF4E-mRNA binding rate across the population, where there is a measurable increase in the median binding rate in a population of mRNAs when eIF4G is included. The stabilization of the interaction is apparent upon visual inspection of the traces- the bursts of FRET last longer with eIF4G included. The interaction between eIF4E and the mRNA cap is now closer to the initiation timescale, with events occasionally lasting for more than five seconds. A transient population persists upon the addition of eIF4G1, which is suggestive of an alternative conformation that is less efficient at engaging the mRNA. This could partially be due to eIF4G being an unstable protein in solution, however we have observed the same behavior even when isolating the two as a complex, suggesting that it is not due to having excess free eIF4E.

We had previously reported an order-of-magnitude heterogeneity in the arrival rate distribution when measuring eIF4E binding to a transcriptome-derived mRNA population, where there is a 20-fold difference between the 5th and 95th percentile of arrival rates (Çetin et al., 2020). eIF4G1 also narrowed the same arrival rate distribution relative to the eIF4E-only condition, where the fastest and the slowest binding mRNA binding rates are less different compared to the eIF4E-only condition. The 20-fold difference between the 5th and 95th percentile of the rates was reduced to ~4-fold (Figure 2.11.)

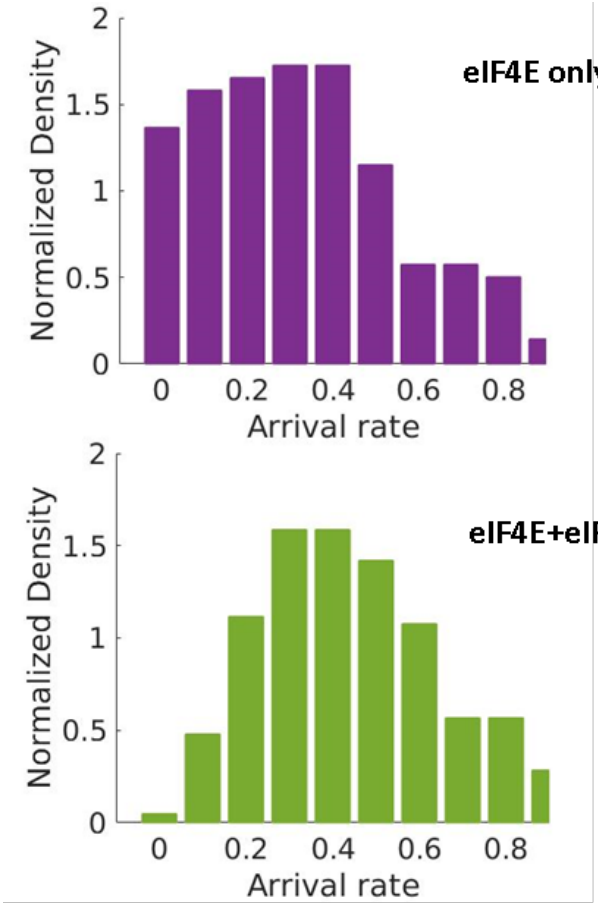

Figure 2.11. eIF4G reduces the heterogeneity in binding rates in an mRNA population. Top: Sample population-wide distribution of eIF4E-mRNA binding rates (per second) across an mRNA population when eIF4E alone is included in the experiment. Bottom: same distribution, but with both eIF4E and eIF4G included.

eIF4G1 exerts the main effect on eIF4E-cap affinity by significantly increasing the average cap-bound lifetime across the population, where the prolonged binding can be detected through the dwell time of FRET events (Figure 2.10A.). Fitting the lifetimes to a double exponential to obtain the dissociation rates revealed that eIF4G1 induces a longer-lived eIF4E-mRNA complex, the median lifetime of

which is around 4 seconds throughout the population (50th and 95th percentile of the lifetimes: ~4s and ~21 s), and does not exist in the eIF4E-only experiment described in a previous study (where the fit lifetimes were best fit to a single exponential, with the 50th and 95th percentile being ~1.15 and 2s, respectively). These results highlight the importance in increasing the lifetimes of the eIF4F-mRNA complex, as the binary eIF4E-mRNA cap interaction is highly dynamic. The quality of the fit for the lifetimes is also improved with eIF4G1 (relative to eIF4E alone), presumably because eIF4G increases the length of all events, allowing previously missed events to be detected (such as those that occur faster than the temporal resolution of the camera).

There are multiple mechanisms through which eIF4G can stabilize the interaction between eIF4E and the mRNA. eIF4G can bind eIF4E and trigger a conformational change (Gross et al., 2003) that would retain eIF4E on the cap for longer. The multiple RNA-binding domains of eIF4G (Berset et al. 2003) could also be responsible for stabilizing the interaction. Furthermore, the interaction could possibly be stabilized by a combination of both factors. To distinguish whether this is an effect of RNA-binding activity by eIF4G1 or a result of altering eIF4E conformation, we also performed the same experiment with eIF4G1 (348-513), which we had previously performed with short oligonucleotides (O'Leary et al., 2013). This truncation only includes the eIF4E-binding domain of eIF4G, lacking all RNA-binding domains. We conducted an analysis for n=100 molecules and found that eIF4G1 (348-513) does not induce the same long-lived population

(Figure 2.12.), although it does seem to stimulate the binding rate of eIF4E to the cap.

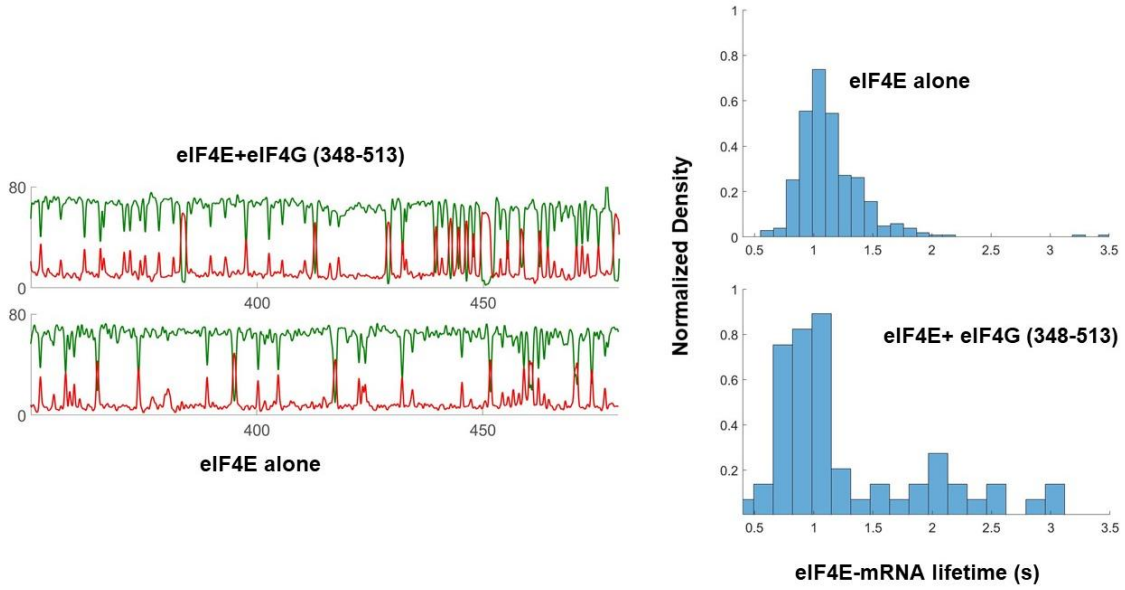

Figure 2.12. eIF4G (348-513) does not extend the eIF4E-mRNA lifetime. Sample smFRET trajectories are presented from an experiment with eIF4E alone (identical to that in Figure 1.6.), compared to an experiment with eIF4G (348-513). Upon visual inspection of the smFRET data it is apparent that the eIF4G fragment is unable to stabilize the eIF4E-mRNA interaction (relative to the full-length eIF4G). Analysis was conducted on a sample of the experiment with the short eIF4G peptide containing only the eIF4E-binding domain. The per-mRNA arithmetic mean lifetime distribution is also plotted, comparing the two experiments.

Our results highlight that eIF4G1 is required for stabilization of the eIF4E-cap interaction, enough to last on the initiation timescale, and that this is a global effect, because it was reproduced on both in vitro transcribed, model mRNAs (many copies of the same transcript) as well as pools of native mRNA. The observed heterogeneity in the lifetimes may be one of the driving factors behind

stochasticity of gene expression. Here, a fraction of the eIF4E-mRNA complexes become stable, rather than all. The broad range of eIF4F-mRNA complex lifetimes observed in these experiments could induce differences in the frequency of ribosome loading onto mRNAs. We also observed similar heterogeneous behavior in experiments conducted with copies of the same mRNA, suggesting it can be partially explained by conformational heterogeneity of the same type of mRNA molecule. We previously also observed different FRET states that interconvert for four different mRNAs, suggesting conformational heterogeneity in our mRNA samples (Chapter 1, Figure 1.13.).

In addition, eIF4G also alters the behavior of the association rates. We had previously reported that the eIF4E-mRNA association rates exhibit double-exponential behavior (Çetin et al., 2020). Addition of eIF4G1 increases the prevalence of the faster phase in the double-exponential, reducing the slow phase. This suggests that eIF4G can alter the conformation of the RNA to make it bind eIF4E faster, or it relieves a conformation of eIF4E that binds mRNA more slowly.

Dynamics of the eIF4F-mRNA interaction on individual mRNAs

We next assessed how formation of the full eIF4F complex modulated eIF4E–mRNA binding. We again included eIF4A (2 μM) and eIF4G (250 nM), reflecting their relative cellular concentrations and ensuring that eIF4E is near-quantitatively bound to both proteins in the eIF4F complex. eIF4E was included

at 10 – 30 nM, as eIF4G potentiates nonspecific eIF4E interactions with the ZMW surface. Based on past thermodynamic analysis, under these conditions eIF4E is expected to be quantitatively bound in an eIF4F complex.

In the eIF4F complex without ATP, eIF4E–mRNA association accelerated on all mRNAs relative to eIF4E alone (Figure 2.12C.), with rates between 43.3 ± 9.8 μM^{-1} s^{-1} for *JJJ1* and 102.2 ± 0.5 μM^{-1} s^{-1} for *HSP30*. This rate for *HSP30* was the fastest measured in the present study. Acceleration again varied between mRNAs, from 6.8 ± 1.9 to 3.0 ± 0.4-fold. The net effect was to differentiate eIF4E–mRNA binding between mRNAs relative to the eIF4E•eIF4G condition, though, as with eIF4E and eIF4E•eIF4G, the shorter mRNAs (*NCE102* and *HSP30*) retained faster association rates.

Since the individual effects of eIF4G and eIF4A•ATP on eIF4E–mRNA cap association served to narrow the range of eIF4E–mRNA association rates relative to the eIF4E-only condition, this differentiation of rates observed with all components of the eIF4F complex present is reasonably ascribed to intersubunit coordination that leads to a different mode of mRNA engagement by the eIF4F heterotrimer than is afforded by the sum of the individual subunit activities. Based on the available structural and biochemical data, and supported by the results described below, we propose that the conformational changes induced in the eIF4F subunits on formation of the eIF4F complex enhance the ability of eIF4F to discriminate between mRNAs in cap recognition, relative to eIF4E•eIF4G.

Long and short eIF4E–mRNA binding events were also observed with eIF4F, and their relative incidence was unchanged within experimental error (Figure 2.13D-E.). Transient eIF4E dissociation occurred at around ~0.3 s^{-1} – 0.6 s^{-1}, similar to eIF4E•eIF4G, while long events dissociated at between ~0.05 s^{-1} and 0.10 s^{-1}, slightly faster than for eIF4E•eIF4G. These results again place eIF4G as a dominant kinetic contributor to eIF4F–mRNA affinity, echoing thermodynamic data for human eIF4F.

However, addition of ATP led to both mRNA-specific and global changes in dynamics. The *HSP30* association rate was strikingly reduced, from being the fastest among the mRNAs, to being the slowest (32.8 ± 7.0 μM^{-1} s^{-1}) with ATP present. This almost entirely reversed the acceleration in eIF4E–mRNA binding afforded to *HSP30* by eIF4F (Figure 2.13F.).

On the other hand, the *NCE102*, *HXT2* and *JJJ1* mRNAs showed small or no reductions in association rate on ATP addition. Since the eIF4F-independent activity of eIF4A•ATP universally had the effect of accelerating eIF4E–mRNA association, our data imply that the kinetic changes in eIF4E–cap binding observed on addition of ATP to eIF4F are mediated through eIF4A bound in the eIF4F complex. As in the cases of eIF4E with added “free” eIF4A(ATP), and eIF4E•eIF4G, the fold-acceleration of eIF4E–mRNA binding with eIF4F in the presence of ATP, relative to eIF4E alone, retained a length dependence – i.e., eIF4F(ATP) overall accelerated eIF4E binding to a greater extent for longer

mRNAs (e.g., *JJJ1 vs. HSP30*). Moreover, the net association rate following this acceleration was again fastest on the 5'-unstructured *NCE102* mRNA.

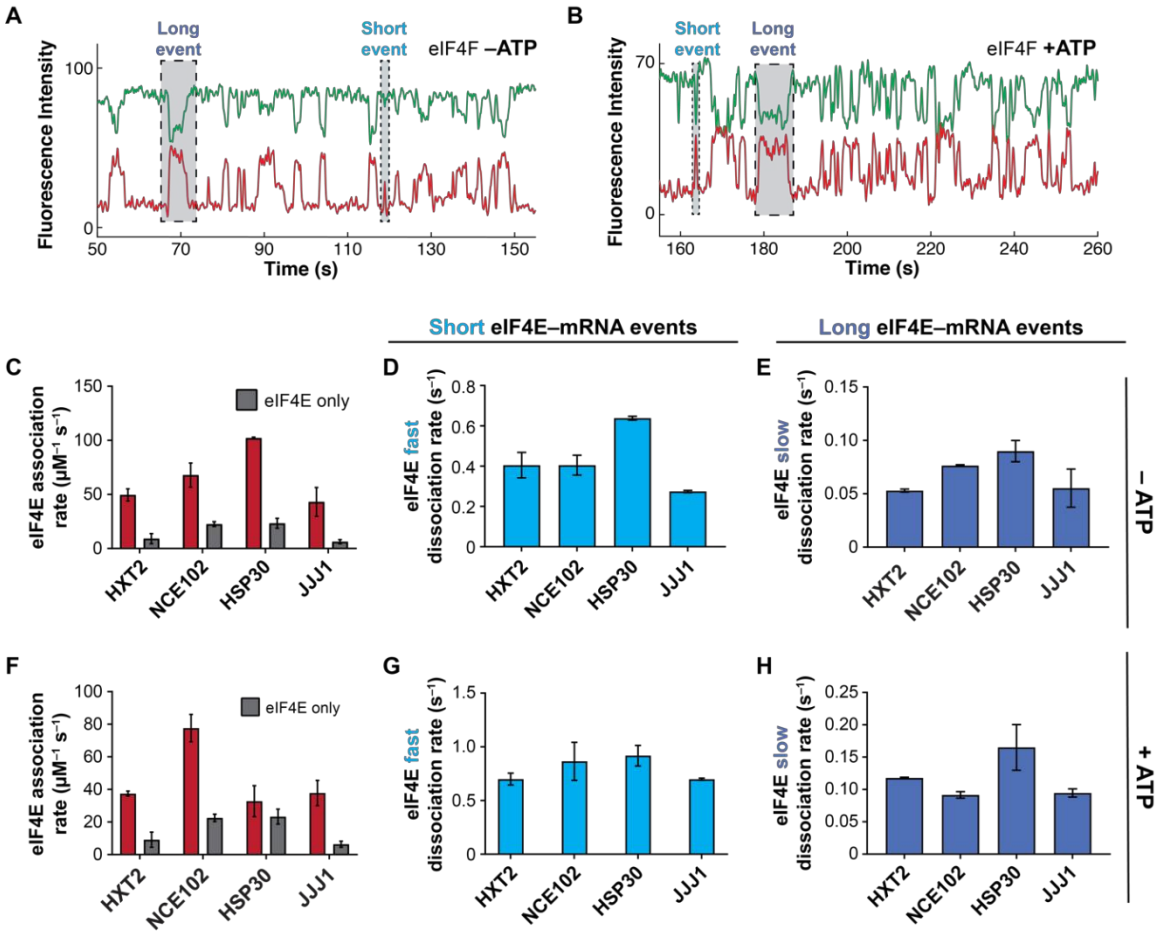

Figure 2.13. The eIF4F complex discriminates eIF4E–mRNA interaction dynamics in an ATP-dependent manner. A. Representative single-molecule fluorescence trace for eIF4E–mRNA interaction in the eIF4F complex without added ATP, on *NCE102* RNA. B Representative trace for eIF4E–mRNA binding in the eIF4F complex with ATP, on *NCE102*. C. eIF4E–mRNA association rates for the eIF4F complex without ATP (red), compared with the rates in the presence of eIF4E only (grey). D. Dissociation rates of transient eIF4E–mRNA interactions in the eIF4F complex without ATP. E. Dissociation rates of long-lived eIF4E–mRNA interactions in the eIF4F complex without ATP. F. eIF4E–mRNA association rates in the eIF4F complex with ATP (red), compared with the rates in the presence of eIF4E only. G. Dissociation rates of transient eIF4E–mRNA interactions in the eIF4F complex with ATP. H. Dissociation rates of long-lived eIF4E–mRNA interactions in the eIF4F complex with ATP.

ATP addition also shortened both the long and short eIF4E–mRNA binding events for the eIF4F complex, i.e. the complex became more dynamic (Figure 2.12G-H.). For the long events, this effect ranged from a modest ~50% for *HSP30* to around two-fold for *HXT2*. Dissociation kinetics also became even more similar between mRNAs than in the other conditions, pointing to a common rate-limiting step for eIF4E dissociation from the eIF4F•mRNA complex. However, the identity of that step still remained unclear.

Because eIF4E–mRNA dynamics became much more similar between mRNAs with eIF4F in the presence of ATP, no trends were discernible with respect to the *in vivo* RIP-seq enrichment data. However, since yeast eIF4A does not co-purify with eIF4E•eIF4G, direct comparisons may not be possible between the RIP-seq experiment and our experimental conditions where eIF4E•eIF4G is exposed to constant and high eIF4A concentrations. Nevertheless, and as for eIF4E•eIF4G alone, our data indicate that the main source of mRNA-to-mRNA variability in eIF4E–mRNA interaction for the eIF4F(ATP) complex is the association rate.

We were initially surprised at the extent to which eIF4F(ATP) tended to equalize eIF4E association rates between mRNAs, with the exception of the *NCE102* which had a higher association rate. *A priori*, this would run counter to the proposal that differential eIF4F interaction differentiates translation between mRNAs. However, inspection of publicly available published data revealed that the *JJJ1* , *HXT2*, and *HSP30* mRNAs have quite similar ribosome occupancies and densities *in vivo* as measured by ribosome density mapping (Arava et al. 2005), and *JJJ1* and *HXT2* have similar translation efficiencies as measured by ribosome profiling (the translation efficiency for *HSP30* was not included in this ribosome profiling dataset). Meanwhile, *NCE102* has significantly higher ribosome occupancies and densities, along with a higher translation efficiency than the other mRNAs. Thus, our data are consistent with a kinetic-control model for cap recognition *in vivo*, where differential eIF4F association rates limit translation differentially between mRNAs.

Simultaneous direct observation of eIF4A– and eIF4E–mRNA interaction

To broaden our view of eIF4F intersubunit coordination during cap recognition, we performed three-color experiments that included fluorescent Cy3-eIF4A (15 nM) (Figure 2.13A), co-delivered with Cy5-eIF4E (10 nM) and unlabelled eIF4G (250 nM) to surface-immobilized Cy3.5-mRNA. Cy3-eIF4A RNA-dependent ATPase activity was indistinguishable from the unlabeled protein (Figure

2.14B,C). The Cy3-eIF4A concentration was limited to 15 nM to prevent non-specific (i.e., RNA-independent) interactions with the surface at higher concentrations, which hinder data analysis. The concentrations of eIF4E and eIF4G were chosen for the reasons described previously. For these experiments we chose *JJJ1*, *NCE102*, and *HXT2*, which span the range of stimulation of eIF4E binding by eIF4A.

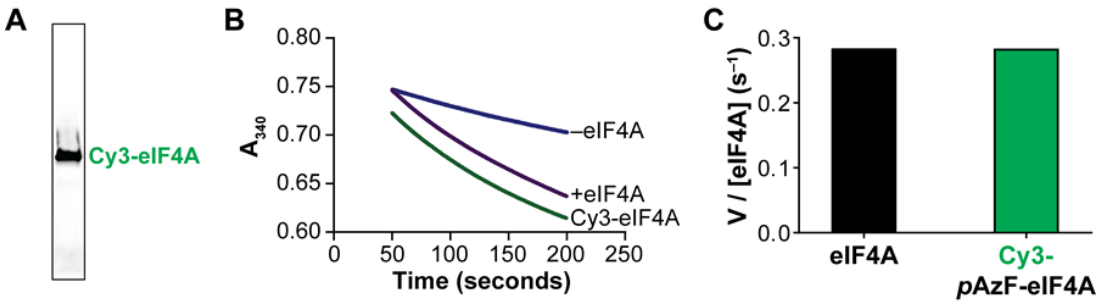

Figure 2.14. Preparation and validation of Cy3-eIF4A. A. SDS-PAGE analysis of Cy3-eIF4A, imaged for Cy3 fluorescence. B. Time-courses of ATP hydrolysis catalyzed by eIF4A and Cy3-eIF4A in the presence of poly(U) RNA and eIF4G1, monitored at 340 nm in an NADH-coupled assay, and compared with a no-enzyme control reaction. C. Quantitation of specific activity for eIF4A and Cy3-eIF4A from the time-course data in panel B.

We observed two types of eIF4A–mRNA binding event. In the first, eIF4A binding was accompanied by eIF4E–eIF4A FRET. (53%, 45%, and 43% of all eIF4A binding events for HXT2, JJJ1, and NCE102, respectively). Since no direct eIF4E–eIF4A interaction is known, we interpret these events to represent assembly of an intact eIF4F complex. In a second event type, eIF4A bound

mRNA without FRET to eIF4E (47%, 55%, and 57% for HXT2, JJJ1, and NCE102), (Figure 2.15B, traces showing behavior in Figure 2.16C-D).

This second class of events results from two separate processes: binding of an authentic eIF4F complex in which the eIF4E is non-fluorescent, and eIF4A–mRNA binding outside of eIF4F, i.e. “free” eIF4A–mRNA interaction (approximately 10% of eIF4A is expected to be free – i.e., not bound to eIF4E•eIF4G – under our conditions). Two types of this no-FRET eIF4A–mRNA binding mode were observed – transient and longer-lived, with the transient events constituting 25 – 90% of the eIF4A–mRNA encounters, depending on mRNA (Figure 2.14F).

The eIF4A–mRNA dissociation rates in eIF4A–eIF4E co-binding events (i.e., authentic eIF4F–mRNA complex formation) were kinetically similar between mRNAs and ranged from 0.027 ± 0.007 s^{-1} (JJJ1) to 0.041 ± 0.003 s^{-1} (HXT2), (Figure 2.15E) Conversely, the dynamics of eIF4A–RNA binding events lacking eIF4E–eIF4A FRET varied between mRNAs and also differed kinetically from events where eIF4E–eIF4A FRET was observed, consistent with a portion of them reporting on eIF4A–mRNA interactions outside the eIF4F complex. The dissociation rates for the dominant (higher-amplitude) eIF4A dissociation pathway in these no-FRET events also varied considerably between the mRNAs, from 0.095 ± 0.03 s^{-1} (NCE102) to 0.325 ± 0.003 s^{-1} (HXT2).

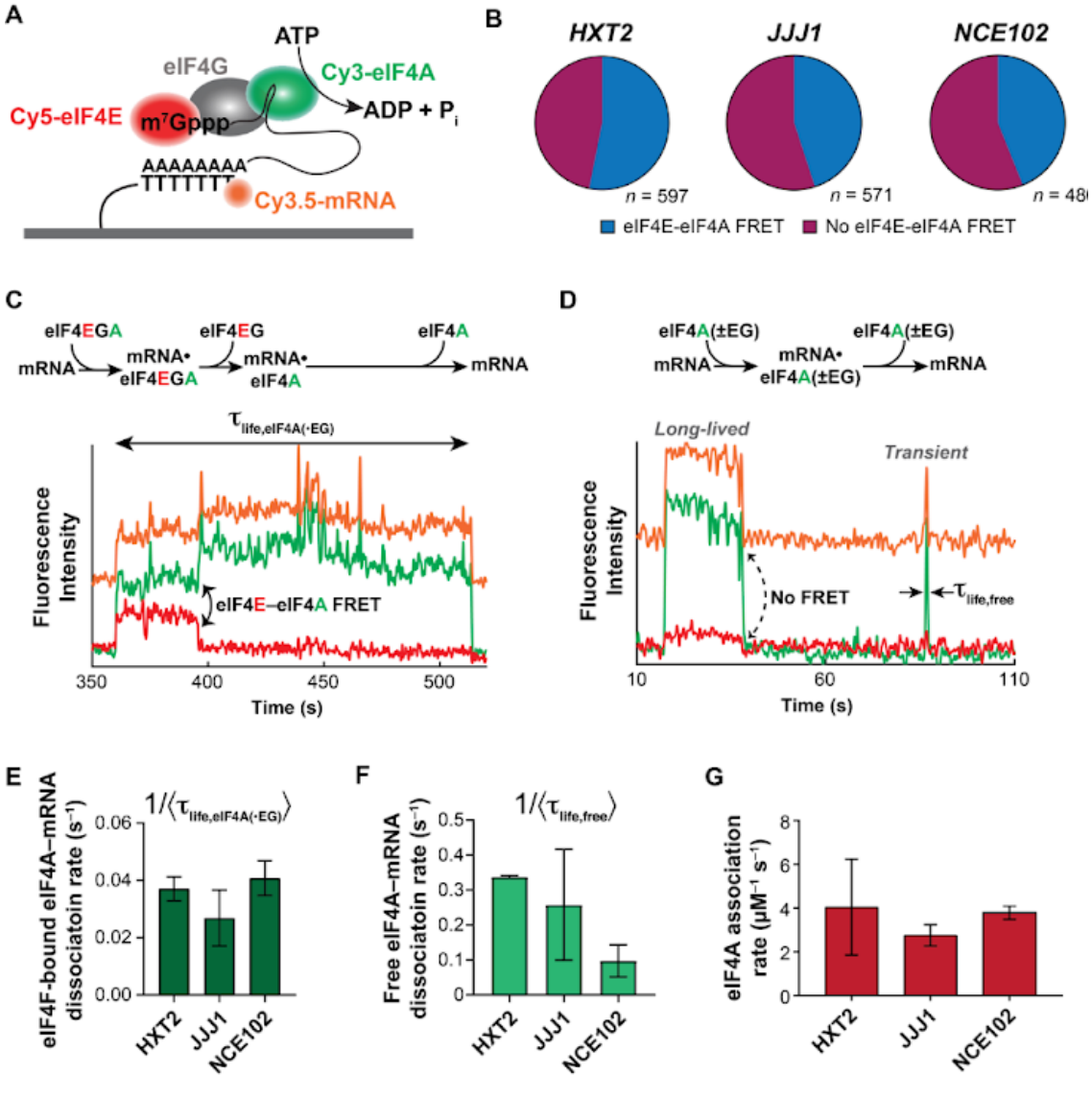
A
ATP
eIF4G
Cy3-eIF4A
Cy5-eIF4E
m7Gppp
ADP + Pi
AAAAAAAA
Cy3.5-mRNA
B
HXT2
JJJ1
NCE102
n = 597
n = 571
n = 48
eIF4E-eIF4A FRET
No eIF4E-eIF4A FRET
C
eIF4EGA
mRNA
mRNA•
eIF4EGA
eIF4EG
mRNA•
eIF4A
eIF4A
mRNA
τlife,eIF4A(·EG)
Fluorescence Intensity
eIF4E–eIF4A FRET
350
400
450
500
Time (s)
D
eIF4A(±EG)
mRNA
mRNA•
eIF4A(±EG)
eIF4A(±EG)
mRNA
Long-lived
Transient
Fluorescence Intensity
No FRET
τlife,free
10
60
110
Time (s)
E
eIF4F-bound eIF4A–mRNA dissociatoin rate (s−1)
1/⟨τlife,eIF4A(·EG)⟩
0.06
0.04
0.02
0.00
HXT2
JJJ1
NCE102
F
Free eIF4A–mRNA dissociatoin rate (s−1)
1/⟨τlife,free⟩
0.5
0.4
0.3
0.2
0.1
0
HXT2
JJJ1
NCE102
G
eIF4A association rate (μM−1 s−1)
8
6
4
2
0
HXT2
JJJ1
NCE102

Figure 2.15. Three-color smFRET to probe eIF4F- and eIF4A-mRNA interaction dynamics. A. Schematic of the three-color smFRET experiment with two donors (on eIF4A and mRNA) and one acceptor (eIF4E). A FRET signal between Cy5-labeled eIF4E and the Cy3.5-labeled mRNA is tracked at the same time as a FRET signal between Cy3-eIF4A and Cy5-eIF4E. B. Relative incidence of eIF4A-mRNA binding occurring with and without FRET to eIF4E. n is the number of molecules analyzed to enumerate the event types on each mRNA. C. Reaction pathway and representative smFRET trace showing concomitant mRNA binding of eIF4E and eIF4A with eIF4E–eIF4A FRET, consistent with eIF4F–mRNA binding, on JJJ1. The eIF4A–mRNA lifetime measured in panel E is indicated. D. Reaction pathway and representative single-molecule fluorescence trace for eIF4A–mRNA binding without eIF4E–eIF4A FRET on JJJ1. These events result both from "free" eIF4A–mRNA interaction ("eIF4A(–EG)"), and eIF4F–mRNA interaction where eIF4E is unlabeled ("eIF4A(+EG)". The Cy3 and Cy5 signals were manually corrected by linear subtraction to equalize their background values, for clarity of presentation. E. eIF4A–mRNA dissociation rates following eIF4A–mRNA binding with eIF4E, i.e., with observable eIF4E–eIF4A FRET as shown in panel C. The Cy3 and Cy5 signals were manually corrected by linear subtraction to equalize their background values, for clarity of presentation. F. eIF4A–mRNA dissociation rates following eIF4A–mRNA binding without FRET to eIF4E. G. eIF4A–mRNA association rates across all binding event types.

eIF4A–mRNA association rates were identical between mRNAs within experimental error (Figure 2.15G). Interestingly, then, and in contrast to eIF4E, variable affinity of free eIF4A for different mRNAs appears to result from differences in the lifetimes of the eIF4A•mRNA complexes. This echoes results that demonstrate different conformational dynamics of eIF4A in the presence of RNA oligonucleotides that differ in their duplex properties, as well as unwinding by eIF4F. Extrapolating our data to cellular concentrations of eIF4A, these results further implicate free eIF4A as a multifunctional "mRNA chaperone" that maintains cap accessibility for eIF4F binding.

ATP hydrolysis ejects eIF4E from the cap after initial eIF4F–mRNA binding

Initial eIF4F•mRNA complex formation sets the stage for recruitment to the mRNA of the 43S ribosomal pre-initiation complex. A key question around cap recognition is how the mRNA 5' end is transferred into its channel on the 40S subunit if the cap is bound by eIF4E/eIF4F. However, the sequence of events occurring in the eIF4F•mRNA complex immediately after its formation remains incompletely understood.

In our two-color smFRET experiments with eIF4F, we found that addition of ATP increased the rate of eIF4E–mRNA dissociation. Our three-color experiments now allowed us to directly follow the fates of eIF4E and eIF4A once bound to mRNA. In these three-color experiments, we also found that eIF4E fluorescence frequently disappeared before eIF4A fluorescence after formation of an eIF4F•mRNA complex detected by co-arrival of Cy5-eIF4E and Cy3-eIF4A fluorescence displaying Cy3-Cy5 FRET (Figure 2.10). Within these eIF4F–mRNA events, eIF4E dissociation prior to eIF4A was the most common outcome, and occurred for ~66% of eIF4F–mRNA binding events on NCE102, 51% on *JJJ1*, and 61% on *HXT2*. Simultaneous disappearance of eIF4E and eIF4A fluorescence thus occurred in 34%, 49%, and 39% of eIF4F–mRNA binding events on NCE102, JJJ1, and HXT2, respectively. We observed hardly any occurrences of eIF4A departing the mRNA before eIF4E. Thus, there is a

preference for disrupting eIF4E–cap interaction whilst maintaining eIF4A–mRNA binding. This echoes findings for mammalian eIF4F where cap binding appears to reduce eIF4E affinity for eIF4F (Ray et al. 1985).

Disappearance of eIF4E fluorescence could be due either to its complete dissociation from eIF4F•mRNA, or adoption of an extended eIF4F conformation that places eIF4E out of FRET range to both mRNA and eIF4A. To differentiate between these possibilities, we repeated the experiment with direct excitation of the Cy5-eIF4E fluorophore. In this illumination scheme, all eIF4E–mRNA interactions are detected, rather than only interactions that produce FRET – i.e., adoption of a no-FRET conformation would be reported by loss of FRET but persistence of the Cy5 signal. We found that disappearance of eIF4E–mRNA FRET following eIF4F–mRNA binding was due to complete dissociation of Cy5-eIF4E from mRNA for 90% of the FRET events on the JJJ1 mRNA. Put otherwise, eIF4E is ejected from the eIF4F•mRNA complex shortly after cap recognition (Figure 2.16.).

We also observed relatively frequent eIF4E rebinding after initial ejection. However, while the first eIF4E dissociation event occurred at a rate of 0.07 – 0.09 s^{-1} across all mRNAs, dissociation during the subsequent rebinding events was slightly faster (k_{off} ~0.11 s^{-1} – 0.14 s^{-1}, Figure 2.17D,E). Evidently a change occurs in the eIF4F complex once it has established itself at the mRNA 5' end which enhances eIF4E dissociation. Indeed, a regular feature of the

eIF4F•mRNA complex was fluctuation of the FRET efficiency during the binding events. This suggests the occurrence of conformational rearrangements once the complex once it is formed on mRNA. This raised the question of whether eIF4E was dissociating alone, or along with eIF4G. To directly address this question, we non-specifically labelled full-length eIF4G with Cy5.5, allowing eIF4E and eIF4G to be visualized simultaneously as they interact with mRNA.

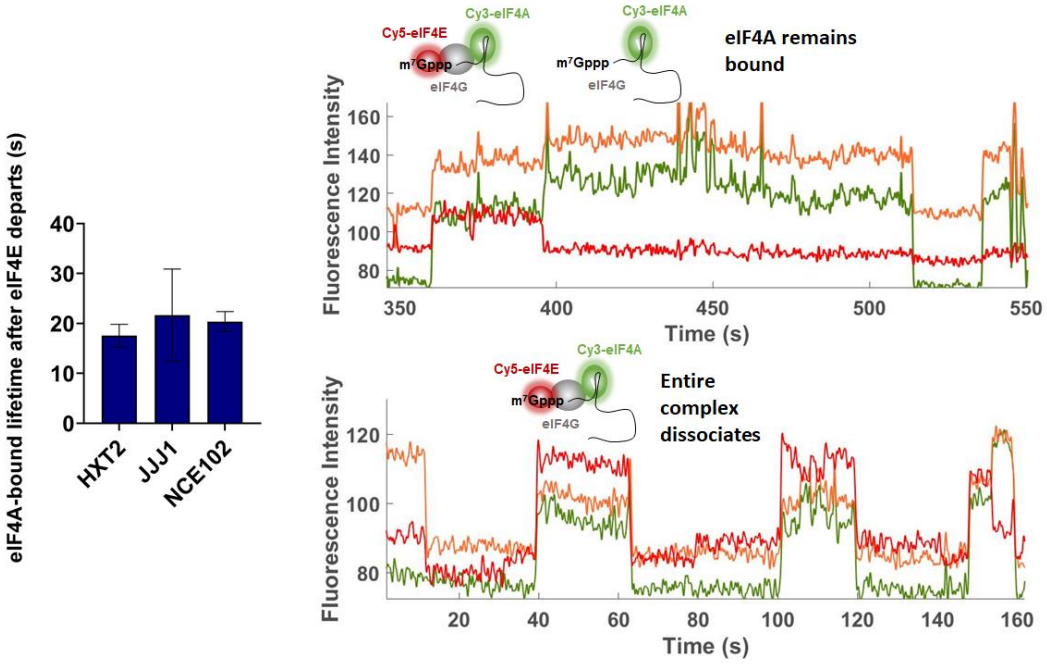

Figure 2.16. Differential eIF4F behavior once bound to mRNA revealed by three-color single molecule spectroscopy. The experimental setup allows distinguishing between events where the eIF4E and eIF4A dissociate from the mRNA as a unit. Examples of both are present in different fluorescence time trajectories, the upper trajectory (same as the one in Figure 2.5) indicates a case where the eIF4A remains bound to mRNA after eIF4E dissociates. The dwell time of eIF4A remaining bound is also quantified and plotted, in this case it is between ~15-20s.

We then co-delivered labelled eIF4E, eIF4G, and eIF4A to surface-immobilized mRNA. The most common behavior observed after co-arrival of eIF4E, eIF4G, and eIF4A (i.e., eIF4F•mRNA complex formation) was that the Cy5-eIF4E and Cy5.5-eIF4G fluorescence departed the mRNA simultaneously, which was observed in different trajectories (Figure 2.15F). Thus, our data support a model where the most likely possibility is eIF4E•eIF4G is ejected from the cap as a unit shortly after eIF4F•mRNA complex formation, leaving eIF4A bound to mRNA. This model is also consistent with the finding that RIP-seq enrichments for eIF4E and eIF4G1 are highly similar in yeast (Costello et al., 2015); if eIF4E was frequently ejected on its own, RIP-seq enrichments would be expected to be higher for eIF4G than for eIF4E.

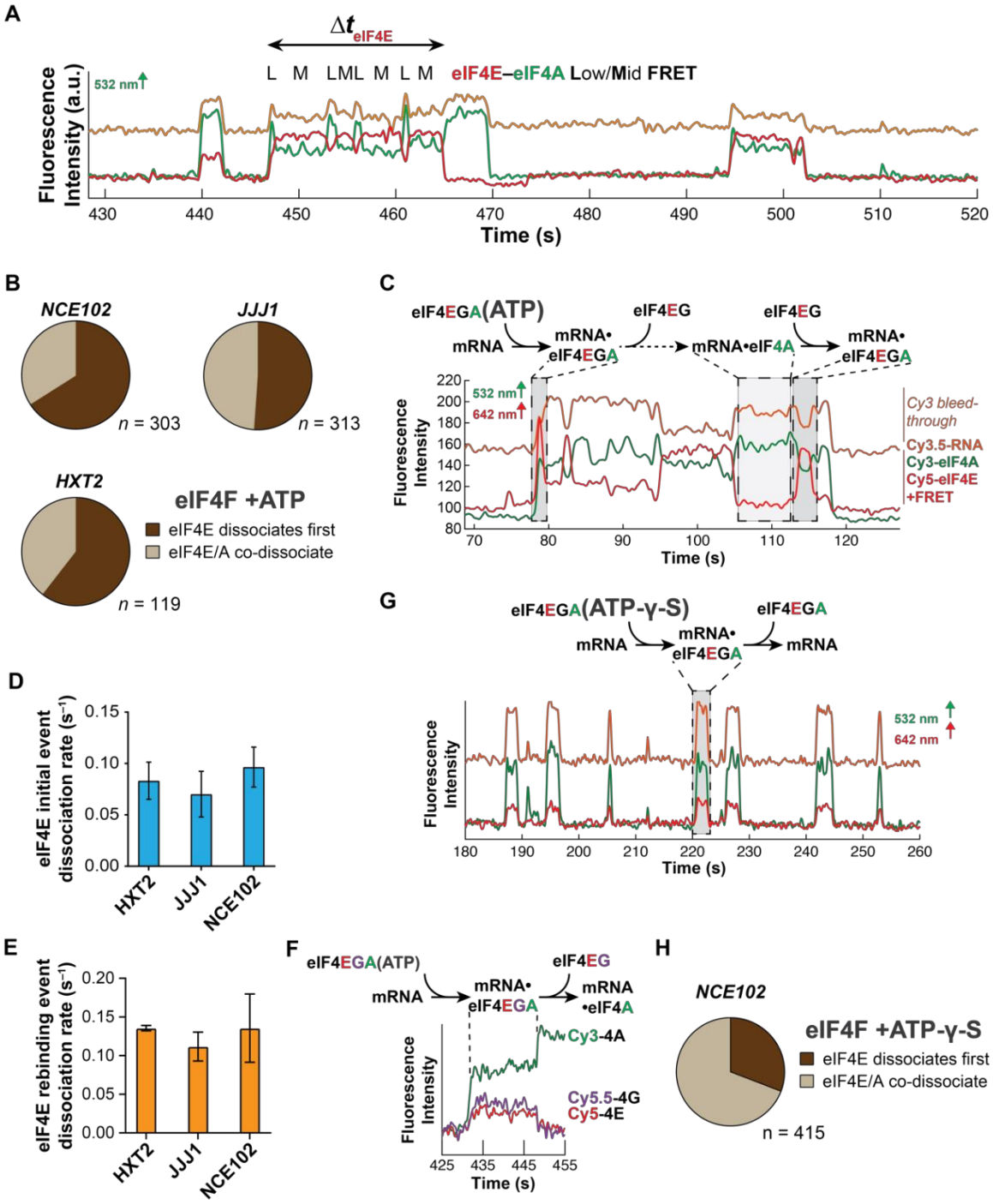
A
Δt eIF4E
L M LML M L M eIF4E–eIF4A Low/Mid FRET
532 nm
Fluorescence Intensity (a.u.)
Time (s)
B
NCE102
JJJ1
HXT2
n = 303
n = 313
n = 119
eIF4F +ATP
eIF4E dissociates first
eIF4E/A co-dissociate
C
eIF4EGA(ATP)
eIF4EG
mRNA
mRNA• eIF4EGA
mRNA•eIF4A
532 nm
642 nm
Cy3 bleed-through
Cy3.5-RNA
Cy3-eIF4A
Cy5-eIF4E
+FRET
Fluorescence Intensity
Time (s)
D
eIF4E initial event dissociation rate (s⁻¹)
HXT2
JJJ1
NCE102
E
eIF4E rebinding event dissociation rate (s⁻¹)
HXT2
JJJ1
NCE102
F
eIF4EGA(ATP)
eIF4EG
mRNA
mRNA• eIF4EGA
mRNA •eIF4A
Cy3-4A
Cy5.5-4G
Cy5-4E
Fluorescence Intensity
Time (s)
G
eIF4EGA(ATP-γ-S)
eIF4EGA
mRNA
mRNA• eIF4EGA
mRNA
532 nm
642 nm
Fluorescence Intensity
Time (s)
H
NCE102
eIF4F +ATP-γ-S
eIF4E dissociates first
eIF4E/A co-dissociate
n = 415

Figure 2.17. Dynamic coordination within eIF4F after cap recognition. A. Representative smFRET trajectory showing event with ejection of eIF4E prior to eIF4A, and fluctuations in the eIF4F•mRNA conformation on JJJ1 . B. Relative incidence of initial eIF4E dissociation vs. eIF4E/eIF4A co-dissociation from eIF4F•mRNA complexes. n is the number of molecules analyzed to enumerate the event types on each mRNA. C. Reaction pathway and annotated representative single-molecule fluorescence trajectory for eIF4F•mRNA complex formation and dynamics, observed by dual red/green illumination which directly reports on the presence of both Cy3-eIF4A and Cy5-eIF4E. D. Rates for the initial eIF4E–mRNA dissociation event after eIF4F–mRNA complex formation. E. eIF4E–mRNA dissociation rates for events where eIF4E rebinds mRNA following initial dissociation from eIF4F•mRNA. F. Reaction pathway and representative single-molecule fluorescence trajectory for a four-color experiment where eIF4G is non-specifically labeled with Cy5.5, allowing its simultaneous detection with Cy3-eIF4A and Cy5-eIF4E. eIF4E and eIF4G fluorescence co-depart the mRNA. G. Reaction pathway and annotated representative single-molecule fluorescence trajectory for eIF4F•mRNA complex dynamics with ATP-γ-S. The Cy3 and Cy5 signals were manually corrected by linear subtraction to equalize their background values, for clarity of presentation. H. Relative incidence of eIF4E or eIF4A dissociation, or co-dissociation from the eIF4F•mRNA complex in the presence of ATP-γ-S.

To establish the role of ATP hydrolysis in ejection of eIF4E from the eIF4F•mRNA complex, we substituted ATP with ATP-γ-S and monitored the dynamics of the corresponding eIF4F•mRNA complexes. With the slowly-hydrolyzable analog, the relative incidence of eIF4E–eIF4A co-dissociation from RNA increased at the expense of eIF4E ejection (Figure 2.17G,H). Thus, ejection of eIF4E is attributable to ATP hydrolysis in the eIF4F complex.

eIF4F increases eIF4E affinity to the cap across the transcriptome, dependent on ATP concentration

We also looked at how eIF4F in the presence of variable amounts of ATP (binding of which to eIF4A can modulate activity) can modulate eIF4E-mRNA binding. We first included the eIF4F complex without ATP, where the on and off-rates look similar to the eIF4E-G condition, although the lifetimes were slightly shorter. We then added varying concentrations of ATP into the experiment. Inclusion of ATP (0.5-2.5 mM) recovers the median lifetime of the long-lived population back to the eIF4E-eIF4G1 only condition (Figure 2.18) and further increases it at higher concentrations of ATP. Inclusion of the whole eIF4F complex and ATP accelerated further increased the binding rate, and higher concentrations of ATP (>0.5 mM) are required to achieve this (Figure 2.19.). At lower ATP concentrations, the binding and dissociation rates look identical to that of the eIF4E+eIF4G1 experiment. The lifetimes remained similar as the eIF4E+eIF4G1 condition, with only a modest increase, which indicates that eIF4G1 is mainly responsible for driving the length of the eIF4F-mRNA interaction.

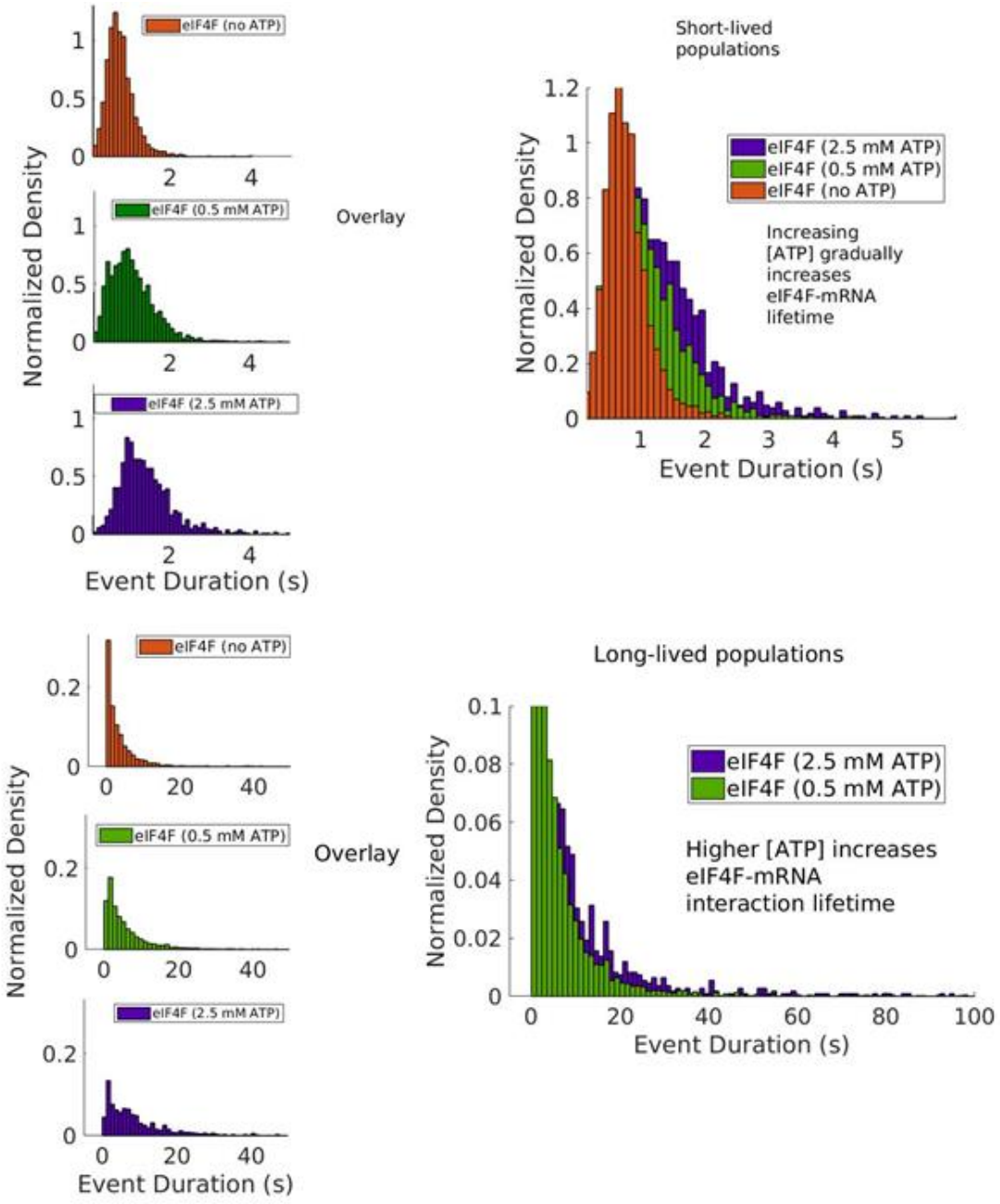

Figure 2.18. [ATP] modulates eIF4F-mRNA lifetime at the transcriptome-wide level. Inclusion of varying amounts of [ATP] in the smFRET experiments gradually increases the eIF4E-mRNA bound lifetime, both for the transient and long-lived events. The binding rate is increased gradually with more ATP added.

These results suggest that formation of the eIF4F complex, with ATP, contributes to the observed discrimination between mRNAs by altering the rate-of formation differently on different mRNA transcripts. The observed variability in binding rates increases with increasing [ATP], suggesting that ATP concentration affects eIF4F dynamics to promote selectivity for binding (Figure 2.18). We found that higher (above 2.5 mM) amounts of ATP further stimulate the binding rate, which is not observed with lower concentrations of ATP (0.5 mM). At lower ATP concentrations (0.5 mM), we obtained essentially the same result as the eIF4E+eIF4G1 condition. However, when a larger (2.5 mM) amount of ATP is added, the binding rate of eIF4E to the cap is stimulated further compared to all other experiments that contain eIF4E+eIF4G1, eIF4F without ATP, eIF4F with AMPPNP (Figure 2.19.). The lifetime distribution of both the long-lived and short-lived population is also shifted to the right (e.g., the duration of the observed eIF4F-mRNA interaction is increased). This effect is not observed when AMPPNP (a nonhydrolyzable ATP analog) is included in the experiment, suggesting that ATP hydrolysis may be involved in the observed effect rather than mere binding. In addition, we previously found that inclusion of free eIF4A and 2.5 mM ATP in this experiment does not cause an increase in the lifetime, although it does stimulate the binding rate relative to only including eIF4E.

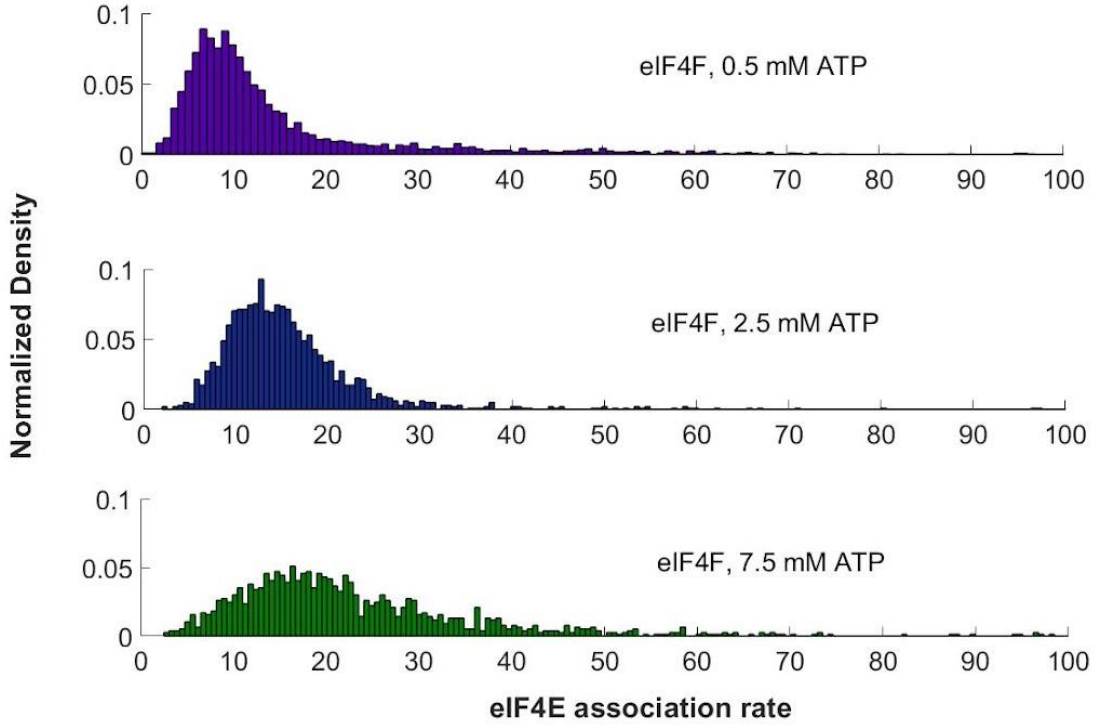

Figure 2.19. Distribution of eIF4E-mRNA binding and dissociation rates across the transcriptome with varying concentrations of ATP. Per-mRNA binding rate distributions are presented in three different experiments where ATP concentration was varied. Increasing [ATP] increases the median binding rate across the population, along with causing the distribution to get broader (e.g, causing more variability between transcripts). Furthermore, adding more [ATP] gradually increases the eIF4E-mRNA lifetime. Data includes both the short-lived and long-lived populations of eIF4E-mRNA binding, which are separated via double exponential fitting of the dwell times, as described above.

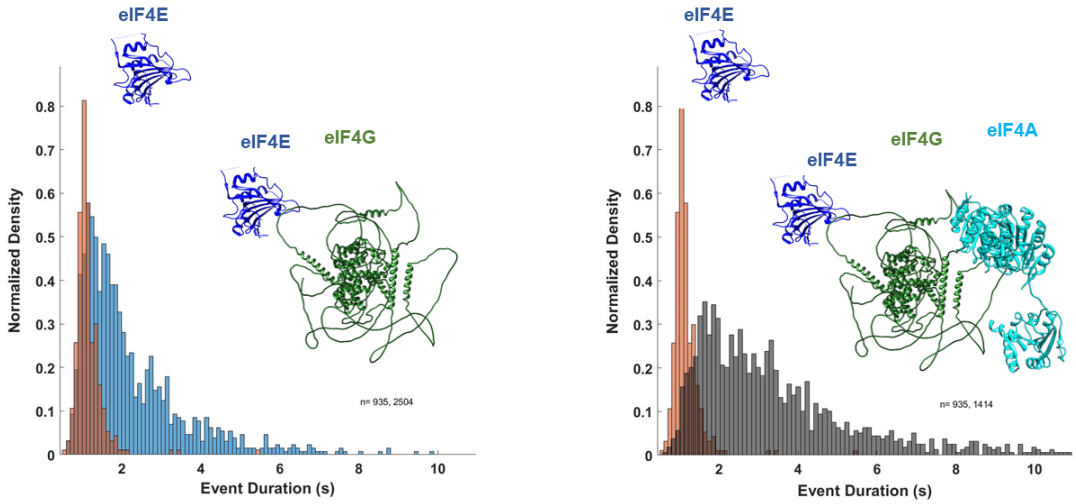

Figure 2.20. Comparison of the eIF4E-G mRNA binding lifetimes to eIF4F with 2.5 mM ATP included. The plot on the left shows the mean eIF4E-only lifetime per mRNA (orange) overlaid with the eIF4E-G condition. The plot on the right shows the same eIF4E-only condition, but this time overlaid with the eIF4F+ 2.5 mM ATP condition, where the lifetimes are increased. The mean lifetime distribution includes a "tail" with eIF4G1 added.

Discussion

Our results place eIF4G at the central role for defining the efficiency of cap binding. The ability of RNA-binding proteins to increase eIF4E-mRNA binding (such as when eIF4A is present without eIF4G) suggests that RNA-binding proteins can act as a chaperone in some cases to make eIF4E binding at the cap more efficient. The excess eIF4A (present at higher concentrations than eIF4E and eIF4G in cells) possibly acts as a chaperone on a cluster of mRNAs to make them more efficient in translation, and to prevent condensation, which would limit the formation of stress granules (Tauber et al. 2020). Our results show that eIF4E– and eIF4F–mRNA dynamics are sensitive to coding-sequence and

mRNA length, and that RNA-binding activity of individual initiation factors partially mitigates this sensitivity.

Similar to eIF4A and eIF4G, other RNA binding proteins may also act to reduce this length dependence. Because both eIF4G and eIF4A, which bind RNA through different structural mechanisms, can both accelerate eIF4E–mRNA binding, our data point tertiary structure being more likely to form in longer mRNAs that pose a steric hindrance to eIF4E–cap binding as the source of the apparent length dependence in our experiments. Regardless, the variable association rates demonstrated in our biophysical experiments would confer an advantage to certain mRNAs during translation. An mRNA that binds eIF4E faster would retain high translation initiation even during cellular conditions where the active eIF4E concentration is reduced (e.g., when 4E-binding proteins are actively binding and sequestering eIF4E away from eIF4G). In addition, since certain mRNA decay mechanisms such as decapping require dissociation of eIF4E (Schwartz and Parker, 2000), mRNAs with lower eIF4E dissociation rates or higher association rates are likely to be more stable.

Furthermore, previous studies indicated that shorter mRNAs are more likely to associate with eIF4F complex members (as well as PABP) (Thompson and

Gilbert 2017). Our data indicate that this may be partially due to the inherent property of shorter transcripts to bind eIF4F components faster.

Moreover, our data indicate that mRNAs utilize eIF4G to arrive at their maximum potential affinity for eIF4E. Such as, eIF4G was enough to achieve the maximum or near-maximum binding rate relative to other conditions up to the inclusion of the eIF4F complex with ATP for most of the mRNAs tested. Variable eIF4F binding rates can explain variable translational efficiency, through kinetically controlling the efficiency of translation initiation on a given transcript through the formation rate of an eIF4E-mRNA complex. This is also significant because it could allow for fine tuning the rate of eIF4E-mRNA complex formation for different mRNAs when levels of individual initiation factors are altered, which is an additional point of regulation to the multi-component process of translation initiation. Furthermore, eIF4G reduces the apparent variability in eIF4E-mRNA association rates relative to eIF4E alone but leads to more heterogeneity in the dissociation (by causing a fraction of complexes to be stable). Moreover, the lifetime of the eIF4E-mRNA complex was largely similar among the mRNAs tested when eIF4F was present together with ATP, which is likely the in vivo situation. This was only tested on four mRNAs, the lifetime of the complex may be variable throughout the transcriptome and would add an additional layer of control by determining how long an mRNA remains activated for initiation (e.g., the time window where the mRNA is available for ribosome recruitment). However, we have not tested different ATP concentrations extensively with

individual mRNAs and cannot exclude that the complex would behave differently at different levels of ATP, which is bound and hydrolyzed by eIF4A. Indeed, our transcriptome-wide experiments indicate that the concentration of ATP plays a role in the dynamics.

Cellular mRNAs begin de-novo translation in an environment replete with RNA-binding proteins and are subsequently incorporated into polysomes. While our experiments do not contain the cellular complement of RNA-binding proteins, the two-color experiments containing eIF4A include it at concentrations that fully saturate its double-stranded RNA binding and significantly saturate single-stranded RNA binding. Thus, the mRNAs in these experiments are expected to exist in an eIF4A mRNP. Our data then suggest that mRNP formation accelerates eIF4F–cap association in a length-dependent manner, and that the acceleration is physiologically relevant.

While our study does not probe eIF4F–mRNA dynamics in polysomes, polysome formation is expected to disrupt both secondary and tertiary structures in mRNA. This is consistent with the finding that very long mRNAs engaged in translation show end-to-end separation that greatly reduces when ribosomes are released by puromycin treatment (Khong & Parker, 2018). Since our data suggest that disruption of mRNA structure leads to enhanced cap recognition, our model predicts that cap recognition may become more efficient as polysomes form and begin to grow in size. Interestingly this could also, in principle, permit a

cooperative effect on cap-/eIF4F-dependent pre-initiation complex loading rates during the earlier rounds of translation. As higher-order polysomes form, eIF4F-dependence of initiation may become less prominent, due both to efficient re-initiation of terminating ribosomes and also enhanced mRNA compaction observed in very heavy polysomes. Our data do not exclude a role for poly(A)-binding protein in modulating how eIF4E binds the mRNA cap structure. PABP–eIF4G interactions could change the conformation of eIF4F to increase the likelihood of efficient binding of eIF4E to the mRNA cap. This would be consistent with the ability of poly(A)-binding protein to stimulate translation on non-polyadenylated mRNAs when provided poly(A) in previous experiments (Borman et al. 2002). Several classes of mRNAs have been identified with differing relative enrichments in eIF4E•eIF4G and Pab1p, pointing to the potential for differential interaction dynamics between these factors on different mRNAs (Costello et al., 2015). PABP also stimulates translation of different mRNAs to a different extent (Sonenberg et al. 1980). It is thus safe to assume that PABP would affect the eIF4E-mRNA dynamics in an mRNA-dependent manner.

After accommodation of eIF4F onto the mRNA, eIF4G–mRNA interactions maintain the eIF4E–cap interaction on the initiation timescale. However, not all complexes that form between eIF4E-G and mRNA were stable, regardless of different strategies to ensure that all eIF4E is bound to eIF4G (e.g., isolating the two proteins as a complex, or titration of eIF4G into the experiment). This suggests an alternative conformation of the eIF4E-G complex where not all RNA-

binding domains are contacting the mRNA, hence unable to prolong the lifetime as much, or different conformations of the mRNA causing variable complex lifetime.

The complex appears to be conformationally dynamic from inspection of the FRET signal. eIF4A ATP hydrolysis then promotes eIF4E dissociation from the mRNA, most reasonably ascribed to allosteric communication mediated by eIF4G. Our data suggest that ATP hydrolysis and eIF4E dissociation are accompanied by a conformational change in the eIF4A•mRNA complex, since eIF4E that rebinds shortly after initial ejection has a shorter residence time than in the original eIF4F•mRNA encounter. eIF4F subunit thus plays a role in establishing the net efficiency of cap recognition. mRNA identity – asserted through a combination of length and structural features – contributes more to variability in cap recognition toward the beginning of this sequence of events, while the factor activities dominate the later stages. Such an arrangement is optimal for maximizing mRNA-to-mRNA discrimination through kinetic control of the recognition process. Our data further indicate that eIF4A can also act scaffold protein that assembles eIF4F by remaining bound to the mRNA and allowing rebinding of other eIF4F factors, along with eIF4G.

ATP concentration in cells is affected by different perturbations such as stress (Gribble et al. 2000, Mendelsohn et al. 2018). Our results suggests that availability of ATP plays an important role for eIF4F discrimination of mRNAs. This may be a mechanism for retaining specific mRNAs in stress granules or

preventing specific mRNAs from being translated when ATP is less abundant. Under this model, mRNAs whose translation is activated upon stress would inherently bind eIF4F faster and be able to retain their ability to efficiently form a complex with eIF4F when less ATP is available.

Chapter 3. Development of an automated analysis scheme for smFRET data generated by the RS II instrument

Introduction

In this chapter, I will discuss a method for partially automating the data analysis for our imaging system. The custom MATLAB scripts developed previously in the Puglisi lab at Stanford University (Chen et al., 2014) work well for analysis of data generated by the RS instrument, where the user inspects time traces generated from each experiment, selects traces appropriate for data analysis, and then manually assign bound vs. unbound states, or dwell times. These have been described previously (Tsai 2013, Chen 2015). However, this process can be time consuming, and not ideal when many binding events are observed in each trace (such is the case in our system when observing eIF4E binding to mRNA, where many cycles of binding and dissociation are observed). It can also be time consuming to select the traces that contain functional signal (for instance, some ZMWs are empty, contain multiple molecules and/or contain noise and other unwanted artefacts). Therefore, analysis of such data manually is tedious, and the researcher devotes significant time, which could be spent elsewhere. In a typical experiment, binding of one molecule to the other is detected via cycles of FRET, which can easily be detected by certain software.

Software for automated analysis and fitting of smFRET data have been described previously (Blanco and Walter 2010; Bronson et al. 2009, Hadzic et al. 2018, McKinney et al. 2006). However, the data generated from the RS II instrument cannot be directly loaded into these programs, because the format does not quite match the input requested by the software. The RS II has four spectral channels which are stored in a matrix in MATLAB, whereas the analysis software is expecting only two (e.g, a FRET pair such as Cy3-Cy5). Therefore, before attempting to load the data into such software for analysis, a few processing steps are required. I have written basic code in MATLAB that resolves this and drastically shortens the time required for data analysis. The software doing the analysis is usually more efficient (taking less time) and accurate than human input (better at detecting events), provided that the data is not noisy in the acceptor channel and the state transitions are clear. The software is also more consistent between experiments and traces and therefore generates more confidence in the data. After selecting the traces to be analyzed using the Puglisi laboratory scripts described previously, the user can simply run the code and then load the file generated into analysis software. I have tried several analysis software, such as vbFRET, ebFRET, SPARTAN, and HaMMy (McKinney et al. 2006, Bronson et al. 2009, Asher et al. 2021). I found ebFRET (van de Meent et al. 2014) to be the best for our application, in terms of software and operating system compatibility, accuracy, and speed.

Results

The first processing step used for automating the data analysis process is removing the portion in the movies where there is no laser excitation. In the RS II, there is usually some part in the movie where the laser has not turned on (Figure 3.1.). This is from a delay in the instrument, the molecules cannot be observed without laser excitation and the background is also much less), even though the instrument has started recording the movie. This needs to be excluded, otherwise the software will either exclude the trace as photobleaching, or erroneously assign it as another FRET state. I have worked around this by setting a simple threshold for the donor fluorophore channel, where all the frames in the movie prior to reaching a certain intensity would be removed. Note that this would not work for static experiments and is better for an experiment where the movie is started, followed by molecules containing the acceptor fluorophore being injected into the sample. However, it should be relatively straightforward to simply alter the threshold (or use the acceptor channel's background as a threshold) to adapt this to a static experiment (where both the donor and acceptor are present at the start of the movie, and FRET is observed from the beginning of the movie). If not, the user can also manually delete the frames where the laser is not turned on in the MATLAB matrix.

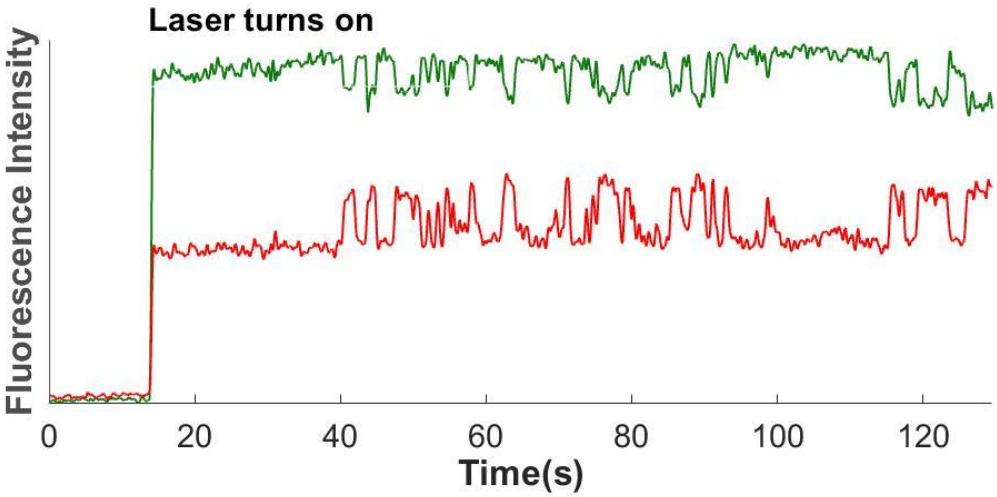

Figure 3.1. Example delay is laser excitation. No fluorescence is observed in the first ~16 seconds of the movie due to a delay in the lasers. The fluorescence is detected after the laser is turned on, and the part of the movie without laser excitation needs to be removed for automated analysis.

The software used for analyzing the output, ebFRET, is available online, we typically use the modified version that is titled xlim-fix that is available via GitHub (https://github.com/ebfret/ebfret-gui/tree/xlim-fix). We use the GUI-based version launchable through the MATLAB command window when the ebFRET files are added to the default MATLAB path. Executing the following set of commands is sufficient to convert data generated by the RS II into a format that is readable by the software called ebFRET (van de Meent et al. 2014) (and a few others).

```
ttotal2=ttotal(:,2:2:end);
for i=1
while mean(ttotal2(i,:))<90
```

```
ttotal2(i,:)=[];
end
end
i=2;
while i<size(ttotal2,2)
  ttotal2(:,i)=ttotal2(:,i)-normfit(ttotal2(1:150,i));
  i=i+2;
end

data=ttotal2;
z=zeros(size(data,1),2);
for x=1
while x<size(data,2)
   z=horzcat(z, (data(:,x)-60));
   z=horzcat(z, (data(:,x+1)));
   x=x+2;
end
end
z(:,1)=[];
z(:,1)=[];

% z(z<0)=0;
```

```
z=double(z);

save data.dat z -ascii
```

The user needs to load the extracted file containing the matrix with all the trace data into the MATLAB workspace. In our workflow, this is typically a file called Run_001-p.mat or Run_filter_61.mat (the numbers “001” and “61” can vary between files that have split up data). Note that several of the names included here in the scripts for the output file, matrix, as well as the variables themselves are arbitrary. Once run on a data file containing picked traces, these commands will then work on it and create a .dat file that can be loaded directly into ebFRET.

It is possible to run it on traces that have not been picked, however, the user needs to be careful because this can cause software instability due to the large amount of data handled (in this case, the user would have to exclude traces unsuitable for analysis in ebFRET, which is more time-consuming. However, if most of the traces have functional signals, this is possible to do). I have made a slight modification to this code, which also allows it to be used on a Cy3.5-Cy5 FRET pair (which we have also used to probe eIF4E-mRNA interaction). Note that there is no correction here for the cross-talk between the two channels (which is significant between Cy3.5-Cy5 due to the spectral overlap, Chen et al., 2014), and this is only for identifying appearance or disappearance of FRET:

```
for i=2
while mean(ttotal(i,:))<90
ttotal(i,:)=[];
end
end
data=ttotal;
z=zeros(size(data,1),2);
for x=3
while x<size(data,2)
   z=horzcat(z, (data(:,x)-70));
   z=horzcat(z, (data(:,x+1)-normfit(data(1:120,x+1))));
   x=x+4; %move on to next molecule
end
end
i=1;
j=1;
z(:,1)=[];
z(:,1)=[];

z=double(z);
save data.dat z -ascii
```

In addition to this script, I have written other variations, that would also write each trace to a different text file which would then make it readable by other software that requires each trace be written to a separate file:

```
ttotal2=ttotal(:,2:2:end); %extract even numbered columns, to get cy3 and cy5 intensity. If using other channels this will not work!
for i=1
while mean(ttotal2(i,:))<90 %remove frames before the green laser is turned on
ttotal2(i,:)=[];
end
end
i=2;
while i<size(ttotal2,2)
  ttotal2(:,i)=ttotal2(:,i)-normfit(ttotal2(1:150,i)); %corrects red background on a per-trace basis
  i=i+2;
end

data=ttotal2;

for x=1
```

```
    while x<size(data,2)
      z=[];
      z=horzcat(z, (data(:,x)-60)); % add cy3 channel, background is usually 60
      z=horzcat(z, (data(:,x+1)));
      z=double(z);
      fname=strcat('molecule', num2str(x));
      save([fname '.txt'], 'z', '-ascii') ;
      x=x+2;
    end
end
```

Upon filtering of the trace data, ebFRET can then be used to detect FRET states. The output file of the scripts can be loaded directly into the ebFRET GUI which is launched through MATLAB. To proceed with analysis, the parts of a trace where photobleaching occurs must be removed. Fortunately, the software has a tool that aids this, along with the option of manually cropping each trajectory on the time axis. Once the traces have been processed to remove photobleaching, the user can then force the software to fit the data to two states (where state 2 is always a “bound” state). Due to the Bayesian statistics used by the software, it tends to get more accurate at identifying states when it is provided with a larger dataset. The number of restarts (typically at least two passes) as well as precision of the software can be increased by the user to make the software

more stringent at assigning states, at the cost of speed. However, for our datasets, I have found that >6 restarts gives only a marginal improvement. In addition, the priors are typically set to 0 for the minimum FRET efficiency and 0.25 for the maximum (the minimum is zero because we have no FRET when the ligand is not bound, it would not be zero if the system is designed to always induce a FRET signal, such as in our intramolecular RNA smFRET experiments).

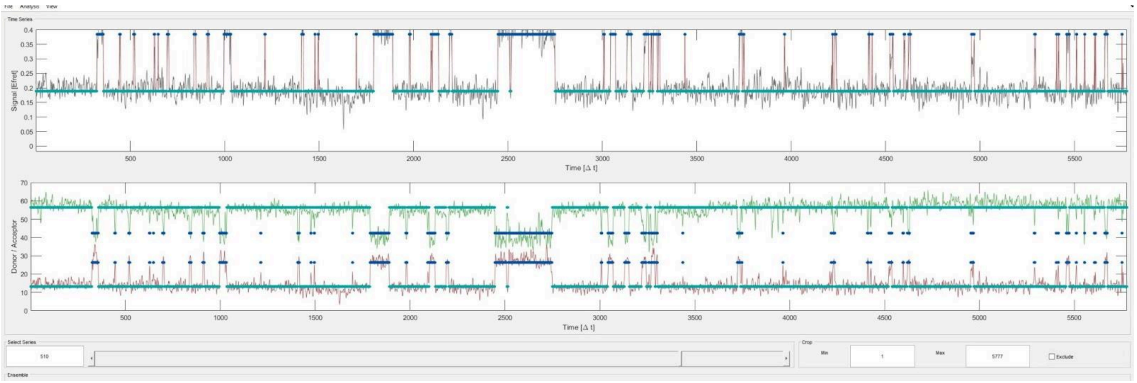

Figure 3.2. Example state assignment of smFRET traces from the RS II using ebFRET. In this scheme, the ebFRET software marks all event positions with a darker blue color (assigning it as state two), whereas the frames where FRET is not observed are marked with turquoise (assigning as state one).

Note that the FRET efficiency plotted here is usually not correct. While providing a rough estimate, the user would have to correct the background for the donor channel properly for accurate estimation of the FRET efficiency. In addition, we have never calibrated our RS II-based experimental setup and imaging system using a donor-acceptor pair with known distance, which is usually required to ensure that the system and the data analysis scheme is reporting distance

changes accurately. Fitting the data to three states and using the third state for the FRET efficiency using the default parameters usually gives the best separation of FRET efficiency data from noise. The software is usually good at setting priors when loading the data, the minimum center can be set to 0, since the experiments here will always have a state zero (no) FRET because eIF4E dissociates. In addition, the hybridization oligonucleotide used here probably binds at different sites throughout the poly(A) tail, changing the end-to-end distance, which would complicate the measurement because the tail is longer than 45 nucleotides.

If provided noisy data, the software will occasionally make mistakes and a significant amount of user input and data exclusion will be required. The ebFRET session can be saved in the GUI, allowing the user to save their progress and return to data analysis at any point. This saved file contains all the event data.

An additional script was developed to convert the ebFRET output file to a matrix where the events are scored for each frame (e.g, marking where the event occurred in each frame). Example commands for that is shown here, this basically extracts all the event positions from the ebFRET:

```
state = {analysis(2).viterbi.state}.';
state1=state(~cellfun('isempty', state));
z=zeros(5900,1)
 for x=1
```

```
while x<=length(state1)
   b=cell2mat(state1(x)) %extract numeric array from cells containing FRET state
data
   x=x+1 %advances to next molecule
if length(b)<5900
   b=vertcat(b,(zeros((5900-length(b)) ,1)))
   z=horzcat(z,b)
end
end
 end
HMM=z-1;
HMM=max(HMM,0)
```

The matrix called “HMM” after this will now contain the event positions (e.g, which frames had an event occur). The co-authors on our earlier manuscript (Çetin et al. 2020) had previously developed scripts for generating the kinetics in a population. I made amendments to that script that also allows one to extract the aggregate kinetics for the entire population (combining all the events from all molecules). This can then be subjected to exponential fitting, determining the rates from the entire population using ebFRET, rather than executing a set of commands on the file containing the picked traces. The data is in frames (instead of seconds) and the obtained rates would need to be divided by the number of

frames to compute the rate per second. Since we typically record movies at ten frames/second, I have set it to divide the rates by ten. This workflow significantly reduces the time required for data processing (at least ten-fold), especially for an interaction such as eIF4F-mRNA (which is characterized by rapidly reversible binding and dissociation under our experimental conditions). This allows rapid analysis of data from experiments that require a large number of molecules, such as the transcriptome-wide experiments that determine the dynamics of the interaction at a larger scale. However, an algorithm which automates the selection of traces is also required to streamline data analysis.

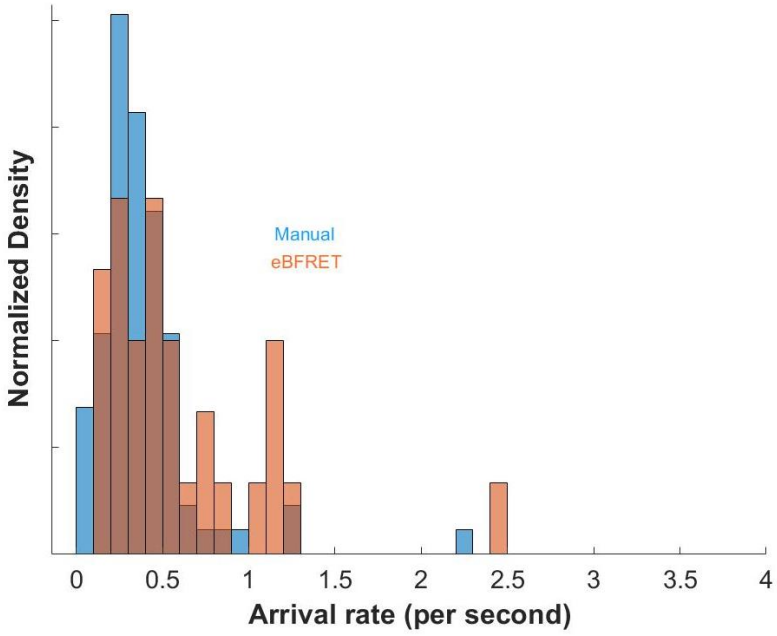

Figure 3.3. Comparison of manual and automated state assignment.

Conclusions and Future Directions

In this study, we systematically characterized the dynamics of the eIF4F-mRNA interaction on full-length yeast mRNAs in vitro, for which no kinetic data was available (past work was limited to shorter RNAs and model oligonucleotides). Our results allowed construction of a detailed kinetic model for the interactions (Figure 4.1.).

Yeast eIF4E binds shorter mRNAs faster in vitro, which is reduced by other initiation factors that make it recognize mRNAs with less variation. Given our finding that mRNA length impacts the eIF4E association rate, these results highlight how information encoded along the mRNA length intrinsically contributes to the efficiency of early initiation and offers one explanation for why longer mRNAs are often translated less efficiently and with higher eIF4F dependence. Moreover, reduction in the availability or activity of any one eIF4F subunit is expected to impact different mRNAs differently in this model. Short mRNAs and/or less structured mRNAs that effectively compete for eIF4F–cap binding are predicted to be less sensitive to depletion of active eIF4F. mRNAs that associate faster with eIF4F might be expected to have an advantage in terms of translational efficiency under conditions such as stress where eIF4F activity is downregulated, provided they do not accumulate in stress granules or P bodies. Other factors also make recognition more efficient. The free fraction of eIF4A can accelerate binding of eIF4E to mRNAs, and eIF4G prolongs the

interaction between eIF4E and mRNA, which was demonstrated on both native mRNA extracted from cells, and in vitro transcribed model mRNAs. While eIF4G can bind throughout the mRNA, the presence of eIF4E biases accommodation at the 5′ end. Our results implicate eIF4A as an RNA chaperone which can stimulate interaction of translation factors with mRNAs. The eIF4E-mRNA interaction has an equilibrium dissociation constant in the low nanomolar range. The variability in the interaction is mainly driven through association rates, which likely controls ribosome recruitment through the kinetics of the eIF4E-mRNA interaction.

Overall, we determined that eIF4G is the main contributor to the dynamics, and that eIF4A can also exert an effect, both on individual mRNAs and on mRNA populations. We obtained modest correlations to *in vivo* binding and good correlation ribosome occupancy data, although on a small sample of mRNAs. Other factors and RNA-binding proteins in cells may further modulate the dynamics of the interaction to lead to the interaction profiles observed *in vivo*. It will be important to test how factors like eIF4B (which stimulates eIF4A activity), affect the dynamics of the interaction. Furthermore, factors like Ded1p interact with eIF4F components, and

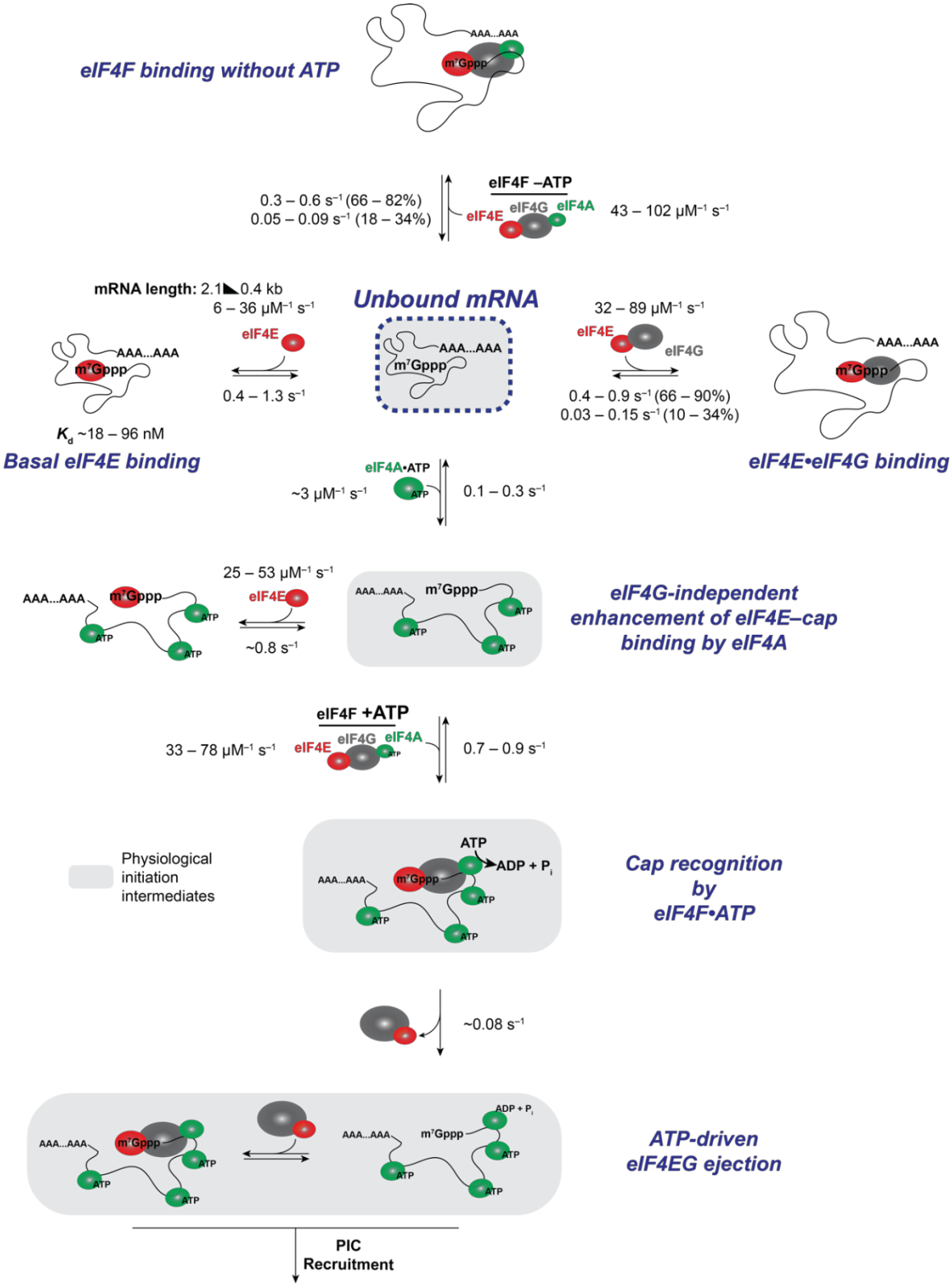

Figure 4.1. Model summarizing kinetic data for eIF4F-mRNA interactions.

The kinetics of eIF4E-mRNA complex formation evidently vary between different mRNAs and offer a point of regulation during translation initiation. mRNAs that inherently form a complex with eIF4F at higher rates would be less sensitive to reduced eIF4E levels, or conditions where the active levels of eIF4E are reduced (such as binding of 4E-binding proteins to eIF4E, sequestering it away from eIF4G and preventing activation of mRNAs). Furthermore, our multicolor experiments dissected the mechanism of eIF4F-mRNA complex formation on different mRNAs, which was largely similar across three different transcriptstested in our experiments. We determined that ATP binding and hydrolysis by eIF4A likely triggers conformational changes in the intact eIF4F complex, and that eIF4E is likely to dissociate from the cap structure after initial binding. This is in the absence of ribosomes, or a scanning complex present on the mRNA. eIF4E-G is likely to dissociate first, leaving eIF4A bound to the mRNA, which remains bound to potentially recruit another eIF4E-G complex. eIF4G is typically considered to be a “scaffold” for eIF4F assembly. However, our results indicate that eIF4A can also act as a scaffold in yeast. eIF4E dissociating from the mRNA after assembly of the eIF4F complex contrasts with the expectation from previous results that eIF4E remains bound to the cap structure throughout scanning (Bohlen et al. 2020). This observation may be due to using yeast initiation factors in our experimental system, which may bind more transiently. ATP concentration also impacts eIF4F-mRNA association, where excess ATP would make the interaction more efficient. This would suggest that

eIF4F-mRNA interactions are reduced upon conditions that reduce the available [ATP] in the cell, such as stress (Mendelsohn et al. 2018). Since the effect was demonstrated on a population-wide experiment, this could be a global effect, or clusters of mRNAs may be less likely to bind eIF4E when ATP is depleted.

ATP binding and hydrolysis also play important and distinct roles. ATP binding induces a conformational change in the eIF4F complex bringing eIF4E and eIF4A within FRET distance, whereas hydrolysis triggers ejection from eIF4E from the cap structure. The dynamics of the eIF4F•mRNA complex suggest a mechanism for coordinating eIF4F–cap recognition with PIC recruitment, and for conferring mRNA sensitivity to distinct translational control pathways. The structure of some of the core initiation factors (such as eIF4A and eIF4G) is rather different between yeast and mammals. Mammalian eIF4G includes an additional eIF4A-interacting domain which may prolong the lifetime of the complex relative to the yeast counterpart. More experiments would be required to address whether this is also the case for the mammalian system. Furthermore, mammalian mRNAs are generally longer and more structurally complex due to their higher GC content. Hence, it will be important to separately characterize these dynamics for mammalian eIF4F in future experiments.

We also isolated recombinant Ded1p and eIF4B for future studies. These components are known to interact with eIF4F subunits (Gao et al., 2016, Gulay et al., 2020), and hence can make an impact on the interaction between eIF4F and the mRNA. It will be important to address this with eIF4F and additional factors. The inclusion of poly(A) binding protein may further modulate the dynamics of the interaction. Ultimately, the study was a thorough characterization of yeast eIF4E and eIF4F binding to mRNAs, and further studies will elucidate the dynamics when other factors and RNA-binding proteins are present.

Chapter 5: Materials and Methods

In vitro transcription, RNA processing and labeling of oligonucleotides

DNA templates to be transcribed were PCR-amplified from Yeast Genomic DNA (EMD Millipore) with Phusion DNA polymerase (NEB) using standard procedures. Primers sequences are reported in previous publications. A T7 promoter (TAATACGACTCACTATAGG) was incorporated into the PCR product through the forward primer, where the underlined bases become +1 and +2 nucleotides added to the transcript. Adding the two guanosines is necessary to obtain sufficient yield for when conducting transcription.

The resulting templates were *in-vitro* transcribed to produce RNA using in-house purified or commercial (NEB) T7 RNA. Transcription reactions were typically carried out on a 40 µL scale, with ~5 µg of DNA template, in a buffer consisting of 200 mM Tris-HCl, pH 7.9, 0.05% (v/v) Triton-X-100, 15 mM spermidine, 2 mM each NTP and 5 mM DTT. $MgCl_2$ concentrations in this buffer were optimized for each transcript by titration, and were 15 – 30 mM. Unreacted nucleotides were removed from the transcription mixture with MicroBio-Spin gel filtration columns (P30, Bio-Rad), and the RNA product was then precipitated using ½ volumes of 7.5M lithium chloride. The resulting RNA pellet was redissolved after three

washes with 80% EtOH and run on a native 1% TBE-Agarose gel, to check for integrity. The RNAs were then capped using the ScriptCap™ m^7G Capping System (CellScript) with the following modifications to the manufacturer's protocol: the incubation time with the capping enzyme was increased to two hours, and the volume of enzyme added was increased twofold. A poly(A) tail was added to the mRNA immediately after capping, using *E. coli* poly(A) polymerase (NEB), following the manufacturer's guidelines. The capped and tailed mRNA was then re-purified by organic extraction with acidic phenol-chloroform, precipitated with 0.1 volumes of 3 M sodium acetate and two volumes of ethanol, and resuspended in RNase-free water.

To assess the capping efficiency, the JJJ1 , HXT2, and NCE102 RNAs were desalted using MicroBioSpin gel filtration columns (BioRad) after capping and treated with RNA 5′ polyphosphatase (Epicentre) and RNA 5′ Terminator dependent exonuclase (Epicentre) for one hour for each enzyme. Batches of the same RNA, either capped and uncapped, were treated separately, and RNA integrity was assessed on a 1.2% TAE-Agarose gel immediately after treatment. For obtaining an estimate of the poly(A) tail length, RNA was run on a 1.5% TAE-agarose gel for 20 minutes at 120V after poly(A) tailing, loaded next to the same mRNA lacking a poly(A) tail, staining using EtBr.

5' biotinylated and 3' amino-modified oligonucleotides purchased from IDT were reacted with a 1:8 molar ratio of oligonucleotide to NHS-ester derivatives of Cy5

(for intramolecular FRET experiments with dual labeled RNA), Cy3 and Cy3.5 in 0.1 M sodium bicarbonate for four hours at room temperature, followed by four successive chloroform extractions to remove unreacted dye, and by buffer-exchange into ddH_2O using MicroBio-Spin gel filtration columns (P30, Bio-Rad). Labeling efficiency was typically 75% as measured by UV/visible spectrophotometry. The labeled oligonucleotides were stored at –20 ˚C and used without further purification.

For EMSAs, RNA (20 nM based on A260) was incubated with eIF4G truncations (800 nM) or full-length eIF4G (400 nM) for five minutes in 1x Assay Buffer (50 mM HEPES-KOH, pH 7.4, 3 mM Mg $(OAc)_2$, 100 mM KOAc), and run on a 1.5% TAE-agarose gel at 6C for 30 minutes at 80V. Bound complexes were visualized using gels including EtBr.

Yeast growth and total RNA isolation.

A 5 mL starter culture of the yeast strain W303 (a generous gift from Justin Chartron, UC Riverside) was grown in 5 mL YPAD medium at 30 ℃ overnight. The starter culture was then used to inoculate 1 L of YPAD medium, and the culture was grown overnight at 30 ℃, to stationary phase (O.D.600~ 3.0). Cells were then harvested by centrifugation (at 4,000 × gfor 10 minutes at 15 ℃). The resulting cell pellet was washed twice with ddH2O to remove traces of growth medium, and was then resuspended in 25 mL RNA Lysis Buffer (50 mM Tris-HCl, pH 8.0 at 4C, 2% SDS, 2% b-mercaptoethanol, 10 mM EDTA). Cells were

lysed by vortexing with zirconium beads (0.5 mm; 33% (v/v) BioSpec), through five cycles of one-minute vortexing followed by a two-minute pause with incubation on ice.

The resulting lysate was centrifuged at 13,000 × g for ten minutes at 4℃, and the supernatant was recovered. The supernatant, containing soluble protein and nucleic acids, was then subjected to two successive extractions with 1 volume of acidic phenol-chloroform (pH 4.5) to enrich for RNA. The aqueous phase was recovered, and nucleic acids were precipitated using 2.5 M LiCl. The resulting pellet was washed twice with 80% EtOH and resuspended in ddH2O (typically ~1 mg /mL based on the 260-nm absorbance in a volume of ~4 mL). The total RNA preparation was first assessed for degradation on a 1% TBE-agarose gel, staining with ethidium bromide. To optimize the density of immobilized mRNA molecules in the ZMW array for single-molecule analysis, the RNA was then concentrated using Vivaspin® 6 centrifugal concentrators (Sartorius, MWCO 10 kDa), and aliquots were stored at –20 ℃. Quality of RNA preparations was further assessed by BioAnalyzer size distribution analysis.

Protein purification and labeling

Genes encoding translation factors were expressed from pET-28a(+) (Qiagen) or pTYB2 (New England Biolabs). Overexpression was carried out at 37 ˚C in LB medium, in volumes ranging from 1 L to 12 L. *E. coli* BL21(DE3) CodonPlus RIL

or BL21(DE3) cells expressing the target recombinant protein were grown to an OD_{600} of 0.5 – 1 at 37 ˚C.

Overexpression was then induced *via* addition of 0.5 mM IPTG, then the overexpression was allowed to proceed overnight at 16 ˚C. For eIF4G, the induction was carried out at 37 ˚C for 2 – 3 hours. The resulting cells were harvested and stored at –80 ˚C until purification.

His_6-tagged yeast eIF4E(A124C) was purified as described previously (O'Leary et al., 2013). Briefly, cell lysate from the overexpression culture was loaded onto a gravity-flow Ni-NTA agarose column (Qiagen) pre-equilibrated with eIF4E buffer (50 mM HEPES-KOH, pH 7.4, 150 mM KCl, 2.5 mM TCEP). The column was then washed with 40 column volumes of eIF4E buffer containing 40 mM imidazole to remove nonspecifically bound proteins, then eIF4E was eluted using eIF4E buffer containing 250 mM imidazole. Imidazole was removed from the protein eluate by desalting on a Bio-Rad 10-DG column equilibrated in containing 50 mM HEPES-KOH, pH 7.4, 150 mM KCl, 0.5 mM TCEP. The resulting protein was immediately labeled with a sulfonated Cyanine 5 maleimide (Lumiprobe) overnight at 6 ˚C in darkness. Unreacted fluorophore was then removed by desalting on a BioRad 10-DG column. The labeled protein was purified by gel filtration using a Superdex 75 Increase column (GE healthcare), equilibrated in storage buffer (50 mM HEPES-KOH, pH 7.4, 150 mM KCl, 2.5 mM TCEP). The labeling efficiency was assessed by UV/visible spectrophotometry and was

typically ~50%. The protein was stored at 6 ˚C in darkness, and was prepared freshly every week as needed.

The plasmid containing recombinant full-length eIF4G1 was a gift from Sarah Walker (also available from Addgene as plasmid #122248). This full-length eIF4G1 construct with a C-terminal chitin binding domain fusion was purified according to a published procedure (Liu et al., 2019), with the following modifications: the cells were lysed using a sonicator, and the final protein after elution was stored in 250 mM KCl instead of 250 mM KOAc, skipping the dialysis after the anion-exchange chromatography step in the procedure, and DTT for storage was substituted with 2.5 mM TCEP. Briefly, *E. coli* cells expressing full-length eIF4G1 were thawed, and lysed using a sonicator after resuspending in Intein Lysis Buffer (50 mM HEPES-KOH, pH 7.4, 500 mM KCl, 1 mM EDTA). The lysate was then clarified by centrifugation at 20,000 × *g* for 15 minutes. The clarified lysate was rocked with 4 mL of chitin resin (New England Biolabs) for 30 minutes at 4 ˚C. The resin was then loaded into a gravity-flow column and washed with 100 mL of Intein Lysis Buffer. The column was then treated with micrococcal nuclease to remove nucleic acids from *E. coli* which co-purified with eIF4G. Briefly, the resin was first equilibrated with micrococcal nuclease buffer (50 mM HEPES-KOH, pH 7.4, 100 mM KCl, 2 mM $CaCl_2$). Then, a 3 mL solution containing 3 U/μL micrococcal nuclease was passed through the column. The resin was then incubated for 30 minutes at 37 ˚C.

Following nuclease treatment, the column was washed with a further 50 mL of lysis buffer. The column was then flushed with 8 mL of lysis buffer containing 50 mM DTT, and 6 mL was allowed to pass through the column, which was then sealed and incubated overnight at 6 ˚C. The following day, the cleaved protein was eluted with 10 mL of lysis buffer. The resulting protein solution was diluted to 100 mM KCl with lysis buffer lacking KCl, then manually loaded onto a Q HP column (1 mL; GE Healthcare Life Sciences) equilibrated in 50 mM HEPES-KOH, pH 7.4, 10% (v/v) glycerol, 2.5 mM TCEP, 100 mM KCl, and washed with five column volumes of buffer containing 50 mM HEPES-KOH, pH 7.4, 10% (v/v) glycerol, 2.5 mM TCEP, 100 mM KCl. The column was then eluted manually with a step-gradient of 150, 200, 250 mM KCl in 50 mM HEPES-KOH, pH 7.4, 10% (v/v) glycerol, 2.5 mM TCEP (one column volume for each step). Eluate fractions were analyzed by SDS-PAGE; eIF4G typically eluted above ~220 mM KCl. Single-use aliquots of purified eIF4G1 were prepared and were stored at –80 ˚C. For non-specific fluorescent labelling, single-use aliquots of the eIF4G protein were treated with an equimolar concentration of Sulfo-Cy5.5 Maleimide (Lumiprobe) resuspended as a 2 mM stock in DMSO, for a total of two hours. The resulting fluorescent protein was then immediately used in the single molecule experiments. The His_6-tagged $eIF4G_{1–452}$ fragment (an *NdeI* fragment of the eIF4G1 CDS) was purified essentially as for eIF4E, but 1 M KCl was included in the purification buffers.

His_6-tagged recombinant eIF4A was purified as described previously. *E. coli* cells expressing recombinant eIF4A were first thawed and resuspended in eIF4A lysis buffer (50 mM HEPES-KOH, pH 7.4, 300 mM KCl, 2.5 mM TCEP). After sonication for cell lysis, the resulting lysate was clarified by spinning at 20,000 × *g* for 15 minutes. The clarified lysate was applied to Ni-NTA agarose (equilibrated in lysis buffer) as a first step, after filtering the lysate through a 0.22 µm syringe filter. The bound protein was eluted with lysis buffer containing 250 mM imidazole after washing with 10 column volumes of lysis buffer containing 40 mM Imidazole. The eluate was buffer-exchanged to Buffer A using a BioRad 10-DG column (50 mM HEPES-KOH, pH 7.4, 100 mM KCl, 2.5 mM TCEP) and subjected to anion-exchange chromatography using a 5 mL Q HP anion-exchange column (GE Healthcare). The column was eluted with a linear gradient of 0.1 – 1 M KCl. eIF4A typically eluted at 250 mM KCl. Fractions containing eIF4A were identified by SDS-PAGE analysis, then pooled, concentrated by centrifugal ultrafiltration, and further purified by gel filtration chromatography using a Superdex 200 column (GE healthcare) equilibrated in 50 mM HEPES-KOH, pH 7.4, 100 mM KOAc, 2.5 mM TCEP, 10% (v/v) glycerol. The final protein sample was divided into single-use aliquots and stored in storage buffer at –80 ˚C. 6x Histidine-tagged recombinant eIF4G (83-452) was expressed in a pET-28a(+) vector using E. coli BL21(DE3) CodonPlus RIL cells, under dual selection with chloramphenicol and kanamycin. The resulting transformants were grown in

a 10 mL starter culture at 37C for 16h. A 2L LB medium flask was inoculated with this culture, and the culture was grown until an O.D.600 value of 1. Overexpression was then induced via addition of 1 mM IPTG, then the overexpression was allowed to proceed overnight at 16 ˚C. Cells were harvested and resuspended in 30 mL of lysis buffer (50 mM HEPES-KOH, pH 7.4, 150 mM KCl, 2.5 mM TCEP, 40 mM imidazole). The resuspended cells were lysed using a sonicator, and the lysate was by centrifugation at 20,000 × g for 15 minutes. The lysate was then passed through a 0.2 micron filter and applied to a 1 mL HisTrap column (Cytiva) equilibrated with 5 column volumes of lysis buffer. The column was washed with 5 mL of lysis buffer, then the protein was eluted using a lysis buffer containing 250 mM imidazole. The resulting eluate was diluted 3-fold using lysis buffer without salt or imidazole, and applied to a 1 mL HiTrap Heparin column (Cytiva) equilibrated in buffer containing 50 mM HEPES-KOH, pH 7.4, 10% (v/v) glycerol, 2.5 mM TCEP, 100 mM KCl. The column was washed with 5 column volumes of the same buffer, and bound protein was then eluted with the same buffer containing 250 mM KCl. The eluted protein was stored at -80C.

For preparation of labeled eIF4A, a construct was designed that expresses the native eIF4A sequence with an N-terminal Met-Ala-(*p*Az)Phe tripeptide extension for unnatural amino acid incorporation. This plasmid was co-transformed into *E. coli* BL21(DE3) cells with the pEVOL-ps plasmid (a generous gift from Abhishek Chatterjee, Boston College) under dual selection with chloramphenicol and kanamycin. The resulting transformants were grown in a 10 mL starter culture

overnight. Afterwards, a 1 L LB medium flask was inoculated with the starter culture and grown to an $O.D._{600}$ value of 0.5. 1 mM 4-azidophenylalanine was then added to the culture medium along with 2 mM arabinose to induce tRNA/aminoacyl-tRNA synthetase expression. Finally, 2 mM IPTG was added to induce expression of eIF4A. Overexpression was allowed to proceed for 5 hours in darkness, to avoid photochemical damage to the unnatural amino acid. The cells were harvested and stored at –80 ˚C until purification. MA(*p*AzF)-eIF4A was purified identically to unlabeled recombinant eIF4A, with the exception that after initial Ni-NTA purification the protein was treated with DBCO-Cy3 overnight to conjugate the fluorophore to the unnatural amino acid. Ded1p was isolated according to a published protocol (Iost et al., 1999).

Steady-state ATPase assay for eIF4A activity.

The NADH-coupled ATPase assay was carried out according to a published procedure. Briefly, reactions were assembled on ice and started by adding Mg-ATP. The reaction was set up with the KMg75 buffer (20 mM HEPES-KOH, pH 7.4, 75 mM KCl, 1 mM DTT, 5 mM $MgCl_2$), 250 nM eIF4A or Cy3-eIF4A, 125 nM full-length eIF4G, 1 mM ATP, 1 mM (measured as concentration of bases) poly(U) RNA (Sigma), lactate dehydrogenase (20 U/mL final concentration), and pyruvate kinase (100 U/mL) Absorbance was recorded at 340 nM with a Shimadzu UV2600 UV-visible spectrophotometer, measuring the decrease of NADH absorbance with time. The slope of the absorbance *vs*. time graph was converted to the rate of ATP hydrolysis using an extinction coefficient of 6,220 M^{-1} cm^{-1} for NADH, and normalized to the eIF4A concentration to yield V / E_0. Control reactions to establish the background rate of NADH oxidation included no eIF4A and no RNA.

Single-molecule experiments

The custom RS instrument was set up as described previously. The RNA to be immobilized was hybridized through its poly(A) tail to $(dT)_{45}$ conjugated to biotin at its 5' end and Cy3 or Cy3.5 at its 3' end, to act as a FRET donor. Annealing was performed using a thermocycler, by heating 100 nM labeled oligonucleotide to 98 ˚C for two minutes in the presence of two- to five-fold molar excess of mRNA, followed by cooling to 4 ˚C at a ramp speed of 0.1 ˚C s^{-1}. The resulting mRNA:$(dT)_{45}$ duplex was diluted to 3-10 nM fluorophore in smFRET assay buffer prior to immobilization on the ZMW using the assay buffer.

Zero-mode waveguides were set up as described previously (Chen et al., 2014). Briefly, the ZMW chip was hydrated with assay buffer (final concentrations of 50 mM HEPES-KOH, pH 7.4, 3 mM $Mg(OAc)_2$, 100 mM KOAc) for two minutes, followed by incubation with 16 μM NeutrAvidin (Thermo Scientific) for five minutes to allow immobilization of biomolecules. The chip was then washed three times with the assay buffer, followed by addition of 10 nM mRNA:biotin-$(dT)_{45}$-Cy3.5 duplex, which was allowed to immobilize for 20 minutes. The chip was then washed again three times to remove non-immobilized nucleic acids, and an imaging buffer containing PCA/PCD oxygen scavenging system and photostabilizer (TSY) was added.

Prior to imaging on the RS II, the chip was treated with 5% (v/v) each of BioLipidure 203 and 206, 1 mg/mL BSA and unlabeled eIF4E; this blocking step mitigates non-specific Cy5-eIF4E interactions with the surface. Inclusion of this step did not detectably alter the kinetics of eIF4E-mRNA interaction. After initiating the imaging on the RS II, between 4 and 30 nM Cy5-eIF4E were robotically injected onto the waveguide, starting the binding reaction. Where unlabeled eIF4G, and/or unlabelled or Cy3-eIF4A were included in experiments, they were co-delivered with Cy5-eIF4E at the concentrations indicated in the results section. Subunits were pre-incubated for ~15 minutes prior to co-delivery. The ZMWs were imaged with 10-minute movies acquired at 10 frames/second, at 0.7 μW/μm^2 green (532 nm) laser power and 0.07 μW/μm^2 red (642 nm) laser power (for dual illumination experiments).

Single-molecule data processing and analysis

Raw movie data were extracted and analyzed with an in-house MATLAB processing pipeline as described previously (Chen et al., 2014). Image files were first converted to fluorescence *vs.* time traces. The locations of events in the traces were then manually assigned, resulting in distributions of event and inter-event durations (i.e., lifetimes and arrival times).

For the two-color FRET experiments, events showing anticorrelated bursts between the FRET donor and acceptor were picked and manually assigned as FRET. For kinetic analysis, arrival-time or lifetime distributions for two-color smFRET experiments were constructed from analysis of events occurring on at least ~100 mRNA molecules, which included at least 500 events, and typically more than 1,000 events. Addition to the analysis of further molecules beyond this number neither significantly altered the kinetic parameters obtained, nor improved the quality of data fitting. Empirical cumulative distribution functions for unbinned distributions were fit in MATLAB, using nonlinear least-squares regression, to either single-exponential (1) or double-exponential (2) models, as appropriate:

$$P(t) = 1 - Ae^{-kt} \quad (1)$$

$$P(t) = A(1 - e^{-kt}) + (1 - A)(1 - e^{-lt}) \quad (2)$$

For double-exponential arrival-time distributions, the fast-phase rate, which typically constituted at least 70% of the amplitude, was used for comparison of eIF4E binding between different mRNAs and conditions.

For goodness-of-fit evaluation, fits typically had an R^2 value > 0.99 (for all distributions generated from experiments with eIF4E-G, eIF4F) and greater than

0.95 (for experiments containing only eIF4E and eIF4E-eIF4A.). Root-mean-squared errors of the fits for arrival-time distributions were typically 0.02 or a lower value; lifetime distributions showed more variable RMSE values with an upper limit of 0.1. For correlation of kinetic parameters with mRNA lengths, and ORF lengths, Pearson correlation coefficients (R) were calculated using GraphPad Prism software (Version 9.1.). Correlations with $p < 0.05$ based on a two-tailed Student's t-test were considered significant. For the three-color FRET experiments, events showing Cy3 signal only were scored as free eIF4A binding. Events showing appearance of Cy3 fluorescence with a concomitant increase in Cy5 fluorescence significantly beyond the negligible expected bleedthrough, and showing apparent FRET efficiency changes during the ensuing binding event, were characterized as eIF4E-eIF4A FRET. A further type of binding event where eIF4E-eIF4A FRET disappeared while eIF4A stayed bound was also scored in both the number of occurrences and the dwell time of the initial FRET event. During these Cy3 fluorescence pulses, the dwell time of FRET when eIF4E-eIF4A FRET reappeared was also quantified. Rate constants were quantified by exponential fitting as described above. For four-color experiments, events showing Cy5.5 signal along with the same frame as a Cy3-Cy5 FRET signal were scored as formation of an eIF4F complex with fluorescent eIF4G.

References

Acker, M. G., Shin, B.-S., Nanda, J. S., Saini, A. K., Dever, T. E., & Lorsch, J. R. (2009). Kinetic analysis of late steps of eukaryotic translation initiation. Journal of Molecular Biology, 385(2), 491–506.

Aitken, C. E., & Lorsch, J. R. (2012). A mechanistic overview of translation initiation in eukaryotes. Nature Structural & Molecular Biology, 19(6), 568–576.

Aitken, C. E., Marshall, R. A., & Puglisi, J. D. (2008). An oxygen scavenging system for improvement of dye stability in single-molecule fluorescence experiments. Biophysical Journal, 94(5), 1826–1835.

Altmann, M., & Linder, P. (2010). Power of yeast for analysis of eukaryotic translation initiation. The Journal of Biological Chemistry, 285(42), 31907–31912.

Amorim, I. S., Lach, G., & Gkogkas, C. G. (2018). The Role of the Eukaryotic Translation Initiation Factor 4E (eIF4E) in Neuropsychiatric Disorders. Frontiers in Genetics, 9, 561.

Andreou, A. Z., & Klostermeier, D. (2013). The DEAD-box helicase eIF4A. In RNA Biology (Vol. 10, Issue 1, pp. 19–32). https://doi.org/10.4161/rna.21966

Andreou, A. Z., & Klostermeier, D. (2014). eIF4B and eIF4G Jointly Stimulate eIF4A ATPase and Unwinding Activities by Modulation of the eIF4A Conformational Cycle. In Journal of Molecular Biology (Vol. 426, Issue 1, pp. 51–61). https://doi.org/10.1016/j.jmb.2013.09.027

Arava, Y., Boas, F. E., Brown, P. O., & Herschlag, D. (2005). Dissecting eukaryotic translation and its control by ribosome density mapping. Nucleic Acids Research, 33(8), 2421–2432.

Archer, S. K., Shirokikh, N. E., Beilharz, T. H., & Preiss, T. (2016). Dynamics of ribosome scanning and recycling revealed by translation complex profiling. Nature, 535(7613), 570–574.

Asher, W. B., Geggier, P., Holsey, M. D., Gilmore, G. T., Pati, A. K., Meszaros, J., Terry, D. S., Mathiasen, S., Kaliszewski, M. J., McCauley, M. D., Govindaraju, A., Zhou, Z., Harikumar, K. G., Jaqaman, K., Miller, L. J., Smith, A. W., Blanchard, S. C., & Javitch, J. A. (2021). Single-molecule FRET imaging of GPCR dimers in living cells. Nature Methods, 18(4), 397–405.

Berset, C., Zurbriggen, A., Djafarzadeh, S., Altmann, M., & Trachsel, H. (2003). RNA-binding activity of translation initiation factor eIF4G1 from Saccharomyces cerevisiae. RNA , 9(7), 871–880.

Bhat, M., Robichaud, N., Hulea, L., Sonenberg, N., Pelletier, J., & Topisirovic, I. (2015). Targeting the translation machinery in cancer. In Nature Reviews Drug Discovery (Vol. 14, Issue 4, pp. 261–278). https://doi.org/10.1038/nrd4505

Blanco, M., & Walter, N. G. (2010). Analysis of complex single-molecule FRET time trajectories. Methods in Enzymology, 472, 153–178.

Bohlen, J., Fenzl, K., Kramer, G., Bukau, B., & Teleman, A. A. (2020). Selective 40S Footprinting Reveals Cap-Tethered Ribosome Scanning in Human Cells. Molecular Cell, 79(4), 561–574.e5.

Borman, A. M., Michel, Y. M., Malnou, C. E., & Kean, K. M. (2002). Free poly(A) stimulates capped mRNA translation in vitro through the eIF4G-poly(A)-binding protein interaction. The Journal of Biological Chemistry, 277(39), 36818–36824.

Bronson, J. E., Fei, J., Hofman, J. M., Gonzalez, R. L., Jr, & Wiggins, C. H. (2009). Learning rates and states from biophysical time series: a Bayesian approach to model selection and single-molecule FRET data. Biophysical Journal, 97(12), 3196–3205.

Cawley, A., & Warwicker, J. (2012). eIF4E-binding protein regulation of mRNAs with differential 5'-UTR secondary structure: a polyelectrostatic model for a component of protein-mRNA interactions. Nucleic Acids Research, 40(16), 7666–7675.

Çetin, B., Song, G. J., & O'Leary, S. E. (2020). Heterogeneous Dynamics of Protein–RNA Interactions across Transcriptome-Derived Messenger RNA Populations. In Journal of the American Chemical Society (Vol. 142, Issue 51, pp. 21249–21253). https://doi.org/10.1021/jacs.0c09841

Chen, J. (2015). The Molecular Choreography of Protein Synthesis: Single-molecule Profiling of Ribosome Recording Phenomena.

Chen, J., Dalal, R. V., Petrov, A. N., Tsai, A., O'Leary, S. E., Chapin, K., Cheng, J., Ewan, M., Hsiung, P.-L., Lundquist, P., Turner, S. W., Hsu, D. R., & Puglisi, J. D. (2014). High-throughput platform for real-time monitoring of biological processes by multicolor single-molecule fluorescence. Proceedings of the National Academy of Sciences of the United States of America, 111(2), 664–669.

Choi, J., Ieong, K.-W., Demirci, H., Chen, J., Petrov, A., Prabhakar, A., O'Leary, S. E., Dominissini, D., Rechavi, G., Soltis, S. M., Ehrenberg, M., & Puglisi, J. D. (2016). N(6)-methyladenosine in mRNA disrupts tRNA selection and translation-elongation dynamics. Nature Structural & Molecular Biology, 23(2), 110–115.

Chu, J., Zhang, W., Cencic, R., O'Connor, P. B. F., Robert, F., Devine, W. G., Selznick, A., Henkel, T., Merrick, W. C., Brown, L. E., Baranov, P. V., Porco, J. A., Jr, & Pelletier, J. (2020). Rocaglates Induce Gain-of-Function Alterations to eIF4A and eIF4F. Cell Reports, 30(8), 2481–2488.e5.

Ciandrini, L., Stansfield, I., & Romano, M. C. (2013). Ribosome traffic on mRNAs maps to gene ontology: genome-wide quantification of translation initiation rates and polysome size regulation. PLoS Computational Biology, 9(1), e1002866.

Costello, J., Castelli, L. M., Rowe, W., Kershaw, C. J., Talavera, D., Mohammad-Qureshi, S. S., Sims, P. F. G., Grant, C. M., Pavitt, G. D., Hubbard, S. J., & Ashe, M. P.

(2015). Global mRNA selection mechanisms for translation initiation. Genome Biology, 16, 10.

Duncan, R., & Hershey, J. W. (1983). Identification and quantitation of levels of protein synthesis initiation factors in crude HeLa cell lysates by two-dimensional polyacrylamide gel electrophoresis. The Journal of Biological Chemistry, 258(11), 7228–7235.

Duss, O., Stepanyuk, G. A., Grot, A., O'Leary, S. E., Puglisi, J. D., & Williamson, J. R. (2018). Real-time assembly of ribonucleoprotein complexes on nascent RNA transcripts. Nature Communications, 9(1), 5087.

Ermolenko, D. N., & Mathews, D. H. (2021). Making ends meet: New functions of mRNA secondary structure. Wiley Interdisciplinary Reviews. RNA, 12(2), e1611.

Etchison, D., & Milburn, S. (1987). Separation of protein synthesis initiation factor eIF4A from a p220-associated cap binding complex activity. Molecular and Cellular Biochemistry, 76(1), 15–25.

Feoktistova, K., Tuvshintogs, E., Do, A., & Fraser, C. S. (2013). Human eIF4E promotes mRNA restructuring by stimulating eIF4A helicase activity. Proceedings of the National Academy of Sciences of the United States of America, 110(33), 13339–13344.

Firczuk, H., Kannambath, S., Pahle, J., Claydon, A., Beynon, R., Duncan, J., Westerhoff, H., Mendes, P., & McCarthy, J. E. G. (2013). Anin vivocontrol map for the eukaryotic mRNA translation machinery. In Molecular Systems Biology (Vol. 9, Issue 1, p. 635). https://doi.org/10.1038/msb.2012.73

Fischer, P. M. (2009). Cap in hand: targeting eIF4E. Cell Cycle , 8(16), 2535–2541.

Gao, Z., Putnam, A. A., Bowers, H. A., Guenther, U.-P., Ye, X., Kindsfather, A., Hilliker, A. K., & Jankowsky, E. (2016). Coupling between the DEAD-box RNA helicases Ded1p and eIF4A. eLife, 5. https://doi.org/10.7554/eLife.16408

García-García, C., Frieda, K. L., Feoktistova, K., Fraser, C. S., & Block, S. M. (2015). RNA BIOCHEMISTRY. Factor-dependent processivity in human eIF4A DEAD-box helicase. Science, 348(6242), 1486–1488.

Gebauer, F., & Hentze, M. W. (2004). Molecular mechanisms of translational control. In Nature Reviews Molecular Cell Biology (Vol. 5, Issue 10, pp. 827–835). https://doi.org/10.1038/nrm1488

Gilbert, W. V., Zhou, K., Butler, T. K., & Doudna, J. A. (2007). Cap-independent translation is required for starvation-induced differentiation in yeast. Science, 317(5842), 1224–1227.

Gingras, A. C., Raught, B., & Sonenberg, N. (1999). eIF4 initiation factors: effectors of mRNA recruitment to ribosomes and regulators of translation. Annual Review of Biochemistry, 68, 913–963.

Graff, J. R., Konicek, B. W., Carter, J. H., & Marcusson, E. G. (2008). Targeting the Eukaryotic Translation Initiation Factor 4E for Cancer Therapy: Figure 1. In Cancer Research (Vol. 68, Issue 3, pp. 631–634). https://doi.org/10.1158/0008-5472.can-07-5635

Graff, J. R., & Zimmer, S. G. (2003). Translational control and metastatic progression: enhanced activity of the mRNA cap-binding protein eIF-4E selectively enhances translation of metastasis-related mRNAs. Clinical & Experimental Metastasis, 20(3), 265–273.

Gribble, F. M., Loussouarn, G., Tucker, S. J., Zhao, C., Nichols, C. G., & Ashcroft, F. M. (2000). A novel method for measurement of submembrane ATP concentration. The Journal of Biological Chemistry, 275(39), 30046–30049.

Grifo, J. A., Tahara, S. M., Morgan, M. A., Shatkin, A. J., & Merrick, W. C. (1983). New initiation factor activity required for globin mRNA translation. The Journal of Biological Chemistry, 258(9), 5804–5810.

Gross, J. D., Moerke, N. J., von der Haar, T., Lugovskoy, A. A., Sachs, A. B., McCarthy, J. E. G., & Wagner, G. (2003). Ribosome loading onto the mRNA cap is driven by conformational coupling between eIF4G and eIF4E. Cell, 115(6), 739–750.

Grüner, S., Weber, R., Peter, D., Chung, M.-Y., Igreja, C., Valkov, E., & Izaurralde, E. (2018). Structural motifs in eIF4G and 4E-BPs modulate their binding to eIF4E to regulate translation initiation in yeast. Nucleic Acids Research, 46(13), 6893–6908.

Gulay, S., Gupta, N., Lorsch, J. R., & Hinnebusch, A. G. (2020). Distinct interactions of eIF4A and eIF4E with RNA helicase Ded1 stimulate translation in vivo. eLife, 9. https://doi.org/10.7554/eLife.58243

Haar, T. von der, von der Haar, T., Ball, P. D., & McCarthy, J. E. G. (2000). Stabilization of Eukaryotic Initiation Factor 4E Binding to the mRNA 5′-Cap by Domains of eIF4G. In Journal of Biological Chemistry (Vol. 275, Issue 39, pp. 30551–30555). https://doi.org/10.1074/jbc.m004565200

Haar, T. von der, von der Haar, T., Gross, J. D., Wagner, G., & McCarthy, J. E. G. (2004). The mRNA cap-binding protein eIF4E in post-transcriptional gene expression. In Nature Structural & Molecular Biology (Vol. 11, Issue 6, pp. 503–511). https://doi.org/10.1038/nsmb779

Hadzic, M. C. A. S., Börner, R., König, S. L. B., Kowerko, D., & Sigel, R. K. O. (2018). Reliable State Identification and State Transition Detection in Fluorescence Intensity-Based Single-Molecule Förster Resonance Energy-Transfer Data. The Journal of Physical Chemistry. B, 122(23), 6134–6147.

Haghighat, A., & Sonenberg, N. (1997). eIF4G dramatically enhances the binding of eIF4E to the mRNA 5′-cap structure. In Journal of Biological Chemistry (Vol. 272, Issue 46, p. 29398). https://doi.org/10.1016/s0021-9258(18)50898-x

Harms, U., Andreou, A. Z., Gubaev, A., & Klostermeier, D. (2014). eIF4B, eIF4G and RNA regulate eIF4A activity in translation initiation by modulating the eIF4A conformational cycle. Nucleic Acids Research, 42(12), 7911–7922.

Hershey, J. W. B., Sonenberg, N., & Mathews, M. B. (2012). Principles of translational control: an overview. Cold Spring Harbor Perspectives in Biology, 4(12). https://doi.org/10.1101/cshperspect.a011528

Hershey, P. E., McWhirter, S. M., Gross, J. D., Wagner, G., Alber, T., & Sachs, A. B. (1999). The Cap-binding protein eIF4E promotes folding of a functional domain of yeast translation initiation factor eIF4G1. The Journal of Biological Chemistry, 274(30), 21297–21304.

Hinnebusch, A. G. (2014). The Scanning Mechanism of Eukaryotic Translation Initiation. In Annual Review of Biochemistry (Vol. 83, Issue 1, pp. 779–812). https://doi.org/10.1146/annurev-biochem-060713-035802

Hinnebusch, A. G., Ivanov, I. P., & Sonenberg, N. (2016). Translational control by 5′-untranslated regions of eukaryotic mRNAs. In Science (Vol. 352, Issue 6292, pp. 1413–1416). https://doi.org/10.1126/science.aad9868

Hinnebusch, A. G., & Lorsch, J. R. (2012). The mechanism of eukaryotic translation initiation: new insights and challenges. Cold Spring Harbor Perspectives in Biology, 4(10). https://doi.org/10.1101/cshperspect.a011544

Hirschman, J. E., Balakrishnan, R., Christie, K. R., Costanzo, M. C., Dwight, S. S., Engel, S. R., Fisk, D. G., Hong, E. L., Livstone, M. S., Nash, R., Park, J., Oughtred, R., Skrzypek, M., Starr, B., Theesfeld, C. L., Williams, J., Andrada, R., Binkley, G., Dong, Q., … Cherry, J. M. (2006). Genome Snapshot: a new resource at the Saccharomyces Genome Database (SGD) presenting an overview of the Saccharomyces cerevisiae genome. Nucleic Acids Research, 34(Database issue), D442–D445.

Hussain, T., Llácer, J. L., Fernández, I. S., Munoz, A., Martin-Marcos, P., Savva, C. G., Lorsch, J. R., Hinnebusch, A. G., & Ramakrishnan, V. (2014). Structural changes enable start codon recognition by the eukaryotic translation initiation complex. Cell, 159(3), 597–607.

Hwang, L. C., Hohlbein, J., Holden, S. J., & Kapanidis, A. N. (2009). Single-Molecule FRET: Methods and Biological Applications. In Handbook of Single-Molecule Biophysics (pp. 129–163). https://doi.org/10.1007/978-0-387-76497-9_5

Ingolia, N. T., Brar, G. A., Rouskin, S., McGeachy, A. M., & Weissman, J. S. (2012). The ribosome profiling strategy for monitoring translation in vivo by deep sequencing of ribosome-protected mRNA fragments. Nature Protocols, 7(8), 1534–1550.

Jackson, R. J., Hellen, C. U. T., & Pestova, T. V. (2010). The mechanism of eukaryotic translation initiation and principles of its regulation. Nature Reviews. Molecular Cell Biology, 11(2), 113–127.

Jensen, K. B., Kate Dredge, B., Toubia, J., Jin, X., Iadevaia, V., Goodall, G. J., & Proud, C. G. (2021). capCLIP: a new tool to probe translational control in human cells through capture and identification of the eIF4E–mRNA interactome. In Nucleic Acids Research (Vol. 49, Issue 18, pp. e105–e105). https://doi.org/10.1093/nar/gkab604

Kahvejian, A., Svitkin, Y. V., Sukarieh, R., M'Boutchou, M.-N., & Sonenberg, N. (2005). Mammalian poly(A)-binding protein is a eukaryotic translation initiation factor, which acts via multiple mechanisms. Genes & Development, 19(1), 104–113.

Karaki, S., Andrieu, C., Ziouziou, H., & Rocchi, P. (2015). The Eukaryotic Translation Initiation Factor 4E (eIF4E) as a Therapeutic Target for Cancer. In Advances in Protein Chemistry and Structural Biology (pp. 1–26). https://doi.org/10.1016/bs.apcsb.2015.09.001

Kats, I. R., & Klann, E. (2019). Translating from cancer to the brain: regulation of protein synthesis by eIF4F. In Learning & Memory (Vol. 26, Issue 9, pp. 332–342). https://doi.org/10.1101/lm.050047.119

Kaye, N. M., Emmett, K. J., Merrick, W. C., & Jankowsky, E. (2009). Intrinsic RNA Binding by the Eukaryotic Initiation Factor 4F Depends on a Minimal RNA Length but Not on the m7G Cap. In Journal of Biological Chemistry (Vol. 284, Issue 26, pp. 17742–17750). https://doi.org/10.1074/jbc.m109.009001

Kertesz, M., Wan, Y., Mazor, E., Rinn, J. L., Nutter, R. C., Chang, H. Y., & Segal, E. (2010). Genome-wide measurement of RNA secondary structure in yeast. Nature, 467(7311), 103–107.

Khong, A., & Parker, R. (2018). mRNP architecture in translating and stress conditions reveals an ordered pathway of mRNP compaction. The Journal of Cell Biology, 217(12), 4124–4140.

Kozak, M. (1999). Initiation of translation in prokaryotes and eukaryotes. In Gene (Vol. 234, Issue 2, pp. 187–208). https://doi.org/10.1016/s0378-1119(99)00210-3

Lai, W.-J. C., Kayedkhordeh, M., Cornell, E. V., Farah, E., Bellaousov, S., Rietmeijer, R., Salsi, E., Mathews, D. H., & Ermolenko, D. N. (2018). mRNAs and lncRNAs intrinsically form secondary structures with short end-to-end distances. Nature Communications, 9(1), 4328.

Leija-Martínez, N., Casas-Flores, S., Cadena-Nava, R. D., Roca, J. A., Mendez-Cabañas, J. A., Gomez, E., & Ruiz-Garcia, J. (2014). The separation between the 5′-3′ ends in long RNA molecules is short and nearly constant. In Nucleic Acids Research (Vol. 42, Issue 22, pp. 13963–13968). https://doi.org/10.1093/nar/gku1249

Leppek, K., Das, R., & Barna, M. (2018). Functional 5′ UTR mRNA structures in eukaryotic translation regulation and how to find them. In Nature Reviews Molecular Cell Biology (Vol. 19, Issue 3, pp. 158–174). https://doi.org/10.1038/nrm.2017.103

Liu, X., Schuessler, P. J., Sahoo, A., & Walker, S. E. (2019). Reconstitution and analyses of RNA interactions with eukaryotic translation initiation factors and ribosomal preinitiation complexes. Methods , 162-163, 42–53.

Lorsch, J. R. (2012). A knotty problem: Dissecting the molecular mechanics of mRNA recruitment to the eukaryotic ribosome. In The FASEB Journal (Vol. 26, Issue S1). https://doi.org/10.1096/fasebj.26.1_supplement.461.1

Lu, W.-T., Wilczynska, A., Smith, E., & Bushell, M. (2014). The diverse roles of the eIF4A family: you are the company you keep. Biochemical Society Transactions, 42(1), 166–172.

Machida, K., Shigeta, T., Yamamoto, Y., Ito, T., Svitkin, Y., Sonenberg, N., & Imataka, H. (2018). Dynamic interaction of poly(A)-binding protein with the ribosome. Scientific Reports, 8(1), 17435.

Mamane, Y., Petroulakis, E., Rong, L., Yoshida, K., Ler, L. W., & Sonenberg, N. (2004). eIF4E – from translation to transformation. In Oncogene (Vol. 23, Issue 18, pp. 3172–3179). https://doi.org/10.1038/sj.onc.1207549

McKinney, S. A., Joo, C., & Ha, T. (2006). Analysis of Single-Molecule FRET Trajectories Using Hidden Markov Modeling. In Biophysical Journal (Vol. 91, Issue 5, pp. 1941–1951). https://doi.org/10.1529/biophysj.106.082487

Mendelsohn, B. A., Bennett, N. K., Darch, M. A., Yu, K., Nguyen, M. K., Pucciarelli, D., Nelson, M., Horlbeck, M. A., Gilbert, L. A., Hyun, W., Kampmann, M., Nakamura, J. L., & Nakamura, K. (2018). A high-throughput screen of real-time ATP levels in individual cells reveals mechanisms of energy failure. PLoS Biology, 16(8), e2004624.

Merrick, W. C. (1990). Overview: Mechanism of Translation Initiation in Eukaryotes. In Enzyme (Vol. 44, Issues 1-4, pp. 7–16). https://doi.org/10.1159/000468743

Merrick, W. C. (2015). eIF4F: A Retrospective. In Journal of Biological Chemistry (Vol. 290, Issue 40, pp. 24091–24099). https://doi.org/10.1074/jbc.r115.675280

Mitchell, S. F., Walker, S. E., Algire, M. A., Park, E.-H., Hinnebusch, A. G., & Lorsch, J. R. (2010). The 5′-7-Methylguanosine Cap on Eukaryotic mRNAs Serves Both to Stimulate Canonical Translation Initiation and to Block an Alternative Pathway. In Molecular Cell (Vol. 39, Issue 6, pp. 950–962). https://doi.org/10.1016/j.molcel.2010.08.021

Nanda, J. S., Saini, A. K., Muñoz, A. M., Hinnebusch, A. G., & Lorsch, J. R. (2013). Coordinated Movements of Eukaryotic Translation Initiation Factors eIF1, eIF1A, and eIF5 Trigger Phosphate Release from eIF2 in Response to Start Codon Recognition by the Ribosomal Preinitiation Complex*. In Journal of Biological Chemistry (Vol. 288, Issue 8, pp. 5316–5329). https://doi.org/10.1074/jbc.m112.440693

Niedzwiecka, A., Darzynkiewicz, E., & Stolarski, R. (2004). Thermodynamics of mRNA 5' cap binding by eukaryotic translation initiation factor eIF4E. Biochemistry, 43(42), 13305–13317.

Niedzwiecka, A., Stepinski, J., Darzynkiewicz, E., Sonenberg, N., & Stolarski, R. (2002). Positive heat capacity change upon specific binding of translation initiation factor eIF4E to mRNA 5' cap. Biochemistry, 41(40), 12140–12148.

Nielsen, K. H., Behrens, M. A., He, Y., Oliveira, C. L. P., Jensen, L. S., Hoffmann, S. V., Pedersen, J. S., & Andersen, G. R. (2011). Synergistic activation of eIF4A by eIF4B and eIF4G. Nucleic Acids Research, 39(7), 2678–2689.

Oberer, M., Marintchev, A., & Wagner, G. (2005). Structural basis for the enhancement of eIF4A helicase activity by eIF4G. Genes & Development, 19(18), 2212–2223.

O'Leary, S. E., Petrov, A., Chen, J., & Puglisi, J. D. (2013). Dynamic recognition of the mRNA cap by Saccharomyces cerevisiae eIF4E. Structure , 21(12), 2197–2207.

Özeş, A. R., Feoktistova, K., Avanzino, B. C., & Fraser, C. S. (2011). Duplex Unwinding and ATPase Activities of the DEAD-Box Helicase eIF4A Are Coupled by eIF4G and eIF4B. In Journal of Molecular Biology (Vol. 412, Issue 4, pp. 674–687). https://doi.org/10.1016/j.jmb.2011.08.004

Palmiter, R. D. (1975). Quantitation of parameters that determine the rate of ovalbumin synthesis. Cell, 4(3), 189.

Park, E.-H., Zhang, F., Warringer, J., Sunnerhagen, P., & Hinnebusch, A. G. (2011). Depletion of eIF4G from yeast cells narrows the range of translational efficiencies genome-wide. BMC Genomics, 12, 68.

Pelletier, J., Graff, J., Ruggero, D., & Sonenberg, N. (2015). Targeting the eIF4F translation initiation complex: a critical nexus for cancer development. Cancer Research, 75(2), 250–263.

Pelletier, J., & Sonenberg, N. (1985). Photochemical cross-linking of cap binding proteins to eucaryotic mRNAs: effect of mRNA 5' secondary structure. Molecular and Cellular Biology, 5(11), 3222–3230.

Pelletier, J., & Sonenberg, N. (2019). The Organizing Principles of Eukaryotic Ribosome Recruitment. Annual Review of Biochemistry, 88, 307–335.

Pestova, T. V., & Hellen, C. U. T. (2013). Translation Initiation in Eukaryotes: Factors and Mechanisms. In Encyclopedia of Biological Chemistry (pp. 432–435). https://doi.org/10.1016/b978-0-12-378630-2.00482-5

Petrov, A., Grosely, R., Chen, J., O'Leary, S. E., & Puglisi, J. D. (2016). Multiple Parallel Pathways of Translation Initiation on the CrPV IRES. Molecular Cell, 62(1), 92–103.

Prabhakar, A., Choi, J., Wang, J., Petrov, A., & Puglisi, J. D. (2017). Dynamic basis of fidelity and speed in translation: Coordinated multistep mechanisms of elongation and termination. Protein Science: A Publication of the Protein Society, 26(7), 1352–1362.

Rajagopal, V., Park, E.-H., Hinnebusch, A. G., & Lorsch, J. R. (2012a). Specific Domains in Yeast Translation Initiation Factor eIF4G Strongly Bias RNA Unwinding Activity of the eIF4F Complex toward Duplexes with 5′-Overhangs. In Journal of Biological Chemistry (Vol. 287, Issue 24, pp. 20301–20312). https://doi.org/10.1074/jbc.m112.347278

Rajagopal, V., Park, E.-H., Hinnebusch, A. G., & Lorsch, J. R. (2012b). Specific domains in yeast translation initiation factor eIF4G strongly bias RNA unwinding activity of the eIF4F complex toward duplexes with 5'-overhangs. The Journal of Biological Chemistry, 287(24), 20301–20312.

Ramanathan, A., Brett Robb, G., & Chan, S.-H. (2016). mRNA capping: biological functions and applications. In Nucleic Acids Research (Vol. 44, Issue 16, pp. 7511–7526). https://doi.org/10.1093/nar/gkw551

Ray, B. K., Lawson, T. G., Kramer, J. C., Cladaras, M. H., Grifo, J. A., Abramson, R. D., Merrick, W. C., & Thach, R. E. (1985). ATP-dependent unwinding of messenger RNA structure by eukaryotic initiation factors. The Journal of Biological Chemistry, 260(12), 7651–7658.

Rubio, C. A., Weisburd, B., Holderfield, M., Arias, C., Fang, E., DeRisi, J. L., & Fanidi, A. (2014). Transcriptome-wide characterization of the eIF4A signature highlights plasticity in translation regulation. Genome Biology, 15(10), 476.

Schütz, P., Bumann, M., Oberholzer, A. E., Bieniossek, C., Trachsel, H., Altmann, M., & Baumann, U. (2008). Crystal structure of the yeast eIF4A-eIF4G complex: an RNA-helicase controlled by protein-protein interactions. Proceedings of the National Academy of Sciences of the United States of America, 105(28), 9564–9569.

Schwartz, D. C., & Parker, R. (2000). mRNA decapping in yeast requires dissociation of the cap binding protein, eukaryotic translation initiation factor 4E. Molecular and Cellular Biology, 20(21), 7933–7942.

Sen, N. D., Zhou, F., Ingolia, N. T., & Hinnebusch, A. G. (2015). Genome-wide analysis of translational efficiency reveals distinct but overlapping functions of yeast DEAD-box RNA helicases Ded1 and eIF4A. Genome Research, 25(8), 1196–1205.

Shah, P., Ding, Y., Niemczyk, M., Kudla, G., & Plotkin, J. B. (2013). Rate-limiting steps in yeast protein translation. Cell, 153(7), 1589–1601.

Sharma, A. K., Sormanni, P., Ahmed, N., Ciryam, P., Friedrich, U. A., Kramer, G., & O'Brien, E. P. (2019). A chemical kinetic basis for measuring translation initiation and elongation rates from ribosome profiling data. PLoS Computational Biology, 15(5), e1007070.

Shatkin, A. (1976). Capping of eucaryotic mRNAs. In Cell (Vol. 9, Issue 4, pp. 645–653). https://doi.org/10.1016/0092-8674(76)90128-8

Silvera, D., Formenti, S. C., & Schneider, R. J. (2010). Translational control in cancer. In Nature Reviews Cancer (Vol. 10, Issue 4, pp. 254–266). https://doi.org/10.1038/nrc2824

Slepenkov, S. V., Darzynkiewicz, E., & Rhoads, R. E. (2006). Stopped-flow kinetic analysis of eIF4E and phosphorylated eIF4E binding to cap analogs and capped oligoribonucleotides: evidence for a one-step binding mechanism. The Journal of Biological Chemistry, 281(21), 14927–14938.

Slepenkov, S. V., Korneeva, N. L., & Rhoads, R. E. (2008). Kinetic Mechanism for Assembly of the m7GpppG·eIF4E·eIF4G Complex. In Journal of Biological Chemistry (Vol. 283, Issue 37, pp. 25227–25237). https://doi.org/10.1074/jbc.m801786200

Sokabe, M., & Fraser, C. S. (2019). Toward a Kinetic Understanding of Eukaryotic Translation. In Cold Spring Harbor Perspectives in Biology (Vol. 11, Issue 2, p. a032706). https://doi.org/10.1101/cshperspect.a032706

Sonenberg, N., & Gingras, A.-C. (1998). The mRNA 5′ cap-binding protein eIF4E and control of cell growth. In Current Opinion in Cell Biology (Vol. 10, Issue 2, pp. 268–275). https://doi.org/10.1016/s0955-0674(98)80150-6

Sonenberg, N., Hershey, J. W. B., & Mathews, M. B. (2001). Translational Control of Gene Expression. CSHL Press.

Sonenberg, N., & Hinnebusch, A. G. (2009). Regulation of Translation Initiation in Eukaryotes: Mechanisms and Biological Targets. In Cell (Vol. 136, Issue 4, pp. 731–745). https://doi.org/10.1016/j.cell.2009.01.042

Sonenberg, N., Morgan, M. A., Merrick, W. C., & Shatkin, A. J. (1978). A polypeptide in eukaryotic initiation factors that crosslinks specifically to the 5’-terminal cap in mRNA. In Proceedings of the National Academy of Sciences (Vol. 75, Issue 10, pp. 4843–4847). https://doi.org/10.1073/pnas.75.10.4843

Sonenberg, N., Trachsel, H., Hecht, S., & Shatkin, A. J. (1980). Differential stimulation of capped mRNA translation in vitro by cap binding protein. In Nature (Vol. 285, Issue 5763, pp. 331–333). https://doi.org/10.1038/285331a0

Szavits-Nossan, J., & Ciandrini, L. (2020). Inferring efficiency of translation initiation and elongation from ribosome profiling. In Nucleic Acids Research (Vol. 48, Issue 17, pp. 9478–9490). https://doi.org/10.1093/nar/gkaa678

Tarun, S. Z., Jr, & Sachs, A. B. (1995). A common function for mRNA 5’ and 3' ends in translation initiation in yeast. Genes & Development, 9(23), 2997–3007.

Tarun, S. Z., Wells, S. E., Deardorff, J. A., & Sachs, A. B. (1997). Translation initiation factor eIF4G mediates in vitro poly(A) tail-dependent translation. In Proceedings of the

National Academy of Sciences (Vol. 94, Issue 17, pp. 9046–9051). https://doi.org/10.1073/pnas.94.17.9046

Tauber, D., Tauber, G., Khong, A., Van Treeck, B., Pelletier, J., & Parker, R. (2020). Modulation of RNA Condensation by the DEAD-Box Protein eIF4A. Cell, 180(3), 411–426.e16.

Thompson, M. K., & Gilbert, W. V. (2017). mRNA length-sensing in eukaryotic translation: reconsidering the “closed loop” and its implications for translational control. Current Genetics, 63(4), 613–620.

Tinoco, I., & Gonzalez, R. L. (2011). Biological mechanisms, one molecule at a time. In Genes & Development (Vol. 25, Issue 12, pp. 1205–1231). https://doi.org/10.1101/gad.2050011

Truitt, M. L., Conn, C. S., Shi, Z., Pang, X., Tokuyasu, T., Coady, A. M., Seo, Y., Barna, M., & Ruggero, D. (2015). Differential Requirements for eIF4E Dose in Normal Development and Cancer. Cell, 162(1), 59–71.

Tsai, A. (2013). The Dynamics of Translation Initiation and Elongation.

van de Meent, J.-W., Bronson, J. E., Wiggins, C. H., & Gonzalez, R. L., Jr. (2014). Empirical Bayes methods enable advanced population-level analyses of single-molecule FRET experiments. Biophysical Journal, 106(6), 1327–1337.

Vicens, Q., Kieft, J. S., & Rissland, O. S. (2018). Revisiting the Closed-Loop Model and the Nature of mRNA 5′–3′ Communication. In Molecular Cell (Vol. 72, Issue 5, pp. 805–812). https://doi.org/10.1016/j.molcel.2018.10.047

Villa, N., Do, A., Hershey, J. W. B., & Fraser, C. S. (2013). Human Eukaryotic Initiation Factor 4G (eIF4G) Protein Binds to eIF3c, -d, and -e to Promote mRNA Recruitment to the Ribosome. In Journal of Biological Chemistry (Vol. 288, Issue 46, pp. 32932–32940). https://doi.org/10.1074/jbc.m113.517011

von der Haar, T., & McCarthy, J. E. G. (2002). Intracellular translation initiation factor levels in Saccharomyces cerevisiae and their role in cap-complex function. Molecular Microbiology, 46(2), 531–544.

Wang, J., Johnson, A. G., Lapointe, C. P., Choi, J., Prabhakar, A., Chen, D.-H., Petrov, A. N., & Puglisi, J. D. (2019). eIF5B gates the transition from translation initiation to elongation. Nature, 573(7775), 605–608.

Wolfe, A. L., Singh, K., Zhong, Y., Drewe, P., Rajasekhar, V. K., Sanghvi, V. R., Mavrakis, K. J., Jiang, M., Roderick, J. E., Van der Meulen, J., Schatz, J. H., Rodrigo, C. M., Zhao, C., Rondou, P., de Stanchina, E., Teruya-Feldstein, J., Kelliher, M. A., Speleman, F., Porco, J. A., Jr, … Wendel, H.-G. (2014). RNA G-quadruplexes cause eIF4A-dependent oncogene translation in cancer. Nature, 513(7516), 65–70.

Yanagiya, A., Svitkin, Y. V., Shibata, S., Mikami, S., Imataka, H., & Sonenberg, N. (2009). Requirement of RNA binding of mammalian eukaryotic translation initiation factor 4GI (eIF4GI) for efficient interaction of eIF4E with the mRNA cap. Molecular and Cellular Biology, 29(6), 1661–1669.

Yoffe, A. M., Prinsen, P., Gelbart, W. M., & Ben-Shaul, A. (2011). The ends of a large RNA molecule are necessarily close. Nucleic Acids Research, 39(1), 292–299.

Yourik, P., Aitken, C. E., Zhou, F., Gupta, N., Hinnebusch, A. G., & Lorsch, J. R. (2017). Yeast eIF4A enhances recruitment of mRNAs regardless of their structural complexity. eLife, 6. https://doi.org/10.7554/eLife.31476